A THERMODYNAMIC APPRAISAL OF MINERAL EQUILIBRIA IN SILICEOUS DOLOMITIC LIMESTONES DURING CONTACT METAMORPHISM

by

Carol J. Schnake

Submitted in Partial Fulfillment
of the Requirements for the Degree of
Master of Science in Geochemistry

New Mexico Institute of Mining and Technology

Socorro, New Mexico

December, 1977

ABSTRACT

Equilibrium phase relations in the system $CaO-MgO-SiO_2-H_2O-CO_2$ can be calculated if the necessary thermodynamic data for the phases involved is available. Where such data is lacking, as for the minerals rankinite, spurrite and tilleyite, it can be either estimated or computed with a fair degree of accuracy using experimentally determined phase equilibria. The thermodynamic data can then be utilized to construct temperature-pressure and temperature - X_{CO_2} topologies which, in general, correspond quite closely to published experimental equilibrium curves. Activity-activity diagrams can also be constructed with this data over a range of temperature and pressure to illustrate isochemical processes such as dehydration and decarbonation as well as to show the effects of the changing chemical potentials of the components in the system upon mineral stabilities. The phase relations depicted in the activity diagrams compare favorably with the phase relations commonly observed both in the laboratory and in natural systems. In addition, these diagrams reveal that the silicate minerals monticellite, merwinite, Ca-olivine, rankinite, spurrite and tilleyite are thermodynamically stable with respect to the carbonates calcite, dolomite and magnesite only at temperatures $\geq 600^{\circ}C$, total pressures <100 bars and large chemical potentials of the CaO component.

TABLE OF CONTENTS

LIST OF FIGURES

LIST OF FIGURES (cont.)

LIST OF FIGURES (cont.)

LIST OF FIGURES (Cont.)

LIST OF FIGURES (Cont.)

LIST OF FIGURES (cont.)

LIST OF FIGURES (cont.)

LIST OF FIGURES (cont.)

LIST OF TABLES

LIST OF TABLES (cont.)

LIST OF SYMBOLS

a - coefficient in equation (6).

a_i - activity of ith species.

a_1, a_2, a_3..... - empirical coefficients, as used in equations (1) and (12).

α_i - coefficient of thermal expansion of the ith species.

b - coefficient in equation (6).

c - coefficient in equation (6).

χ_i - compressibility of the ith species.

Cp_ϕ - heat capacity of the ϕth phase.

ΔCp_r - heat capacity of reaction.

γ_i - fugacity coefficient of the ith species.

γ_i° - fugacity coefficient of the ith species in the standard state.

f_i - fugacity of the ith species.

f_i° - standard fugacity of the ith species.

$\Delta G_{r,T,P}$ - Gibbs free energy of reaction at T and P.

$\Delta G^\circ_{r,T,P}$ - standard Gibbs free energy of reaction at T and P.

$H_T - H_{298}$ - difference between the enthalpy of a phase at T and T = 298.

$\Delta H^\circ_{f,i}$ - standard enthalpy of formation from the elements of the ith species.

$\Delta H^\circ_{r,T,P}$ - standard enthalpy of reaction at T and P.

k', k'' - coefficients in equations (10) and (11).

K - equilibrium constant.

m - coefficient in equation (13).

μ_i - chemical potential of the ith species.

μ_i° - standard chemical potential of the ith species.

$n_{i,\phi}$ - number of moles of the ith species in the ϕth phase.

N_i - mole fraction of the ith species.

ν_i - reaction coefficient of the ith species.

P - pressure (bars).

P_r - reference pressure (bars).

$Q_{r,T,P}$ - activity product of the reaction at T and P.

R - gas constant, equal to 1.987 cal/mole-deg.

S_i° - standard third law entropy of the ith species.

$S^\circ_{298.15,\phi}$ - standard third law entropy of the ϕth phase at 298.15 K.

$\Delta S^\circ_{r,T,P}$ - standard third law entropy of reaction at T and P.

T - temperature (Kelvin).

T_r - reference temperature (Kelvin).

V_i - volume of the ith species.

V_i° - standard volume of the ith species.

$\overline{V}_i$ - partial molal volume of the ith species.

ACKNOWLEDGEMENTS

I would like to thank Dr. Richard E. Beane, my advisor, for both introducing me to, and encouraging me to enter, the field of theoretical geochemistry. The many stimulating discussions in addition to the valuable advice and encouragement offered by Dr. Beane were instrumental in the completion of this thesis. I would also like to thank Dr. Marc W. Bodine and Dr. A. J. Budding, the other members of my committee, who kindly reviewed this manuscript, and David W. Schnake and Jeanne L. Bruton, who deserve special recognition for the many ways in which they have expressed their support of my work.

INTRODUCTION

Metamorphism has been classically treated as the mineralogical and structural response of rocks to changes in temperature and pressure in systems which are closed, and therefore isochemical, with respect to all components except H_2O and CO_2. However, geologic studies indicate that many Tertiary intrusives in the Southwestern U.S. were emplaced at very shallow depths and actually intersected regions of dynamic groundwater flow. Consequently, the metamorphism occurring around these intrusions would be indicative of an open system in which composition is an additional variable according to classical thermodynamics. The purpose of this thesis is to study the effects of changes in both physical and chemical parameters upon equilibria in the system $CaO-MgO-SiO_2-H_2O-CO_2$ through a series of thermochemical calculations. Temperature and pressure will be considered as variables in the physical environment while the chemical environment will be described in terms of the changing chemical potential of components in the system. The effects of mixing H_2O and CO_2 in the fluid phase will also be studied. The range of conditions considered will parallel the contact metamorphism of siliceous dolomitic limestones; namely, temperatures and pressures up to $1100^{\circ}C$ and 1000 bars. This thesis is not meant to be a definitive study of the contact metamorphism of siliceous dolomitic limestones but is rather an appraisal of the thermodynamic methods that can be utilized to model metamorphism.

The standard states adopted in this paper are: the pure phase at any specified temperature and pressure for solids and liquids; for gases,

the hypothetical ideal gas at any specified temperature and 1 atm. pressure; and, for components such as CaO(c) and MgO(c), the pure solid oxide at the temperature and pressure of interest. The standard state for ions is a hypothetical one molal solution at 1 atm. and the temperature of interest.

COMPOSITIONAL AND THERMODYNAMIC CHARACTERISTICS OF THE SYSTEM

The compositions of minerals in the system $CaO-MgO-SiO_2-H_2O-CO_2$ considered in this study are listed in Table 1 and plotted on the compositional triangle $CaO-MgO-SiO_2$ in Figure 1 assuming the presence of ubiquitous H_2O and CO_2. Most of the necessary thermodynamic data for these phases is available in the literature (e.g., Robie and Waldbaum, 1968) and is tabulated in Appendix A; however, no thermodynamic data whatsoever is currently available for spurrite and tilleyite and only a value of ΔH_f° has been established for rankinite. To include these minerals in the following calculations, an estimation of their thermodynamic properties was first attempted as described below.

ESTIMATION OF THERMODYNAMIC DATA

Heat Capacity

It has been shown that the heat capacity of a mineral can be closely approximated by summing the heat capacities of its component oxides in stochiometric proportions; similarly, the heat capacity power function of a mineral can be estimated using the power functions of the appropriate

Table 1. Composition of minerals in the system $CaO-MgO-SiO_2-H_2O-CO_2$ considered in this study.

Mineral Name	Chemical Formula
Quartz	SiO_2
Lime	CaO
Periclase	MgO
Portlandite	$Ca(OH)_2$
Brucite	$Mg(OH)_2$
Aragonite	$CaCO_3$
Calcite	$CaCO_3$
Magnesite	$MgCO_3$
Dolomite	$CaMg(CO_3)_2$
Huntite	$CaMg_3(CO_3)_4$
Wollastonite	$CaSiO_3$
Ca-olivine	$\gamma-Ca_2SiO_4$
B-larnite	$\beta-Ca_2SiO_4$
Rankinite	$Ca_3Si_2O_7$
Clinoenstatite	$MgSiO_3$
Forsterite	Mg_2SiO_4
Chrysotile (serpentine)	$Mg_3Si_2O_5(OH)_4$
Talc	$Mg_3Si_4O_{10}(OH)_2$
Monticellite	$CaMgSiO_4$
Diopside	$CaMgSi_2O_6$
Akermanite	$Ca_2MgSi_2O_7$
Merwinite	$Ca_3MgSi_2O_8$

Table 1, cont.

Mineral Name	Chemical Formula
Tremolite	$Ca_2Mg_5Si_8O_{22}(OH)_2$
Spurrite	$2Ca_2SiO_4 \cdot CaCO_3$
Tilleyite	$Ca_5Si_2O_7(CO_3)_2$

Figure 1. Triangular composition diagram (assuming ubiquitous H_2O and CO_2) illustrating the composition of minerals in the system CaO-MgO-SiO_2-H_2O-CO_2.

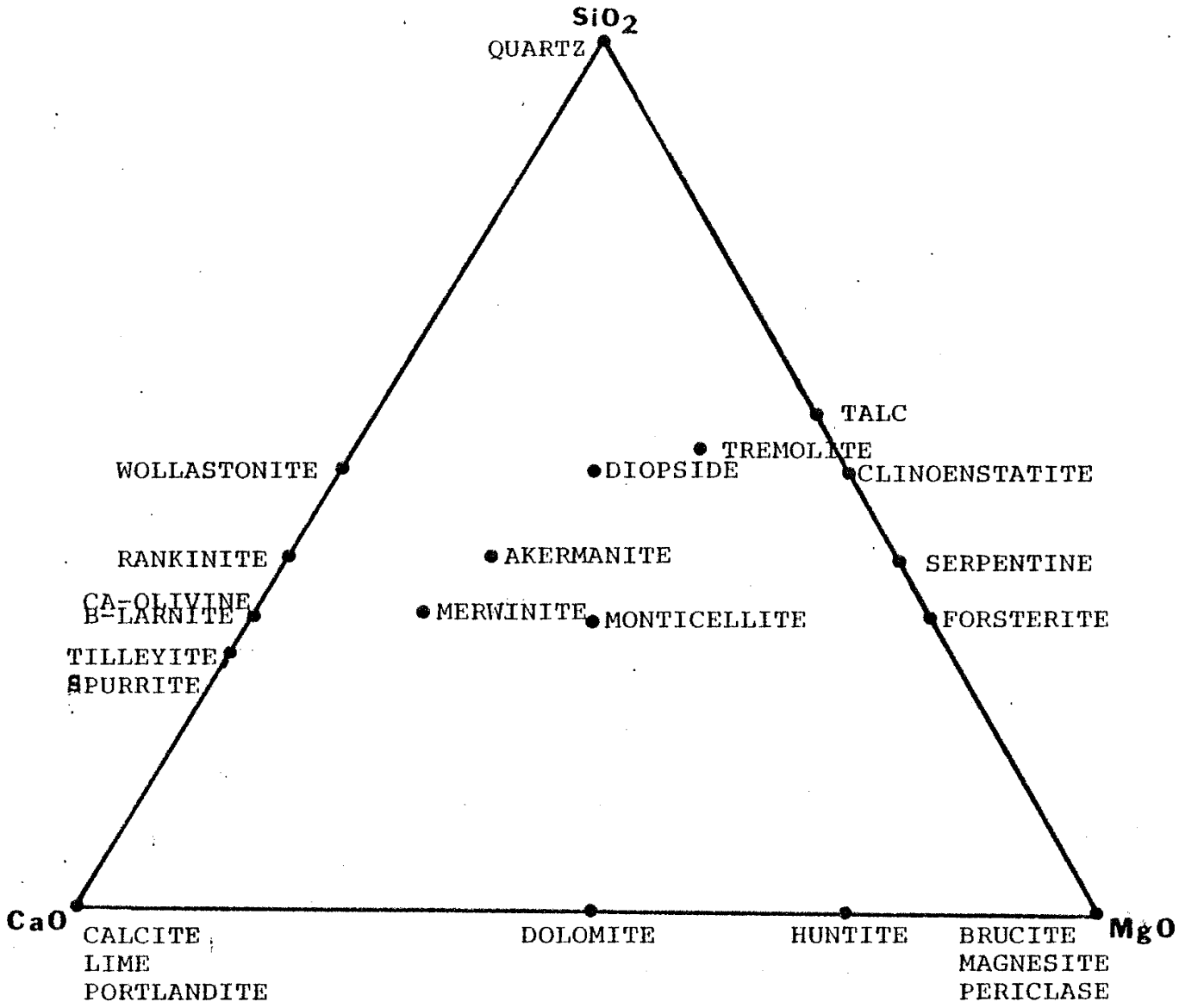
SiO2
QUARTZ
TALC
TREMOLITE
WOLLASTONITE
DIOPSIDE
CLINOENSTATITE
RANKINITE
AKERMANITE
SERPENTINE
CA-OLIVINE
B-LARNITE
MERWINITE
MONTICELLITE
FORSTERITE
TILLEYITE
SPURRITE
CaO
MgO
CALCITE
LIME
PORTLANDITE
DOLOMITE
HUNTITE
BRUCITE
MAGNESITE
PERICLASE

components (Helgeson, 1968). An alternate method of estimation would result if the heat capacity contribution of each of the oxide components in the mineral to the mineral's total heat capacity was determined. That is, if the number of moles of the oxide in the mineral is known along with the mineral's heat capacity at a specified temperature, there should be some value for each oxide which could be multiplied by the number of moles of the oxide and added to the contributions of the other oxides determined in a similar manner to obtain the known heat capacity of the mineral. Thus:

$$Cp_{\phi} = a_1 n_{1,\phi} + a_2 n_{2,\phi} + a_3 n_{3,\phi} + \ldots . \quad (1)$$

$$= \Sigma\, a_i n_{i,\phi} \quad (2)$$

where ϕ refers to the mineral under consideration, Cp is equal to the heat capacity of that mineral at some specified temperature, $n_{1,\phi}$, $n_{2,\phi}$ and $n_{3,\phi}$ represent the number of moles of oxide components 1, 2 and 3 in one mole of the ϕth mineral and a_1, a_2 and a_3 are the coefficients representing the contributions of oxide components 1, 2 and 3 to the heat capacity of the mineral at the specified temperature. The heat capacity contributions of the component oxides obtained in this manner are not necessarily equivalent to the published heat capacities or heat capacity power functions of the pure oxides, but instead reflect the contribution of the oxides as integral parts of a phase to the mineral's heat capacity.

For the minerals in the system under consideration, equation (1) can be rewritten

$$Cp_{\phi} = a_1 n_{CaO,\phi} + a_2 n_{MgO,\phi} + a_3 n_{SiO_2,\phi} + a_4 n_{H_2O,\phi} + a_5 n_{CO_2,\phi} \quad (3)$$

such that the temperature dependence of the heat capacity is

$$\frac{dCp\phi}{dT} = \left(\frac{da_1}{dT}\right) n_{CaO,\phi} + \left(\frac{da_2}{dT}\right) n_{MgO,\phi} + \left(\frac{da_3}{dT}\right) n_{SiO_2,\phi} + \left(\frac{da_4}{dT}\right) n_{H_2O,\phi} + \left(\frac{da_5}{dT}\right) n_{CO_2,\phi} . \quad (4)$$

The coefficients a_i represent the contribution of the component oxides to the heat capacity of a mineral, and an expression of the conventional form for heat capacities, viz. $Cp = a + bT + c/T^2$, can be formulated for each. By doing so, the heat capacity power function of a mineral, usually described by this polynomial because of its ability to portray the dependence of heat capacity on temperature, can be obtained by the simple summation of the heat capacity power functions of its component oxides in stochiometric proportions.

In order to estimate the heat capacity contributions of the CaO, MgO and SiO_2 components, experimentally determined heat capacity power functions of minerals in the system $CaO-MgO-SiO_2$ were used to calculate numerical values of Cp at 100°C temperature intervals. If n minerals are chosen, n number of simultaneous equations in the form of equation (1) can be written at each specified temperature. Each of these sets of simultaneous equations may then be solved for the heat capacity contributions of the component oxides CaO, MgO and SiO_2 (represented by a_1, a_2 and a_3 in equation 1) at the temperature considered using a linear least square regression. Subsequent regression of the oxide components' heat capacity contributions as functions of temperature provides a heat capacity power function of the form $a + bT + c/T^2$ for each component oxide. This power function represents the contribution of the oxide component under consideration to the heat capacity of a mineral.

The minerals chosen for this part of the study were B-larnite, clinoenstatite, merwinite, akermanite, forsterite, wollastonite and diopside. Robie and Waldbaum (1968) have published tables of H_T-H_{298} values

for these minerals and this data was regressed to determine the heat capacity power function for each because

$$H_T - H_{298} = \int_{298}^{T} Cp_{\phi}\, dT \qquad (5)$$

$$= a(T-T_{298}) + \frac{b}{2}(T^2-T_{298}) - c(\frac{1}{T} - \frac{1}{T_{298}}) \qquad (6)$$

The heat capacity power functions obtained in this manner are in good agreement with the heat capacity power functions determined by Kelley (1960) using the same H_T-H_{298} data and were therefore used to calculate the heat capacities of the minerals from 100° to 1200°C at 100°C intervals. With this data and the coefficients of the oxides in the minerals, the calculations described above were carried out to determine the temperature-dependent contributions of the CaO, MgO and SiO_2 components to the heat capacity of a mineral. The results are shown in Table 2.

A comparison of the heat capacities of wollastonite and clinoenstatite, found to be representative of the minerals in the system, generated by 1) stochiometric summation of the heat capacity power functions of the pure oxides as described by Helgeson (1969), 2) summation of the heat capacity contributions of the component oxides in the mineral in the manner described above, and 3) the heat capacities calculated from the data of Robie and Waldbaum (1968) for these minerals, reveals that at lower temperatures, both summation methods seem to reproduce the data from Robie and Waldbaum with the same degree of accuracy. As temperature increases, the summation of the contributions of the component oxides reproduces the measured heat capacities more accurately than the stochiometric summation method outlined by Helgeson. This might be expected

Table 2. Contribution of the oxide components CaO, MgO, SiO_2 and CO_2 to the heat capacity of a mineral (where $Cp = a + bT + c/T^2$).

Component Oxide	a	$b*10^{-3}$	$c*10^{5}$
CaO	8.38	3.91	2.55
MgO	8.22	3.69	1.12
SiO_2	19.85	-1.52	-11.79
CO_2	14.68	4.40	-8.23

because, in addition to the fact that the oxide component contributions were generated directly from the measured values of heat capacity, the SiO_2 component undergoes a phase change at 573°C. The heat capacity power function for the SiO_2 component in minerals takes this into account automatically, but the stochiometric summation method described by Helgeson must use α or β -quartz in the calculations depending on the temperature range in which the heat capacity is to be determined. In the preceding calculations, the heat capacity power function of α-quartz was used to estimate the heat capacity of minerals up to 1200°C, which would account for some of the error above 573°C. It is important to note that Helgeson never extended the use of this method above 300°C.

The heat capacity power function of rankinite listed in Appendix A was estimated by the component oxide power function summation method. This summation procedure is illustrated in Table 3. The heat capacity power functions for monticellite, merwinite and akermanite that are used in the following calculations were also estimated in this manner.

The estimation of the heat capacity power functions for spurrite ($2Ca_2SiO_4 \cdot CaCO_3$) and tilleyite ($Ca_5Si_2O_7(CO_3)_2$) poses a special problem because both minerals are "mixed" silicate-carbonates of calcium. The simplifying assumption may be made that the contributions of the CaO, MgO and SiO_2 components to the heat capacities of these minerals and the carbonates are equivalent to their contributions to silicates and, likewise, that the contribution of the CO_2 component to the heat capacity of the mixed carbonate silicates is equivalent to its contribution to carbonates. With this assumption in mind, the contribution of the CO_2 component to the heat capacity of carbonate minerals was estimated in the following minerals: calcite, dolomite and magnesite.

Table 3. Estimation of the heat capacity power functions of the form $a + bT + c/T^2$ for the minerals rankinite, spurrite and tilleyite.

Rankinite

Component Oxides	a	$b*10^{-3}$	$c*10^{5}$
3CaO	3(8.38)	3(3.91)	3(2.55)
$2SiO_2$	2(19.85)	2(-1.52)	2(-11.79)
$Ca_3Si_2O_7$	64.84	8.69	-15.93

Spurrite

5CaO	5(8.38)	5(3.91)	5(2.55)
$2SiO_2$	2(19.85)	2(-1.52)	2(-11.79)
CO_2	14.68	4.40	-8.23
$2Ca_2SiO_4 \cdot CaCO_3$	96.28	20.91	-19.06

Tilleyite

5CaO	5(8.38)	5(3.91)	5(2.55)
$2SiO_2$	2(19.85)	2(-1.52)	2(-11.79)
$2CO_2$	2(14.68)	2(4.40)	2(-8.23)
$Ca_5Si_2O_7(CO_3)_2$	110.96	25.31	-27.29

Therefore, $Cp_{rankinite} = 64.84 + 8.69*10^{-3}T - 15.93*10^{5}/T^2$,

$Cp_{spurrite} = 96.28 + 20.91*10^{-3}T - 19.06*10^{5}/T^2$ and

$Cp_{tilleyite} = 110.96 + 25.31*10^{-3}T - 27.29*10^{5}/T^2$.

The heat capacities of calcite, dolomite and magnesite were calculated using heat capacity power functions obtained by regression of $H_T - H_{298}$ values tabulated by Robie and Waldbaum. By subtracting the heat capacity contribution of the appropriate component oxides from the total heat capacities of these minerals over the temperature range of 25° to 1500°C using the previously calculated heat capacity contributions of the oxide components CaO and MgO to silicates, the contribution of the CO_2 component to each of the three minerals at each temperature is determined. Regression of these contributions using an expression of the form $a + bT + c/T^2$ yields a heat capacity power function representing the contribution of the CO_2 component to the total heat capacity of a mineral. The results are shown in Table 2.

A comparison of the heat capacities of calcite, dolomite and magnesite calculated from the heat capacity power function derived from the data of Robie and Waldbaum with those calculated from the power functions estimated from the method of summation of the contributions of the component oxides shows very good agreement as illustrated in Table 4. Thus, using the data in Table 2, the heat capacity power functions of spurrite and tilleyite were estimated as shown in Table 3 by summation of oxide component contributions.

Table 4. Comparison of the heat capacities of calcite, dolomite and magnesite as calculated from the data of Robie and Waldbaum (1968) and from the summation of the heat capacity contributions of the component oxides.

Calcite

K	Cp^{a}_{R+W} (cal/mole)	Cp^{b}_{COMP} (cal/mole)
298	19.60	19.15
400	23.17	22.83
600	26.36	26.47
800	28.19	28.82
1000	29.63	30.80
1200	30.91	32.64
1400	32.11	34.40

Dolomite

298	36.01	36.46
400	43.89	44.53
600	52.07	52.25
800	57.64	57.08
1000	62.46	61.08
1200	66.98	64.75
1400	71.36	68.27

Magnesite

298	17.04	17.31
400	21.64	21.69
600	25.95	25.78
800	28.59	28.26
1000	30.75	30.28
1200	32.71	32.11
1400	34.59	33.86

[a] calculated from the data of Robie and Waldbaum (1968)

[b] estimated by the summation of the heat capacity contributions of the component oxides

Entropy

According to the third law of thermodynamics, the standard entropy of a mineral which is perfectly crystalline at 0 K is given by the integral

$$S^{o}_{298.15,\phi} = \int_{o}^{298.15} \frac{(Cp\phi)}{T}\, dT \qquad (7)$$

where ϕ refers to the mineral under consideration, if no change of state occurs between 0 and 298 K. $S^{o}_{298.15}$ is commonly referred to as the standard third law entropy of the ϕth mineral. However, the experimental heat capacity data required to solve this equation is lacking for the minerals involved in this study and the heat capacity power functions estimated in the previous section are inapplicable below 298 K. Thus, another method of estimation must be sought.

Latimer (1951) proposed a method of approximation which assigned key values to the elements and the negative ions in solid compounds which could be summed in appropriate proportions to estimate the standard third law entropy of simple substances. However, this method of estimation becomes increasingly less definitive as the compound becomes more complex and therefore would be of limited value in the estimation of the entropies of minerals as complex as spurrite and tilleyite.

Kelley (1965) also published tables of additive entropy constants which could be used to estimate the entropy of a mineral. Table 5 lists a number of entropies of minerals, estimated by summing the entropy constants according to their stochiometric proportions in the mineral under consideration, for comparison to the standard third law entropies tabulated in Robie and Waldbaum (1968). The error in Kelley's method of estimation generally ranges from $\pm$ 1 to 7% for the minerals in Table 5.

Table 5. Comparison of standard third law entropies estimated by the method of Kelley (1965) with the tabulated values from Robie and Waldbaum (1968).

Mineral Name	$S^{o\ a}_{298.15}$, calculated	$S^{o\ b}_{298.15}$, tabulated
Akermanite	46.3 ± 2	50.03 ± 0.50
B-larnite	30.2 ± 2	30.50 ± 0.20
Ca-olivine	30.2 ± 2	28.80 ± 0.20
Clinoenstatite	16.1 ± 2	16.22 ± 0.10
Diopside	36.3 ± 2	34.20 ± 0.20
Forsterite	22.0 ± 2	22.75 ± 0.20
Merwinite	56.3 ± 2	60.5 ± 0.5
Monticellite	26.1 ± 2	24.5 ± 1.0
Talc	63.6 ± 2	62.34 ± 0.15
Tremolite	136.2 ± 2	131.19 ± 0.30
Wollastonite	20.2 ± 2	19.60 ± 0.20

[a] calculated using Kelley's (1965) tables of additive entropy constants (in cal/mole-deg)

[b] from Robie and Waldbaum (1968) (in cal/mole-deg)

Fyfe et al. (1958) observed that close approximations to the entropy of certain minerals can be obtained by summing the tabulated third law entropies of their component oxides. Estimating the entropies of a number of Ca-Mg silicates in this manner and comparing the results to Robie and Waldbaum's tabulated $S^{\circ}_{298.15}$ of the minerals in Table 6 shows that their agreement can be quite good if the mineral's entropy is less than 30 cal/mole-deg but that the accuracy diminishes as the entropy and therefore the structural complexity of the mineral increases. Because rankinite, spurrite and tilleyite are all relatively complex, this method of estimation would be of dubious value. However, Fyfe et al. were able to refine this method of estimation by noting that there is a relationship between the entropy and molar volume of a mineral, as evidenced by

$$\left(\frac{\partial S_{\phi}}{\partial V_{\phi}}\right)_{T} = \frac{\alpha_{\phi}}{\chi_{\phi}} \qquad (8)$$

where α and χ represent the ϕth mineral's coefficients of thermal expansion and compressibility, respectively. They developed this relationship into the following equation which can be used to estimate the standard third law entropy of a mineral:

$$S^{\circ}_{298.15,\phi} = \Sigma n_i S^{\circ}_{298.15,i} - 0.6\ (\Sigma n_i V^{\circ}_i - V^{\circ}_{\phi}) \qquad (9)$$

where i represents the oxide under consideration and n_i refers to the number of moles of the ith oxide in one mole of the mineral.

Beane (1975) suggested that the average correction factor of 0.6 proposed by Fyfe et al. might actually be a value which reflects changes in the composition and/or structure of minerals. The replacement of 0.6 by a variable specific to minerals of certain mineralogical or structural

Table 6. Comparison of standard third law entropies estimated by the summation of the entropies of oxides per Fyfe et al. (1958) with tabulated values from Robie and Waldbaum (1968).

Mineral Name	$S^{o}_{298.15}$, calculated [a]	$S^{o}_{298.15}$, tabulated [b]
Akermanite	45.20	50.03 ± 0.50
B-larnite	28.88	30.50 ± 0.20
Ca-olivine	28.88	28.80 ± 0.20
Clinoenstatite	16.32	16.22 ± 0.10
Diopside	35.70	34.20 ± 0.20
Forsterite	22.76	22.75 ± 0.20
Merwinite	54.70	60.5 ± 0.5
Monticellite	25.82	24.5 ± 1.0
Wollastonite	19.38	19.60 ± 0.20

[a] calculated by summation of the entropies of oxides tabulated by Robie and Waldbaum (1968) per Fyfe et al. (1958) (in cal/mole-deg)

[b] from Robie and Waldbaum (1968) (in cal/mole-deg)

groups might then result in more accurate reproduction of $S^{o}_{298.15}$ values. This volume correction factor could be obtained from a group of minerals related by structure or composition with known $S^{o}_{298.15}$ and V^{o}, and the average value of that factor could then be used to estimate $S^{o}_{298.15}$ for other minerals belonging to that group for which entropies have not been measured. Beane accordingly proposed two equations which could be solved for k' and k" (the equivalent of 0.6 in equation 9) for similar groups of minerals of known thermodynamic properties in order to calculate the $S^{o}_{298.15}$ of a related mineral or minerals:

$$\frac{S^{o}_{298.15,\,\phi}}{V^{o}_{\phi}} = k' \cdot \frac{\Sigma n_i S^{o}_{298.15,\,i}}{\Sigma n_i V^{o}_{i}} \qquad (10)$$

$$S^{o}_{298.15,\,\phi} - \Sigma n_i S^{o}_{298.15,i} = k'' \,(V^{o}_{\phi} - \Sigma n_i V^{o}_{i}) \qquad (11)$$

To evaluate the accuracy of these equations in estimating $S^{o}_{298.15}$ of a mineral, k' and k" were calculated using $S^{o}_{298.15}$ and V^{o} data for a) a set of cyclosilicates and nesosilicates and b) a set of Ca-Mg silicates. These values were then used to determine an average k' and k" for each grouping. Utilizing these values of k' (equal to 0.99 and 1.03 for a and b, respectively) and k" (equal to -0.09 and -0.14 for a and b, respectively) in equations (10) and (11), the standard third law entropies of the minerals were recalculated to test each method's accuracy in reproducing tabulated $S^{o}_{298.15}$ values in Robie and Waldbaum and to determine whether grouping by structure or composition yielded the best estimates. The results are shown in Table 7 along with the estimates made using equation (9) of Fyfe et al., for comparison.

Table 7. Estimation of the standard third law entropies of minerals per Beane (1975) and Fyfe et al. (1958).

Nesosilicates and cyclosilicates			$S^{o\ a}_{298.15}$, calculated		$S^{o\ a}_{298.15}$, calculated	$S^{o\ c}_{298.15}$, tabulated
Mineral Name	k'	k"	with k'	with k"	per Fyfe et al.(1958)	
Akermanite	1.08	1.82	46.07	44.96	46.80	50.03 ± 0.50
Andalusite	0.95	0.07	23.31	21.77	24.02	22.28 ± 0.10
Ca-olivine	0.95	-0.03	30.07	28.62	30.62	28.80 ± 0.20
Cordierite	0.90	0.23	106.91	82.49	114.31	97.33 ± 0.90
Fayalite	0.92	11.57[b]	38.28	38.95	38.74	35.45 ± 0.40
Forsterite	1.03	0.01	21.83	22.89	21.92	22.75 ± 0.20
Gehlenite	1.05	0.75	44.85	40.30	46.13	47.4 ± 0.4
Grossularite	0.94	0.68	60.61	72.00	59.14	57.7 ± 1.3
Merwinite	1.13	-2.31	52.88	54.93	53.19	60.5 ± 0.5
Monticellite	0.94	-2.00	25.89	25.76	26.22	24.5 ± 1.0
AVERAGE	0.99	-0.09				

Table 7. cont.

Ca-Mg silicates			$S^{o}_{298.15}$, calculated		$S^{o}_{298.15}$, calculated	$S^{o}_{298.15}$, tabulated
Mineral Name	k'	k"	with k'	with k"	per Fyfe et al. (1958)	
Akermanite	1.08	1.82	47.93	44.83	46.80	50.03 ± 0.50
Ca-olivine	0.95	-0.03	31.28	28.47	30.62	28.80 ± 0.20
Clinoenstatite	1.07	0.04	15.59	16.67	14.84	16.22 ± 0.10
Diopside	1.06	0.21	33.11	36.72	31.32	34.20 ± 0.20
Forsterite	1.03	0.01	22.72	22.96	21.92	22.75 ± 0.20
Merwinite	1.13	-2.31	55.02	55.05	53.19	60.5 ± 0.5
Monticellite	0.94	-2.00	26.94	25.73	26.22	24.5 ± 1.0
Tremolite	0.99	0.54	136.16	143.44	130.11	131.19 ± 0.30
Wollastonite	1.00	0.46	20.20	19.31	19.67	19.60 ± 0.20
AVERAGE	1.03	-0.14				

[a] in cal/mole-deg

[b] omitted from the average owing to its anomalous value

[c] from Robie and Waldbaum (1968) (in cal/mole-deg)

Beane's methods of estimation utilizing k' and k" values work reasonably well for both groupings with an error of less than $\pm$ 1.5 cal/mole-deg in both cases when $S^{o}_{298.15}$ of a mineral is less than 30 cal/mole-deg. In general, however, the error is quite variable, although there does seem to be a trend toward greater discrepancies between the estimated and tabulated values of $S^{o}_{298.15}$ when the mineral becomes structurally complex. It appears, at least in this case, that grouping by composition versus grouping by structure does not result in significant differences between the estimated values of $S^{o}_{298.15}$. The values of $S^{o}_{298.15}$ estimated by Fyfe et al. show about the same degree of deviation from the tabulated values as the estimates using Beane's method. But, again the error is quite variable and seems to indicate that there is more than just a simple relationship between entropy and volume that affects the standard third law entropy of some minerals.

Even if the aforementioned methods of approximation were accurate enough for the purposes of this study, a problem is encountered when dealing with the generation of data for spurrite and tilleyite because these minerals contain CO_2 for which entropy and volume data are lacking at 25°C and 1 bar.

It may be possible to estimate the entropy contribution of the CO_2 component by subtracting the previously calculated entropy contributions of the CaO and MgO components from a number of carbonates to isolate the entropy supposedly contributed to each carbonate by CO_2. An average of these values would then represent the average contribution of the CO_2 component to the entropy of the carbonates. This procedure is illustrated in Table 8 along with the entropies of the carbonates calculated in this manner. Again, errors range from $\pm$ 0.3 to 1.7 cal/mole-deg.

Table 8. Estimation of the entropy contribution of CO_2 to carbonate minerals.

Mineral Name	$S^{o\ a}_{298.15,tab.}$	$S^{o\ b}_{298.15,CO_2 cont.}$	$S^{o\ c}_{298.15,calc.}$
Aragonite	21.18 ± 0.30	9.21	20.68
Calcite	22.15 ± 0.20	10.18[d]	20.68
Dolomite	37.09 ± 0.07	8.92[e]	36.67
Huntite	67.0 ± 1.5	8.29[e]	68.68
Magnesite	15.7 ± 0.2	8.41	16.00
		AVERAGE 8.71	

[a] from Robie and Waldbaum (1968) (in cal/mole-deg)

[b] $S^o_{298.15,CO_2\ cont.} = (S^o_{298.15,\ tab.} - \sum_1^j \nu_j S^o_{298.15,j})$ where

j refers to all oxides except CO_2 (in cal/mole-deg)

[c] in cal/mole-deg

[d] omitted from average owing to its anomalous value

[e] corrected to show contribution per each mole of CO_2 in the mineral

The method of "oxide contribution" developed earlier to estimate the heat capacity power functions of minerals was relatively successful, and therefore an analogous procedure was followed to calculate the individual contributions of the CaO, MgO, SiO_2 and CO_2 components as integral parts of a mineral to a mineral's standard third law entropy. The minerals akermanite, B-larnite, clinoenstatite, diopside, forsterite, merwinite and monticellite in the system CaO-MgO-SiO_2 with experimentally determined values of $S^o_{298.15}$ were used to set up a series of simultaneous equations in the form

$$S^o_{298.15,\emptyset} = a_1 n_{CaO,\emptyset} + a_2 n_{MgO,\emptyset} + a_3 n_{SiO_2,\emptyset} \qquad (12)$$

where $S^o_{298.15,\emptyset}$ is the standard third law entropy of the $\emptyset$th mineral, $n_{i,\emptyset}$ represents the coefficient of the ith oxide in the $\emptyset$th mineral, and a_i are coefficients representing the contribution of each of the component oxides to the entropy of the mineral. These simultaneous equations were then solved by means of a least square regression for the values of a_1, a_2 and a_3 which represent the contribution of the CaO, MgO and SiO_2 components, respectively, to the standard third law entropies of the silicate minerals. Table 9 lists the results of these calculations and also compares the experimentally determined values of $S^o_{298.15}$ of the minerals involved in these estimations to the corresponding values of $S^o_{298.15}$ estimated using the calculated contributions of the CaO, MgO and SiO_2 components as integral parts of a mineral to its entropy.

Equation (11) of Fyfe et al. states that there is a relationship between the entropy and volume of a mineral and its component oxides.

Table 9. Contribution of the oxide components CaO, MgO and SiO_2 to the entropy of a mineral.

Entropy contribution of:

CaO = 11.97 cal/mole-deg

MgO = 7.29 cal/mole-deg

SiO_2 = 8.16 cal/mole-deg

Mineral Name	$S^{o\ a}_{298.15}$, calculated	$S^{o\ b}_{298.15}$, tabulated
Akermanite	47.55	50.03 ± 0.50
B-larnite	32.10	30.50 ± 0.20
Clinoenstatite	15.45	16.22 ± 0.10
Diopside	35.58	34.20 ± 0.20
Forsterite	22.74	22.75 ± 0.20
Merwinite	59.52	60.5 ± 0.5
Monticellite	27.42	24.5 ± 1.0
Wollastonite	20.13	19.60 ± 0.20

[a] in cal/mole-deg

[b] from Robie and Waldbaum (1968) (in cal/mole-deg)

Because the problem now encountered is one in which the entropy and volume of one of the components (CO_2) is unknown, it would be convenient to separate the $S^o_{298.15,CO_2}$ and $V^o_{CO_2}$ terms from the main body of equation (11) to obtain

$$(S^o_{298.15,\emptyset} - \Sigma n_j S^o_{298.15,j}) = m\,(V^o_{\emptyset} - \Sigma n_j V^o_j) + (S^o_{298.15,CO_2} - mV^o_{CO_2}) \qquad (13)$$

in which k'' has been replaced by m and j refers to all oxides except CO_2. Equation (13) is, essentially, the equation of a line in the form $y = mx + b$ where $b = (S^o_{298.15,CO_2} - mV^o_{CO_2})$. A group of n minerals containing CO_2 with known $S^o_{298.15}$ and V^o can be used to set up n simultaneous equations in the form of equation (13) which can be solved for m and b. In this manner, the need to know the exact values of $S^o_{298.15,CO_2}$ and $V^o_{CO_2}$ is circumvented by isolating these values in the b term, which is evaluated from available data on carbonate minerals. Once m and b have been established, $S^o_{298.15}$ for CO_2-bearing minerals can be calculated by evaluating equation (13). Table 10 lists the results of one representative calculation using this method. Application of the constants derived in this manner to the estimation of $S^o_{298.15}$ for spurrite and tilleyite requires the assumption that the CO_2 component of these minerals is thermodynamically similar to the carbonates from which m and b were calculated.

To estimate the contribution of the CO_2 component to entropy, the data of a group of silicates and carbonates was regressed to simultaneously determine the entropy contributions of the CaO, MgO, SiO_2 and CO_2 components in these minerals. The procedure followed is the same as described above. Five carbonates (aragonite, calcite, dolomite, huntite, and magnesite) and eight silicates (akermanite, B-larnite, clinoenstatite, diopside,

Table 10. Estimation of the standard third law entropies of minerals per equation (13) in text. See text for explanation of symbols.

Mineral Name	$S^{o\ a}_{298.15,\emptyset,tab.}$	$\Sigma n_j S^{o\ a}_{298.15,j}$	$V^{o\ b}_{\emptyset}$	$\Sigma n_j V^{o\ b}_{j}$	$S^{o\ c}_{298.15,\emptyset,calculated}$
Calcite	22.15 ± 0.20	9.5	36.934	16.76	20.55
Dolomite	37.09 ± 0.07	(9.5+6.44)	64.34	(16.76+11.25)	36.84
Aragonite	21.18 ± 0.30	9.5	34.15	16.76	19.69
Witherite	26.8 ± 0.5	16.8	45.81	25.59	27.87
Otavite	23.3 ± 0.6	13.1	34.3	15.585	23.70
Siderite	25.1 ± 0.6	14.52	29.378	12.00	24.71
Magnesite	15.7 ± 0.2	6.44	28.018	11.25	16.44
Huntite	67.0 ± 1.5	(3*6.44+9.5)	122.58	(3*11.25+16.76)	70.36
Rhodochrosite	23.90 ± 0.50	14.27	31.073	13.221	24.60
Strontianite	23.2 ± 0.4	13.0	39.01	20.69	23.48
Smithsonite	19.70 ± 0.30	10.43	28.275	14.338	19.55

Solving equation (13) -- $(S^{o}_{298.15,\emptyset} - \Sigma n_j S^{o}_{298.15,j}) = m(V^{o}_{\emptyset} - \Sigma n_j V^{o}_{j}) + (S^{o}_{298.15,CO_2} - mV^{o}_{CO_2})$
for m and b yields: m= 0.31, b = 4.80.

[a] from Robie and Waldbaum (1968) (in cal/mole-deg)

[b] from Robie and Waldbaum (1968) (in cm^3/mole)

[c] calculated according to equation (13) with m = 0.31, b = 4.80 (in cal/mole-deg)

forsterite, merwinite, monticellite and wollastonite) were included in the calculations. The addition of the carbonates permitted the estimation of the entropy contribution of the CO_2 component and served to refine the estimation of the contributions of the CaO and MgO components. Results are shown in Table 11. This and the previous method of estimation generally involve errors ranging from $\pm$ 0.5 to 3 cal/mole-deg.

The calculations above indicate that one method of estimation does not appear to be superior to the others; that is, each method involves some error in estimating the entropy of minerals and the error is inevitably greater for some minerals than others. Because there does seem to be a correlation between the increasing entropy of a mineral and the increasing error in the reproduction of the tabulated $S^{\circ}_{298.15}$ values, the error would seem to reflect upon the structural complexity of the mineral.

The method of estimation of heat capacities by the summation of the heat capacity contributions of the component oxides developed earlier in this paper was found to be quite accurate in reproducing experimental results; inherent in this method of estimation is the assumption that there is no interaction between the component oxides which would affect a mineral's heat capacity. However, when the same method of estimation was used to calculate the standard third law entropy of a mineral, agreement between the calculated and tabulated values was noticeably poorer. This would suggest that there is significant component interaction that affects the entropy of a mineral, and therefore average values of the contributions of the oxide components cannot account for the varying amounts of component interaction in minerals ranging from the structurally simple to complex.

Table 11. Contribution of the oxide components CaO, MgO, SiO_2 and CO_2 to the entropy of a mineral.

Entropy contribution of:

CaO = 12.09 cal/mole-deg

MgO = 6.88 cal/mole-deg

SiO_2 = 8.36 cal/mole-deg

CO_2 = 8.80 cal/mole-deg

(Note: the entropies calculated in this manner must include a factor of -0.11 cal/mole-deg which represents the intercept generated by the method of multiple regression used.)

Mineral Name	$S^{o\ a}_{298.15}$, calculated	$S^{o\ b}_{298.15}$, tabulated
Aragonite	20.78	21.18 ± 0.30
Calcite	20.78	22.15 ± 0.20
Dolomite	36.46	37.09 ± 0.07
Huntite	67.82	67.0 ± 1.5
Magnesite	15.57	15.7 ± 0.2
Akermanite	47.67	50.03 ± 0.50
B-larnite	32.43	30.50 ± 0.20
Clinoenstatite	15.13	16.22 ± 0.10
Diopside	35.58	34.20 ± 0.20
Forsterite	22.01	22.75 ± 0.20
Merwinite	59.76	60.5 ± 0.5
Monticellite	27.22	24.5 ± 1.0
Wollastonite	20.34	19.60 ± 0.20

[a] in cal/mole-deg

[b] from Robie and Waldbaum (1968) (in cal/mole-deg)

This problem of estimation may also be viewed in a slightly different manner. It is known that

$$\left(\frac{\partial G}{\partial T}\right)_p = -S \qquad \text{and} \qquad \left(\frac{\partial S}{\partial T}\right)_p = \frac{Cp}{T} \qquad (14, 15)$$

or, alternately,

$$S = \int \frac{Cp}{T}\, dT + c_1 \quad \text{and} \quad G = -\int \left(\int \frac{Cp}{T}\, dT + c_1\right) dT + c_2 \qquad (16, 17)$$

where c_1 and c_2 represent integration constants. According to these equations, G, S and C_p form, in effect, a hierarchy of functions with G of the highest and C_p of the lowest order. Earlier in this paper, it was found that although the summation of individual oxide contributions to the heat capacity of a mineral reproduces experimental results quite well, the same method of estimation is not as accurate when dealing with standard third law entropies, which inaccuracy was attributed to the effects of component interaction. Equations (14) to (17) reveal that although C_p might be a fundamental thermodynamic quantity, it must be integrated over temperature and added to c_1, an integration constant, to obtain the higher order function of entropy. This integration constant c_1 can be thought of as the component interaction that contributes to the entropy of a mineral. (It can also be considered $S^o_{298.15}$.) In general, the more complex the mineral or the greater its number of components, the larger this term is going to be. S may be integrated in turn (equation 17) to obtain G, a still higher order function, provided another integration constant, c_2, is known. However, these integration constants have not been determined, and thus it would be unrealistic to estimate G with the summation methods used for heat capacities.

Because the methods of estimation of the standard third law entropy of a mineral result in, at best, rough approximations of the actual values, the entropies of rankinite, spurrite and tilleyite were calculated using each method that was applicable and then averaged in hopesof reducing the amount of random error; these calculations are shown in Table 12. The estimations by simple summation of the pure oxides' entropies as tabulated by Robie and Waldbaum (1968) were omitted from all the averages owing to their discrepancy with the other values and the fact that this method seems to become significantly less accurate as entropies increase in value. Increasing values generally correspond to more complex chemical formulas, indicating increased component interaction and thus increased discrepancy between the estimated and tabulated entropies.

The standard third law entropies of spurrite and tilleyite calculated in this study are 81.63 and 91.81 cal/mole-deg, respectively. The estimated entropy of rankinite was 52.23 cal/mole-deg because the other methods of estimation took CO_2 into account and therefore introduced a possible source of error in the estimation of the entropy of a CO_2-poor Ca-silicate mineral such as rankinite.

These preliminary estimates of the standard third law entropies of rankinite (52.23 cal/mole-deg), spurrite (81.63 cal/mole-deg) and tilleyite (91.81 cal/mole-deg) will be refined with actual experimental data after ΔH_f^o values have been established for spurrite and tilleyite by using the relationship between the slopes of equilibrium curves and the entropy and volume change of reaction (i.e., the Clapeyron equation).

Table 12. Calculation of the standard third law entropies of rankinite, spurrite and tilleyite.

Method of Estimation	$S^{o}_{298.15}$ (cal/mole-deg)		
	Rankinite	Spurrite	Tilleyite
1)	48.26[a]	75.97[a]	84.68[a]
2)	52.23	84.88	93.59
3)	____	85.75	94.66
4)	____	77.79	89.64
5)	____	78.10	89.34
"AVERAGE"	52.23	81.63	91.81

Key to methods of approximation:

1) stochiometric summation of experimentally determined entropies of the pure oxides from Robie and Waldbaum (1968) per Fyfe et al. (1958)

2) stochiometric summation of the contributions of the CaO and SiO_2 components to entropy (Table 6) and the average entropy contribution of the CO_2 component to minerals (Table 8)

3) stochiometric summation of the contributions of CaO, SiO_2 and CO_2 components to entropy with -0.11 correction factor (Table 7)

4) solution of equation (13) in text (Table 5)

5) same as 4) except for addition of cerussite to minerals used to calculate m and b (m = 0.095, b = 9.08)

[a] omitted from average as explained in text

Enthalpy

A mineral's standard enthalpy of formation from the elements can be determined using experimental equilibrium curves for reactions in which the mineral is involved, provided that complete thermodynamic data is available for all phases in the reaction except for the enthalpy of formation of the mineral under consideration. That is, if an equilibrium point at a specific temperature and pressure has been experimentally determined for some reaction, knowledge of all the thermodynamic properties of the phases involved except for one property of one phase allows the calculation of that unknown thermodynamic property. For this study in particular, the enthalpies of spurrite and tilleyite were calculated using entropies and heat capacity power functions already estimated and which, for the time being, are assumed to be reasonably correct.

At some temperature T and pressure P, the free energy change for a reaction $\Delta G_{r,T,P}$ is written

$$\Delta G_{r,T,P} = \Delta G^{o}_{r,T,P} + RT\ln Q_{r,T,P} \qquad (18)$$

where $\Delta G^{o}_{r,T,P}$ is the standard Gibbs free energy of reaction at T and P and Q represents the activity product of the reaction at T and P, viz.

$$Q_{r,T,P} = \Sigma a_i^{\nu_i} \qquad (19)$$

in which i refers to the phases or species involved in the reaction and ν represents their reaction coefficients. If this temperature and pressure is such that the reaction is at equilibrium, then

$$\Delta G_{r,T,P} = 0 \qquad (20)$$

and hence

$$\Delta G^\circ_{r,T,P} = - RT\ln K_{r,T,P} \qquad (21)$$

where Q = K at equilibrium. $\Delta G^\circ_{r,T,P}$ may be calculated according to the standard states chosen in this paper by evaluating

$$\Delta G^\circ_{r,T,P} = \Delta H^\circ_{r,T,P} - T\Delta S^\circ_{r,T,P}$$

$$= \Delta H^\circ_{r,Tr,Pr} + \int_{Tr}^{T} \Delta Cp_r \, dT + \int_{Pr}^{P} (\Delta V_{sol,liq,T}) \, dP$$

$$- T \left(\Delta S^\circ_{r,Tr,Pr} + \int_{Tr}^{T} (\Delta Cp_r/T) \, dT\right)^a \qquad (22)$$

in which sol and liq refer to the solids and liquids involved in the reaction and Tr and Pr represent the reference temperature and pressure.

However, in this case, ΔH°_f of one of the phases is unknown. If equation (22) is evaluated at some equilibrium temperature and pressure assuming $\Delta H^\circ_f = 0$ for phase u, the $\Delta G^\circ_{r,T,P}$ so calculated and designated as $\Delta G^\circ_{r,T,P,22}$ will be related to the true $\Delta G^\circ_{r,T,P}$ by

$$\Delta G^\circ_{r,T,P,22} + \nu_u \Delta H^\circ_{f,u} = \Delta G^\circ_{r,T,P} \qquad (23)$$

where ν_u refers to the reaction coefficient of the uth phase. Equation (23) can then be combined with equation (21) and rearranged to yield the unknown standard enthalpy of formation from the elements,

$$\nu_u \Delta H^\circ_{f,u} = -RT\ln K_{r,T,P} - \Delta G^\circ_{r,T,P,22} \, . \qquad (24)$$

[a] The term $\Delta V_{sol,liq,T}$ is taken to be pressure independent based on the simplifying assumption that the net compressibility and thermal expansion of the condensed phases is negligible, and therefore $\int_{Pr}^{P} (\Delta V_{sol,liq,T}) dP$ can be approximated by $\Delta V_{sol,liq,T}(P-P_r)$.

When a dehydration or decarbonation reaction is studied,

$$K_{r,T,P} = \Sigma a_i^{\nu_i} \qquad (25)$$

where a_i are the activities of the gases involved in the reaction raised to the power represented by their reaction coefficients. If $\Delta G^{o}_{r,T,P,22}$ and the activities of the gases at the specified temperature and pressure can be determined, it is possible, using equation (24), to calculate the enthalpy of a mineral because of the need to maintain equilibrium at that temperature and pressure.

The activity of CO_2 will be approximated by its fugacity in the following calculations because γ^{o}, the fugacity coefficient for CO_2 in the standard state (i.e., any specified temperature and 1 bar), is nearly equal to unity at the temperatures involved in this study. Later in the paper this concept will be discussed in more detail.

Harker (1959) published experimentally determined equilibrium points for the reactions

$$2\ CaSiO_3 + 3\ CaCO_3 \rightleftharpoons Ca_5Si_2O_7(CO_3)_2 + CO_2 \qquad (7)$$

and

$$Ca_5Si_2O_7(CO_3)_2 \rightleftharpoons 2Ca_2SiO_4 \cdot CaCO_3 + CO_2\ ; \qquad (8)$$

Zharikov and Shmulovich repeated his high-temperature experiments in 1970. A comparison of the two sets of decarbonation curves reveals that the equilibria determined by Zharikov and Shmulovich lie at significantly higher temperatures than those of Harker at a given pressure. This may be a result of the fact that Harker, for some reason unknown to him, could not synthesize tilleyite without the use of CaF_2 and Al_2O_3 as fluxes,

whereas Zharikov and Shmulovich were able to synthesize tilleyite without resorting to fluxes of any sort. Few workers have explored the system $CaO-MgO-SiO_2-CO_2$ experimentally at high temperatures, much less in the detail that Zharikov and Shmulovich did. Because their work is the most recent and complete, and did not depend on the use of fluxes which could possibly affect equilibrium among the phases, their experimental data was utilized to calculate ΔH_f^o of spurrite and tilleyite as well as to refine the $S^o_{298.15}$ values of these phases. It should be remembered, of course, that the accuracy of the thermodynamic data calculated in the manner described above is dependent on the accuracy of their experimental data.

Inspection of Zharikov and Shmulovich's (1970) data yielded well-defined experimental brackets at three pressures for the reaction

$$2\ CaSiO_3 + 3\ Ca\ CO_3 \rightleftharpoons Ca_5Si_2O_7(CO_3)_2 + CO_2 \quad . \qquad (7)$$

With the knowledge of all pertinent thermodynamic data for the phases involved in the reaction except the ΔH_f^o of tilleyite, equation (24) can be used in conjunction with equation (22) as previously described to calculate ΔH_f^o of tilleyite at each of the equilibrium points. The results, listed in Table 13, show that the calculated values of ΔH_f^o of tilleyite agree with each other amazingly well. The average of these three values, -1524261 cal/mole, has an error limit of $\pm$ 100 cal/mole, a very small range when compared to the magnitude of the enthalpy of tilleyite. This high degree of correlation would seem to indicate that the standard third law entropy previously estimated for tilleyite is reasonably accurate.

Having estimated a value of ΔH_f^o for tilleyite, the equilibrium curve for reaction (7) can now be calculated directly from thermodynamic data and compared to that curve determined experimentally by Zharikov and

Table 13. Estimation of the standard enthalpies of formation of tilleyite and spurrite

$2\ CaSiO_3 + 3\ CaCO_3 \rightleftharpoons Ca_5Si_2O_7(CO_3)_2 + CO_2$

Temperature (°C)	Pressure (kg/cm^2)	ΔH_f^o (cal/mole)
885 ± 5	200	-1524368
955 ± 5	350	-1524183
995 ± 5	500	-1524232
	AVERAGE	-1524261

$Ca_5Si_2O_7(CO_3)_2 \rightleftharpoons 2Ca_2SiO_4 \cdot CaCO_3 + CO_2$

Temperature (°C)	Pressure (kg/cm^2)	ΔH_f^o (cal/mole)
855 ± 5	100	-1395837
935 ± 5	200	-1395326
995 ± 5	300	-1394815
1050 ± 10	500	-1394838
	AVERAGE	-1395204.

[a]Kg/cm^2 equated with bars because 1.0197 kg/cm^2 = 1 bar.

Shmulovich. If the two curves coincide, the accuracy of the thermodynamic data estimated for tilleyite will be confirmed. However, if the two curves do not coincide, whether in position or slope, the estimated thermodynamic data for tilleyite must be manipulated, observing various thermodynamic restrictions, such that the two will coincide more closely. This procedure, of course, requires the assumption that the thermodynamic data for the other phases in the reaction is correct and that all the error is contained in the estimated data. The means by which equilibrium curves on pressure-temperature diagrams are constructed will be described in detail later in the paper. For the time being, however, it is sufficient to note that it is possible to calculate pressure-temperature topologies wholly on the basis of thermodynamic data.

The equilibrium curve for reaction (7), calculated using $S^{o}_{298.15}$ = 91.81 cal/mole-deg and ΔH^{o}_{f} = -1524260 cal/mole for tilleyite, is shown in Figure 8 along with the experimentally determined curve of Zharikov and Shmulovich. The calculated curve does indeed go through all the experimental brackets surrounding the equilibrium curve of Zharikov and Shmulovich and thus the accuracy of the estimated thermodynamic data for tilleyite is verified: ΔH^{o}_{f} = -1524260 $\pm$ 100 cal/mole and $S^{o}_{298.15}$ = 91.81 cal/mole-deg.

ΔH^{o}_{f} of spurrite was calculated using four well-defined equilibrium points on the pressure-temperature curve for the reaction

$$Ca_5Si_2O_7(CO_3)_2 \rightleftharpoons 2Ca_2SiO_4 \cdot CaCO_3 + CO_2 \qquad (8)$$

as determined by Zharikov and Shmulovich. Table 13 lists the results: ΔH^{o}_{f} = -1395204 $\pm$ 600 cal/mole. The equilibrium curve for reaction (8), back calculated using ΔH^{o}_{f} = -1395200 cal/mole and $S^{o}_{298.15}$ = 81.63 cal/mole-deg

for spurrite and the data just calculated for tilleyite, was found to be steeper than the corresponding curve of Zharikov and Shmulovich on a plot of temperature as the abscissa and pressure as the ordinate (see Figure 9). The slope of an equilibrium curve on a pressure-temperature diagram is related to the entropy and volume change of the reaction by the Clapeyron equation:

$$\left(\frac{dP}{dT}\right) = \left(\frac{\Delta Sr}{\Delta Vr}\right) . \qquad (26)$$

According to this equation, a change in the slope of the reaction curve above may be affected by a change in the estimated $S^{o}_{298.15}$ of spurrite. However, because we are working with a curve along which equilibrium has been established, ΔH_r must change accordingly to maintain equilibrium. This, in turn, means that ΔH^{o}_{f} of spurrite must be adjusted. That is, at equilibrium,

$$\Delta G_{r,T,P} = \Delta H_{r,T,P} - T\Delta S_{r,T,P} = 0, \qquad (27)$$

and if the entropy of spurrite is altered, the estimated enthalpy of spurrite must also change to maintain $\Delta G_{r,T,P} = 0$ because the thermodynamic data for all the other phases is assumed to be correct. Therefore, as each new $S^{o}_{298.15}$ is chosen, a corrected ΔH^{o}_{f} of spurrite must be calculated using equations (22) and (24) and the method established earlier for calculation of ΔH^{o}_{f} of a mineral. The ΔH^{o}_{f} obtained in this manner can be used with the revised $S^{o}_{298.15}$ of spurrite to recalculate the pressure-temperature curve. If the curve fails to match the experimental curve, the process must be repeated, and so on until the curves correspond as closely as possible. However, because the entropy estimated for tilleyite worked so well in reproducing the slope of the equilibrium curve of Zharikov and Shmulovich , it was assumed that the

estimated value of $S^{o}_{298.15}$ for spurrite would be of reasonable accuracy also. Therefore, spurrite's entropy was assumed to be correct and no attempt was made to equalize the slopes of the calculated and experimental equilibrium curves, leaving ΔH^{o}_{f} = -1395200 ± 600 cal/mole and $S^{o}_{298.15}$ = 81.63 cal/mole-deg.

Weeks (1956) lists ΔH^{o}_{f} = -945435 cal/mole for rankinite, but there appears to be no published value of $S^{o}_{298.15}$ available for that mineral. Assuming this enthalpy of rankinite to be correct, points along the equilibrium curve of Zharikov and Shmulovich for the reaction

$$Ca_5Si_2O_7(CO_3)_2 + 4\ CaSiO_3 \rightleftharpoons 3Ca_3Si_2O_7 + 2CO_2 \qquad (9)$$

were utilized to back calculate $S^{o}_{298.15}$ of rankinite in a manner analogous to that used to calculate ΔH^{o}_{f} of a mineral when all other pertinent thermodynamic data is known. The entropy calculated in this manner was 48.3 cal/mole-deg as compared to the previously estimated value of 52.23 cal/mole-deg. The equilibrium curve for the above reaction calculated with $S^{o}_{298.15}$ = 48.3 cal/mole-deg for rankinite corresponds very well with the experimental curve of Zharikov and Shmulovich. Thus, the thermodynamic data used for rankinite in this study is: $S^{o}_{298.15}$ = 48.3 cal/mole-deg and ΔH^{o}_{f} = -945435 cal/mole.

DESCRIPTION OF MINERAL EQUILIBRIA AS A FUNCTION OF PHYSICAL PARAMETERS

Introduction

The influence of the physical factors of temperature and pressure upon isochemical mineral equilibria is conveniently represented by means of pressure-temperature diagrams. Metamorphic reactions among minerals plotted on such diagrams serve to delineate changes in prevailing mineral assemblages upon variation in these factors. The reactions, represented by equilibrium curves, are univariant because any change of temperature or pressure requires a corresponding change in the other variable to maintain a dynamic equilibrium between the reactants and products. If CO_2 or H_2O is taking part in the reaction, it is considered a pure phase with a = 1.0. However, this approach is unrealistic in terms of natural systems because unmetamorphosed siliceous dolomitic limestones contain interstitial water and during the metamorphism of these rocks, CO_2 is released to mix with the H_2O phase in varying proportions. Therefore, one is not actually dealing with pure H_2O or CO_2 but rather a fluid phase composed of a mixture of the two gases.

According to the phase rule,

$$P + F = C + 2 \qquad (28)$$

where P is equal to the number of phases, F represents the number of degrees of freedom and C is the number of components. Normally, the thermodynamic degrees of freedom correspond to temperature, pressure and the number of moles of each of the components occurring in the system. A mixture of CO_2 and H_2O in the fluid phase, however, would add a degree

of freedom to the reaction because the number of components has increased by one while there is still a single fluid phase. This additional degree of freedom corresponds to variation in the composition of the fluid phase. Even if H_2O or CO_2 does not appear specifically in a given reaction, it still contributes to the total pressure. Thus, decarbonation reactions may be considered bivariant in systems containing H_2O and CO_2 (Winkler, 1974). Workers such as Greenwood (1962), Metz and Trommsdorf (1968) and Winkler (1967, 1974) have found it convenient to represent the effects of the changing composition of the fluid phase with temperature-mole fraction CO_2 diagrams. Because the reactions are bivariant and pressure, temperature and mole fraction of CO_2 (designated as X_{CO_2}) are all possible variables, total pressure must be fixed in such diagrams.

Temperature-pressure and temperature-X_{CO_2} diagrams can both be constructed entirely with thermodynamic data. If the correspondence between the thermochemical and experimental curves on these diagrams is relatively good, the thermochemical calculations may serve to construct equilibrium curves when experimental data is lacking, incomplete or of dubious accuracy, and may even shed light on discrepancies between experimental curves.

Pressure-Temperature Diagrams

The construction of univariant equilibrium curves on pressure-temperature diagrams is relatively simple and will be illustrated with the hypothetical decarbonation reaction

$$A \rightleftharpoons B + \nu CO_2 \quad . \qquad (29)$$

For this reaction

$$\log K_{r,T,P} = \log \left(\frac{a_B a_{CO_2}^{\nu_{CO_2}}}{a_A} \right) = \log a_{CO_2}^{\nu_{CO_2}} \qquad (30)$$

according to the standard state chosen in this paper. The activity of CO_2 can be approximated by its fugacity at relatively high temperatures and low pressures because γ^o, the fugacity coefficient of pure CO_2 at some temperature and the reference pressure, is nearly equal to unity under these conditions. That is,

$$a = \frac{f}{f^o} = \frac{\gamma P}{\gamma^o P^o} \simeq f \qquad (31)$$

where f and f^o represent the fugacity of CO_2 at the temperature and pressure (P) under consideration and at the reference temperature and pressure (P^o), respectively, because P^o is defined to be unity by the choice of standard states in this paper and γ^o is equal to unity as described above.

Therefore,

$$\log K_{r,T,P} \simeq \log f_{CO_2}^{\nu_{CO_2}} \quad . \qquad (32)$$

Log $K_{r,T,P}$ can also be calculated with equation (22) and the relation

$$\log K_{r,T,P} = \frac{-\Delta G^o_{r,T,P}}{2.303\ RT} \qquad (21)$$

using thermodynamic data for the phases involved in the reaction. Equations (21) and (32) show that the calculated value of log $K_{r,T,P}$ must equal log $f_{CO_2}^{\nu_{CO_2}}$ at equilibrium. It is possible to plot log $K_{r,T,P}$ as calculated with equations (22) and (21) versus temperature at a specified pressure, and then to compare that plot with another, at the same scale, of log $f_{CO_2}^{\nu_{CO_2}}$ versus temperature at the same pressure. The intersection of the two curves represents the temperature at which log $K_{r,T,P}$ = log $f_{CO_2}^{\nu_{CO_2}}$

or, to be more specific, the equilibrium temperature for the reaction at that pressure. If this procedure is repeated at a series of pressures, a sequence of equilibrium points will be obtained which, when plotted on a pressure-temperature diagram, will represent the univariant equilibrium curve for the reaction.

Necessary log f_{CO_2} values were obtained from the work of Ryzhenko and Volkov (1971) for temperatures from 100° to 1000°C and pressures from 1500 to 5000 bars. For pressures from 100 to 1400 bars over the same temperature range, the P-V-T data of Kennedy (1954) for CO_2 was used to solve for the fugacity of CO_2 according to the equation

$$\ln P - \ln f = \frac{1}{RT} \int_0^P \alpha \, dP \qquad (33)$$

where $\alpha = RT/P - V$. Log f_{CO_2} values for temperatures exceeding 1000°C were estimated by the extrapolation of the available data.

These calculations were completed for each of the decarbonation reactions listed in Table 14 and the appropriate equilibrium curves are shown in Figures 2 to 11.

Also illustrated in Figures 2 to 11 are experimentally determined curves taken from the literature for direct comparison to the calculated curves (a complete experimental curve for reaction 1 was not available for comparison). Curves (7), (8) and (9) should correspond closely to the experimental curves of Zharikov and Shmulovich because the thermodynamic data for tilleyite, spurrite and rankinite was obtained from their experimental data. A comparison of Zharikov and Shmulovich's equilibrium curve for the reaction

$$2Ca_2SiO_4 \cdot CaCO_3 + Ca_3Si_2O_7 \rightleftharpoons 4\beta\text{-}Ca_2SiO_4 + CO_2 \qquad (10)$$

with the calculated equilibrium curve shows excellent agreement between them. This might indicate a discrepancy in Zharikov and Shmulovich's

TABLE 14

UNIVARIANT EQUILIBRIA IN THE SYSTEM $CaO-MgO-SiO_2-CO_2$

1) Diopside + 3 dolomite $\rightleftharpoons$ 2 forsterite + 4 calcite + 2 CO_2

$$CaMgSi_2O_6 + 3\ CaMg(CO_3)_2 \rightleftharpoons 2\ Mg_2SiO_4 + 4\ CaCO_3 + 2\ CO_2$$

2) Dolomite $\rightleftharpoons$ calcite + periclase + CO_2

$$CaMg(CO_3)_2 \rightleftharpoons CaCO_3 + MgO + CO_2$$

3) Calcite + B-quartz $\rightleftharpoons$ wollastonite + CO_2

$$CaCO_3 + B\text{-}SiO_2 \rightleftharpoons CaSiO_3 + CO_2$$

4) Diopside + forsterite + 2 calcite $\rightleftharpoons$ 3 monticellite + 2 CO_2

$$CaMgSi_2O_6 + Mg_2SiO_4 + 2\ CaCO_3 \rightleftharpoons 3\ CaMgSiO_4 + 2\ CO_2$$

5) Diopside + calcite $\rightleftharpoons$ akermanite + CO_2

$$CaMgSi_2O_6 + CaCO_3 \rightleftharpoons Ca_2MgSi_2O_7 + CO_2$$

6) 3 Calcite + 2 wollastonite $\rightleftharpoons$ spurrite + 2 CO_2

$$3\ CaCO_3 + 2\ CaSiO_3 \rightleftharpoons 2Ca_2SiO_4 \cdot CaCO_3 + 2\ CO_2$$

7) 3 Calcite + 2 wollastonite $\rightleftharpoons$ tilleyite + CO_2

$$3\ CaCO_3 + 2\ CaSiO_3 \rightleftharpoons Ca_5Si_2O_7(CO_3)_2 + CO_2$$

8) Tilleyite $\rightleftharpoons$ spurrite + CO_2

$$Ca_5Si_2O_7(CO_3)_2 \rightleftharpoons 2Ca_2SiO_4 \cdot CaCO_3 + CO_2$$

9) Tilleyite + 4 wollastonite $\rightleftharpoons$ 3 rankinite + 2 CO_2

$$Ca_5Si_2O_7(CO_3)_2 + 4\ CaSiO_3 \rightleftharpoons 3\ Ca_3Si_2O_7 + 2\ CO_2$$

10) Spurrite + rankinite $\rightleftharpoons$ 4 B-larnite + CO_2

$$2Ca_2SiO_4 \cdot CaCO_3 + Ca_3Si_2O_7 \rightleftharpoons 4\ B\text{-}Ca_2SiO_4 + CO_2$$

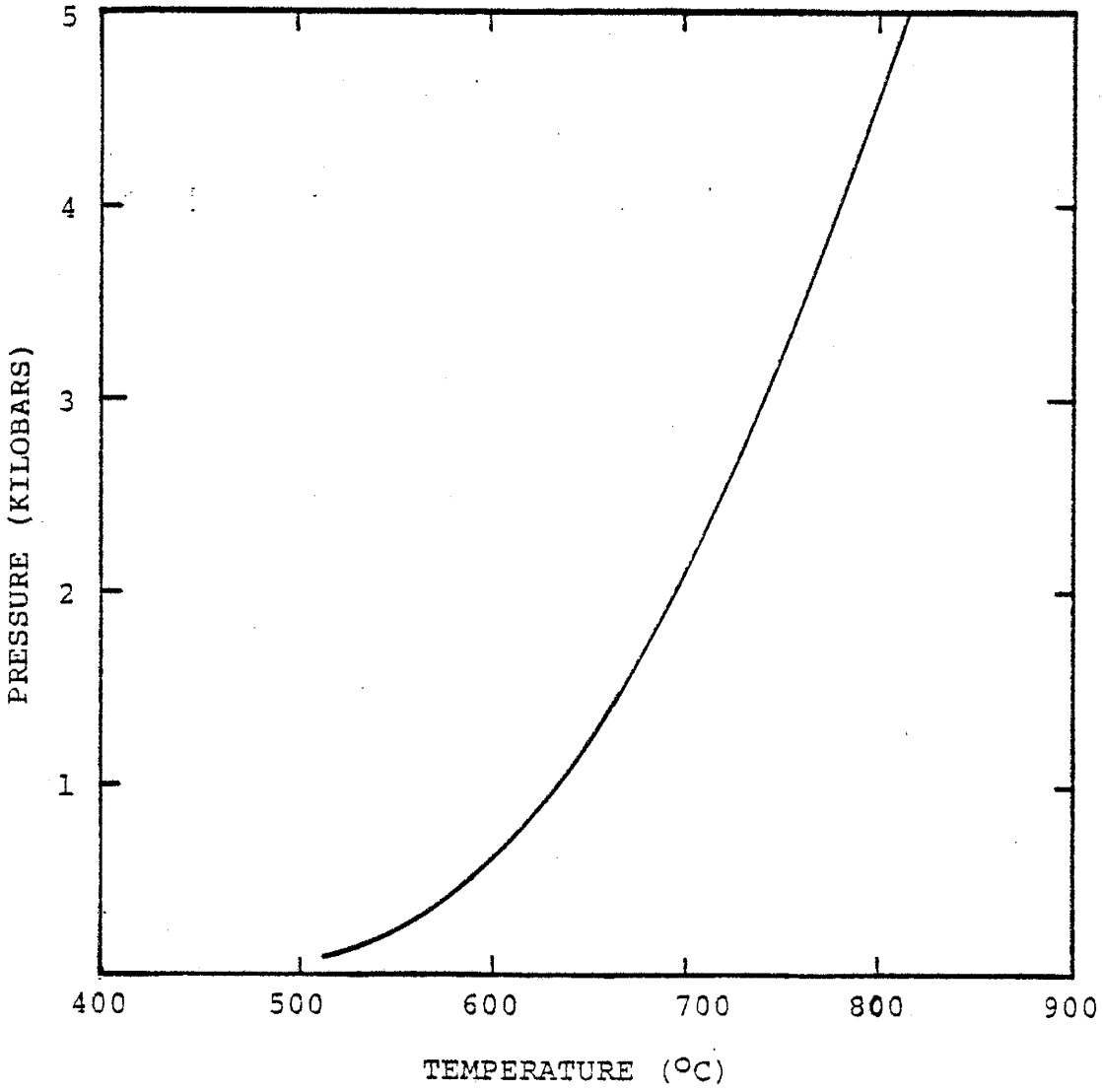

Figure 2. Calculated pressure-temperature equilibrium curve for the reaction $CaMgSi_2O_6$ (diopside) + $3CaMg(CO_3)_2$ (dolomite) $\rightleftharpoons$ $2Mg_2SiO_4$ (forsterite) + $4CaCO_3$ (calcite) + $2CO_2$ (gas).

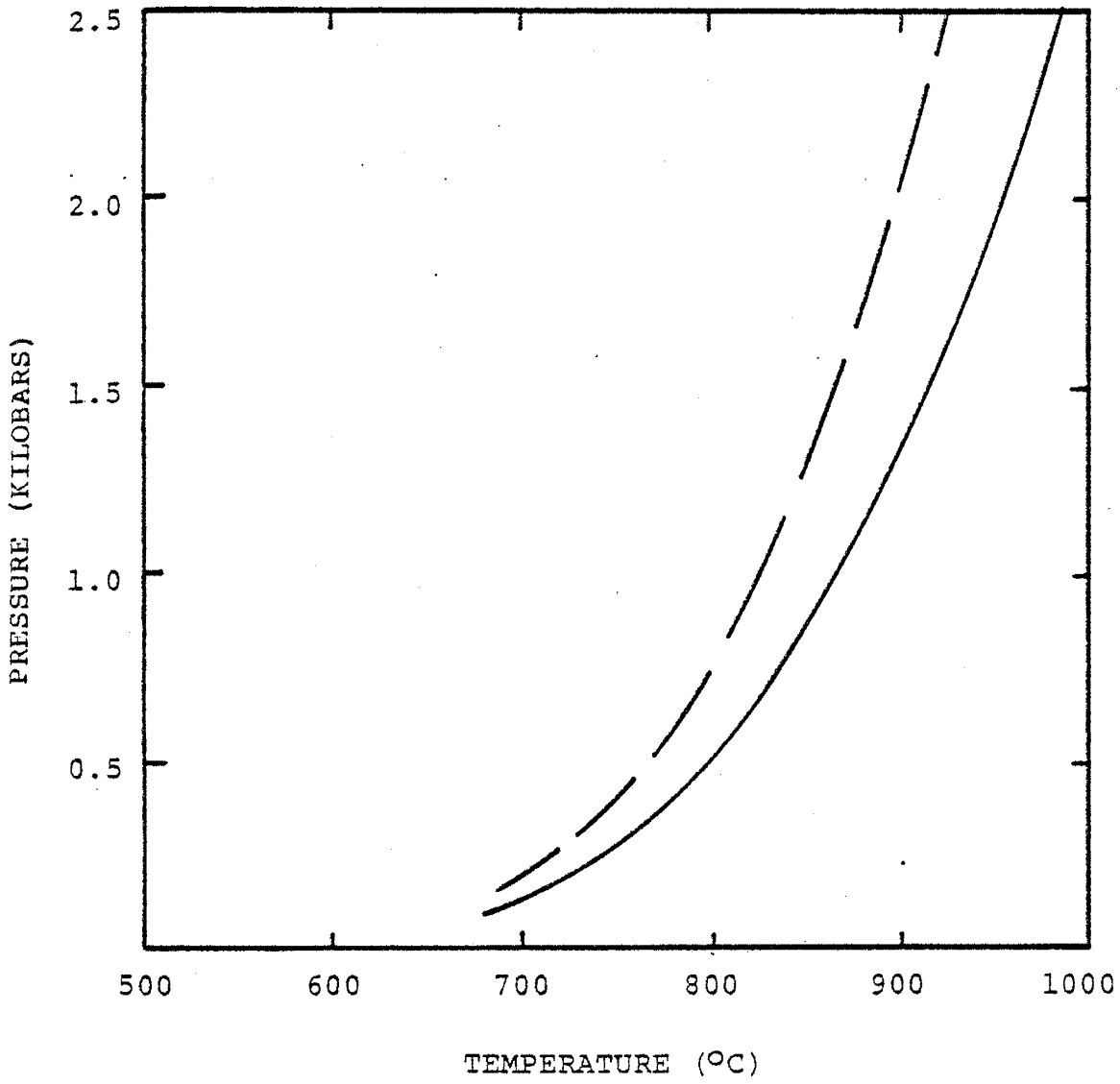

Figure 3. Pressure-temperature equilibrium curves for the reaction $CaMg(CO_3)_{2\ (dolomite)} \rightleftharpoons CaCO_{3\ (calcite)} + MgO_{\ (periclase)} + CO_{2\ (gas)}$. The solid line represents the calculated equilibrium curve and the dashed line represents the experimentally determined equilibrium curve of Harker and Tuttle (1955).

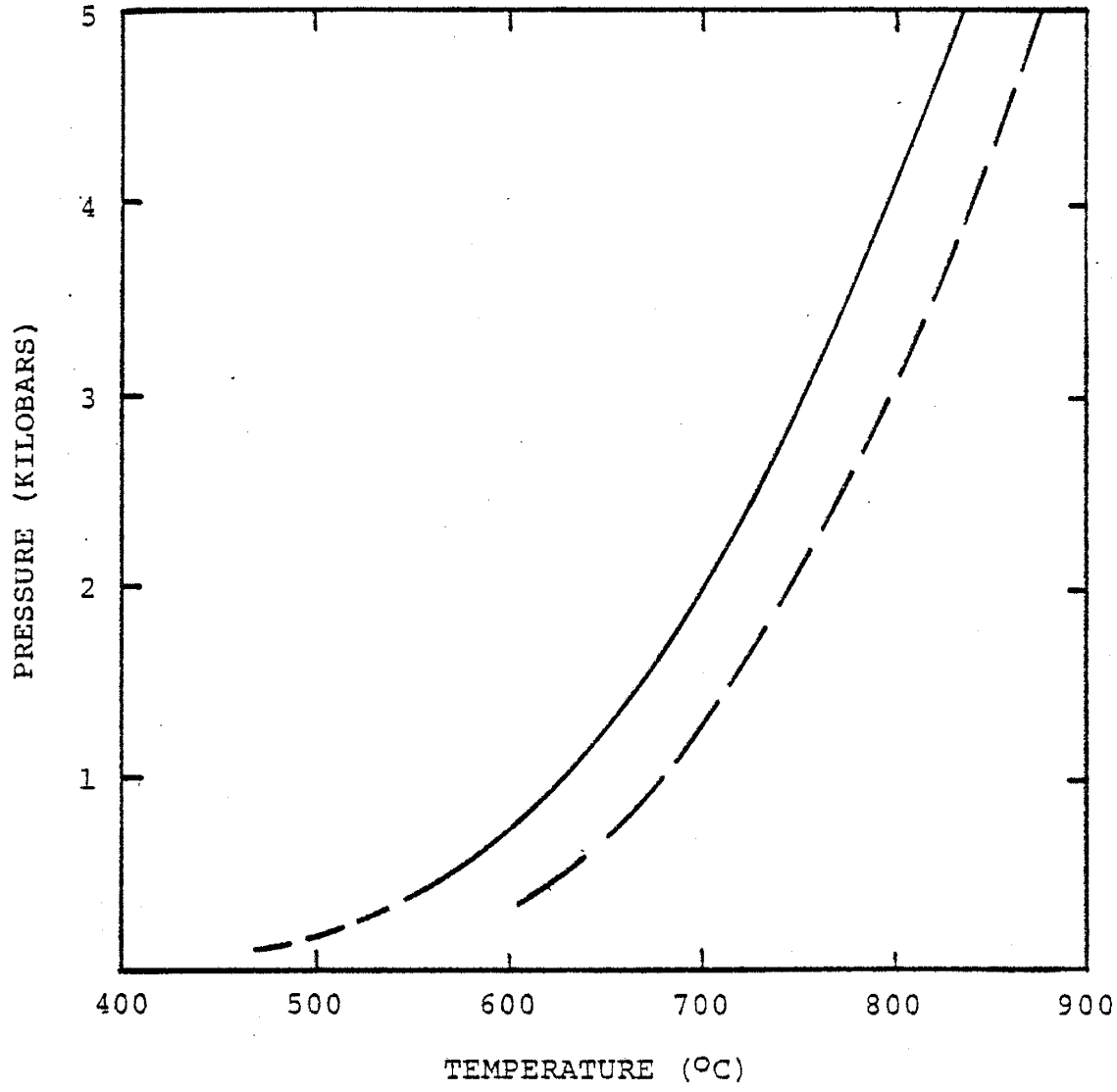

Figure 4. Pressure-temperature equilibrium curves for the reaction $CaCO_3$ (calcite) + β-SiO_2 (β-quartz) ⇌ $CaSiO_3$ (wollastonite) + CO_2 (gas). The solid line represents the calculated equilibrium curve and the dashed line represents the experimentally determined equilibrium curve of Harker and Tuttle (1956).

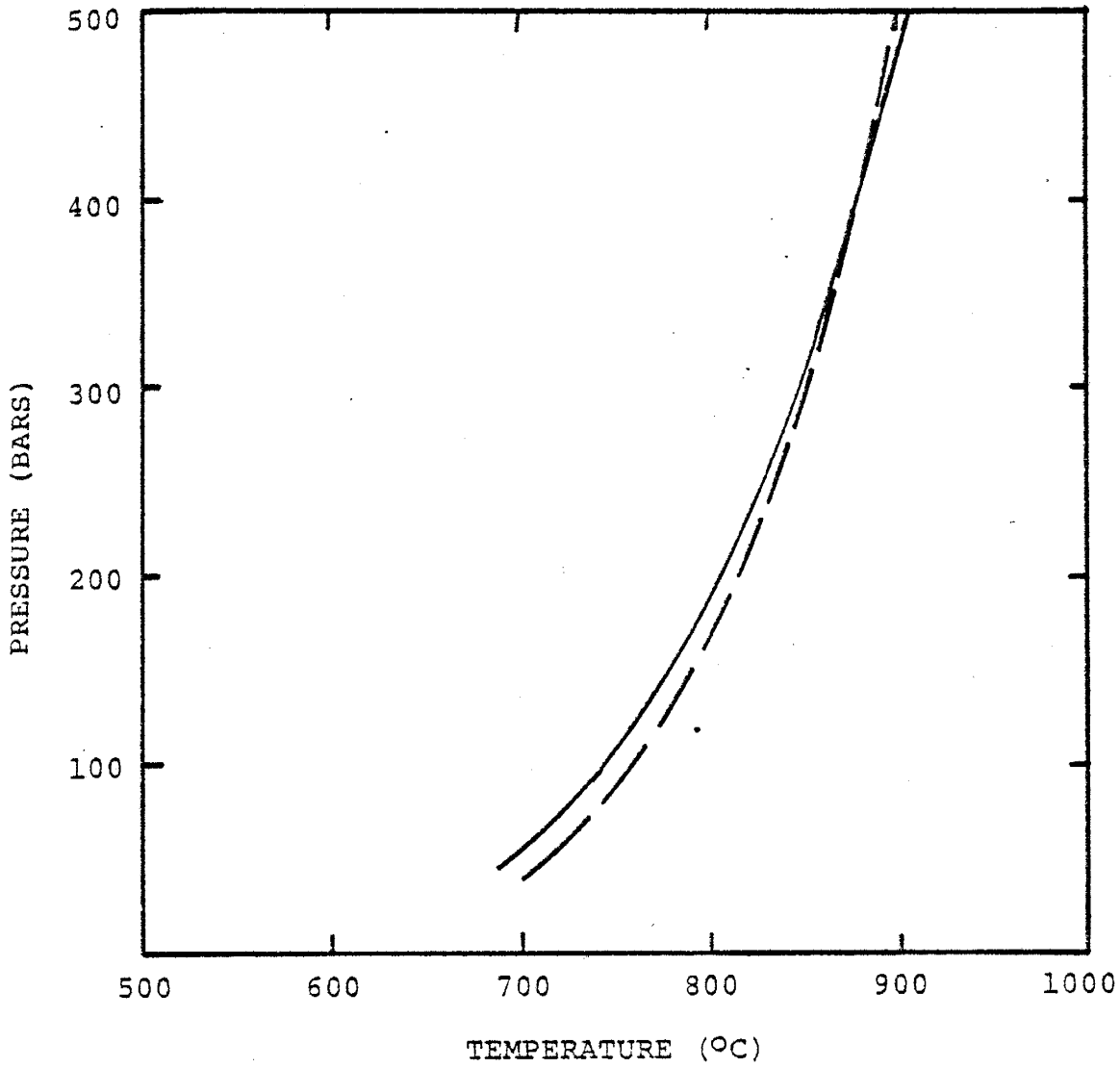

Figure 5. Pressure-temperature equilibrium curves for the reaction $CaMgSi_2O_6$ (diopside) + Mg_2SiO_4 (forsterite) + $2CaCO_3$ (calcite) $\rightleftharpoons$ $3CaMgSiO_4$ (monticellite) + $2CO_2$ (gas). The solid line represents the calculated equilibrium curve and the dashed line represents the experimentally determined equilibrium curve of Walter (1963a).

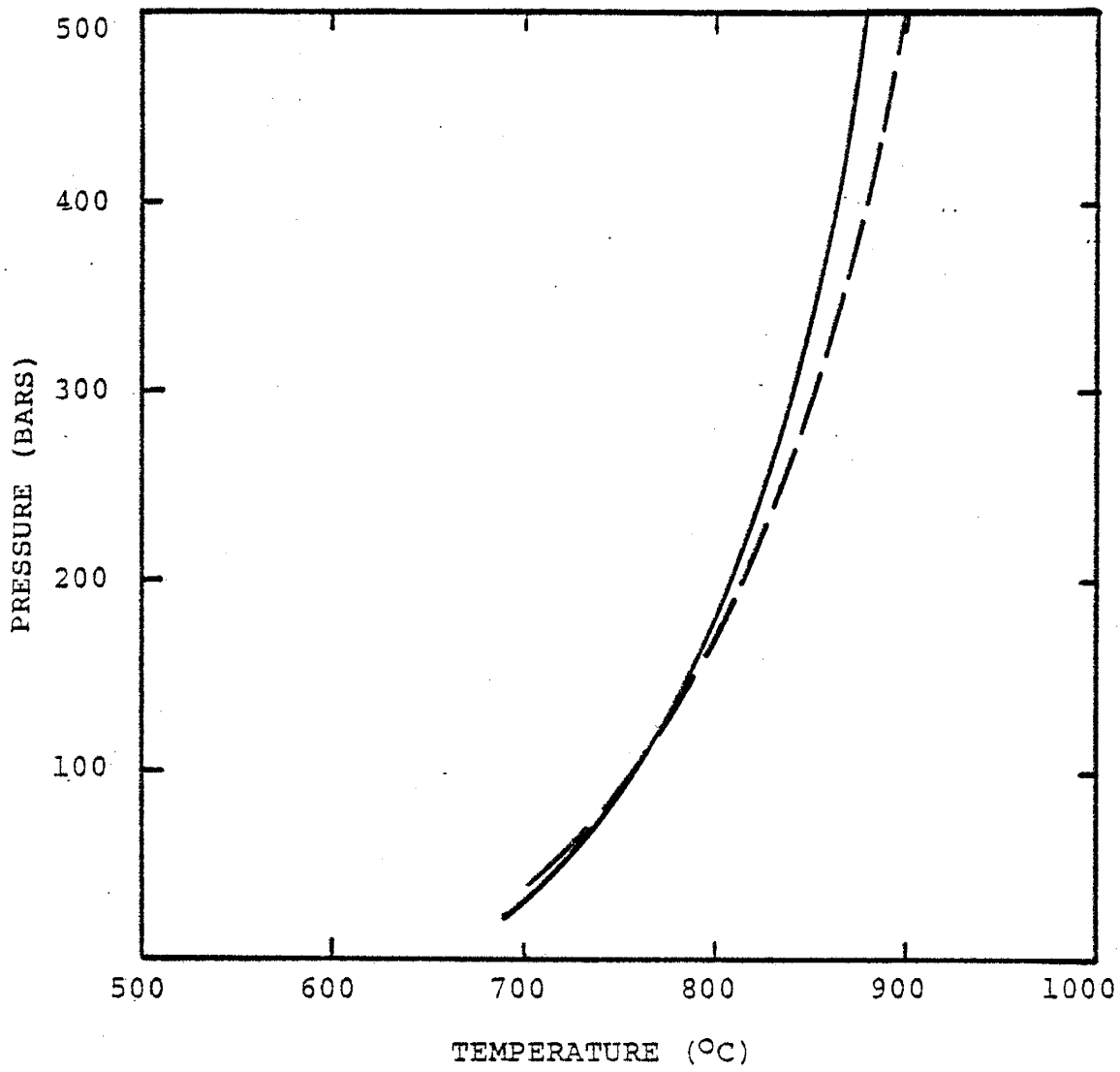

Figure 6. Pressure-temperature equilibrium curves for the reaction $CaMgSi_2O_6$ (diopside) + $CaCO_3$ (calcite) $\rightleftharpoons$ $Ca_2MgSi_2O_7$ (akermanite) + CO_2 (gas). The solid line represents the calculated equilibrium curve and the dashed line represents the experimentally determined equilibrium curve of Walter (1963a).

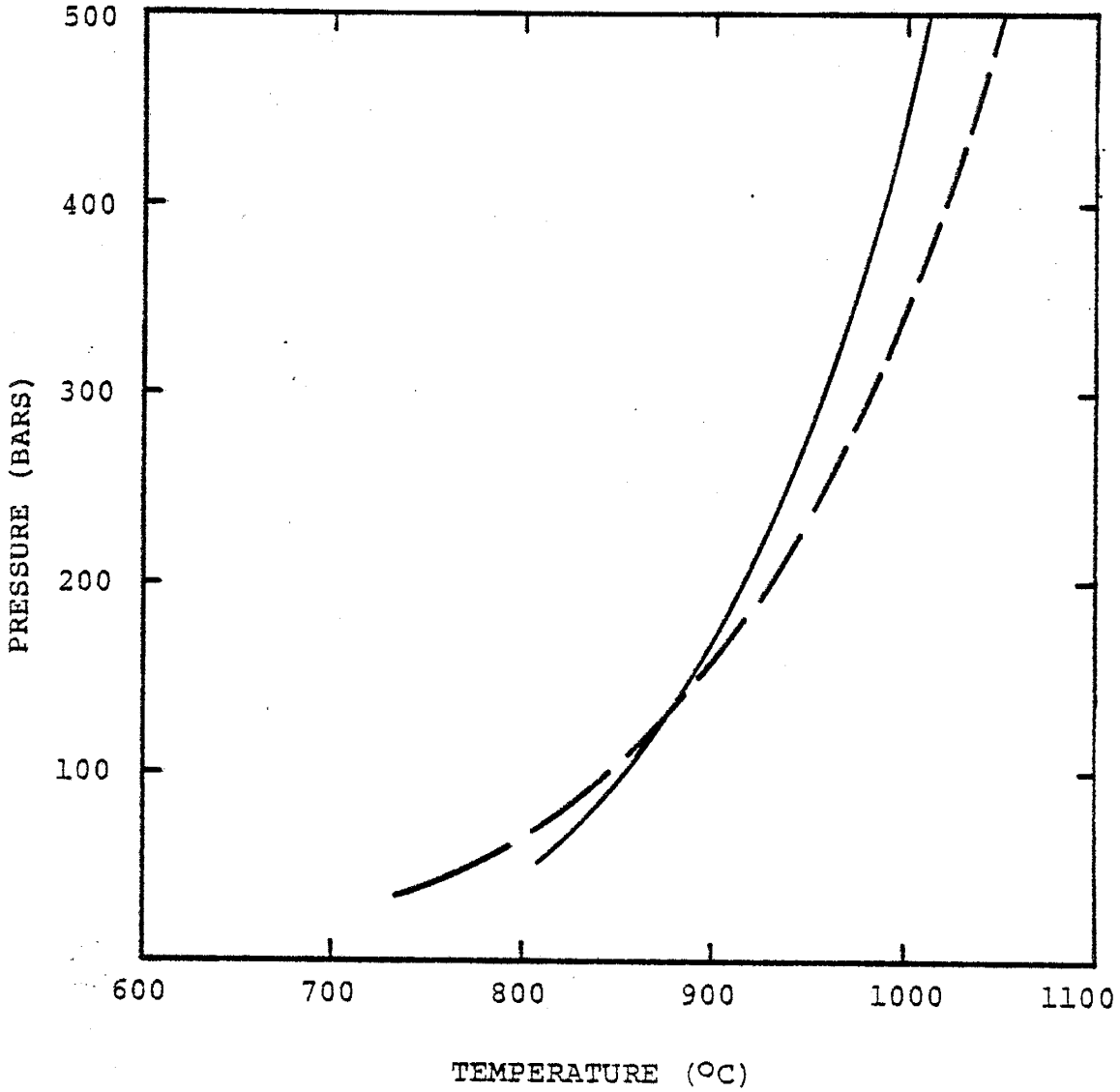

Figure 7. Pressure-temperature equilibrium curves for the reaction $3CaCO_3$ (calcite) + $2CaSiO_3$ (wollastonite) $\rightleftharpoons$ $2Ca_2SiO_4 \cdot CaCO_3$ (spurrite) + $2CO_2$ (gas). The solid line represents the calculated equilibrium curve and the dashed line represents the experimentally determined equilibrium curve of Zharikov and Shmulovich (1970).

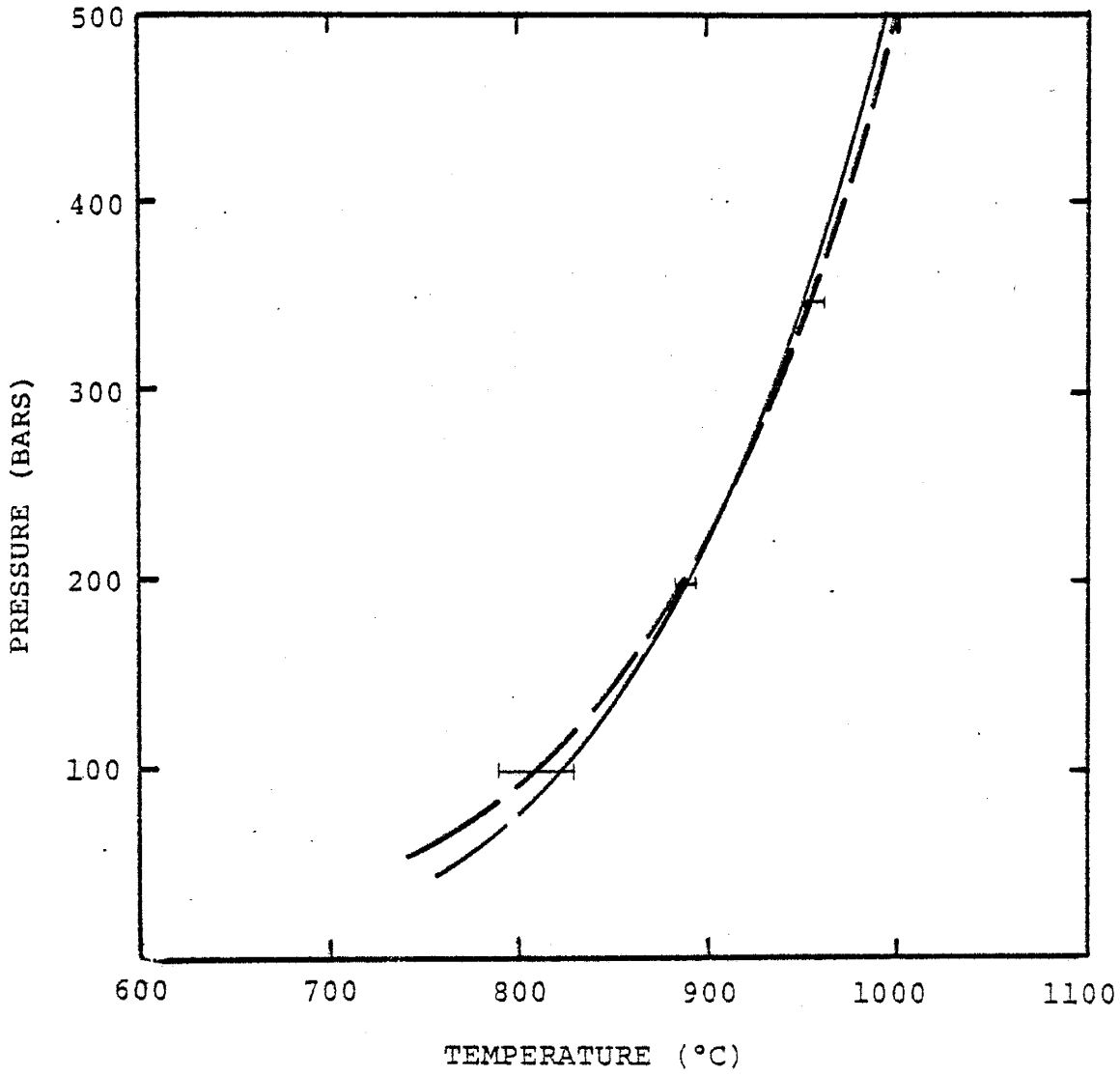

Figure 8. Pressure-temperature equilibrium curves for the reaction $3CaCO_{3\ (calcite)} + 2CaSiO_{3\ (wollastonite)} \rightleftharpoons Ca_5Si_2O_7(CO_3)_{2\ (tilleyite)} + CO_{2\ (gas)}$. The solid line represents the calculated equilibrium curve and the dashed line represents the experimentally determined equilibrium curve of Zharikov and Shmulovich (1970).

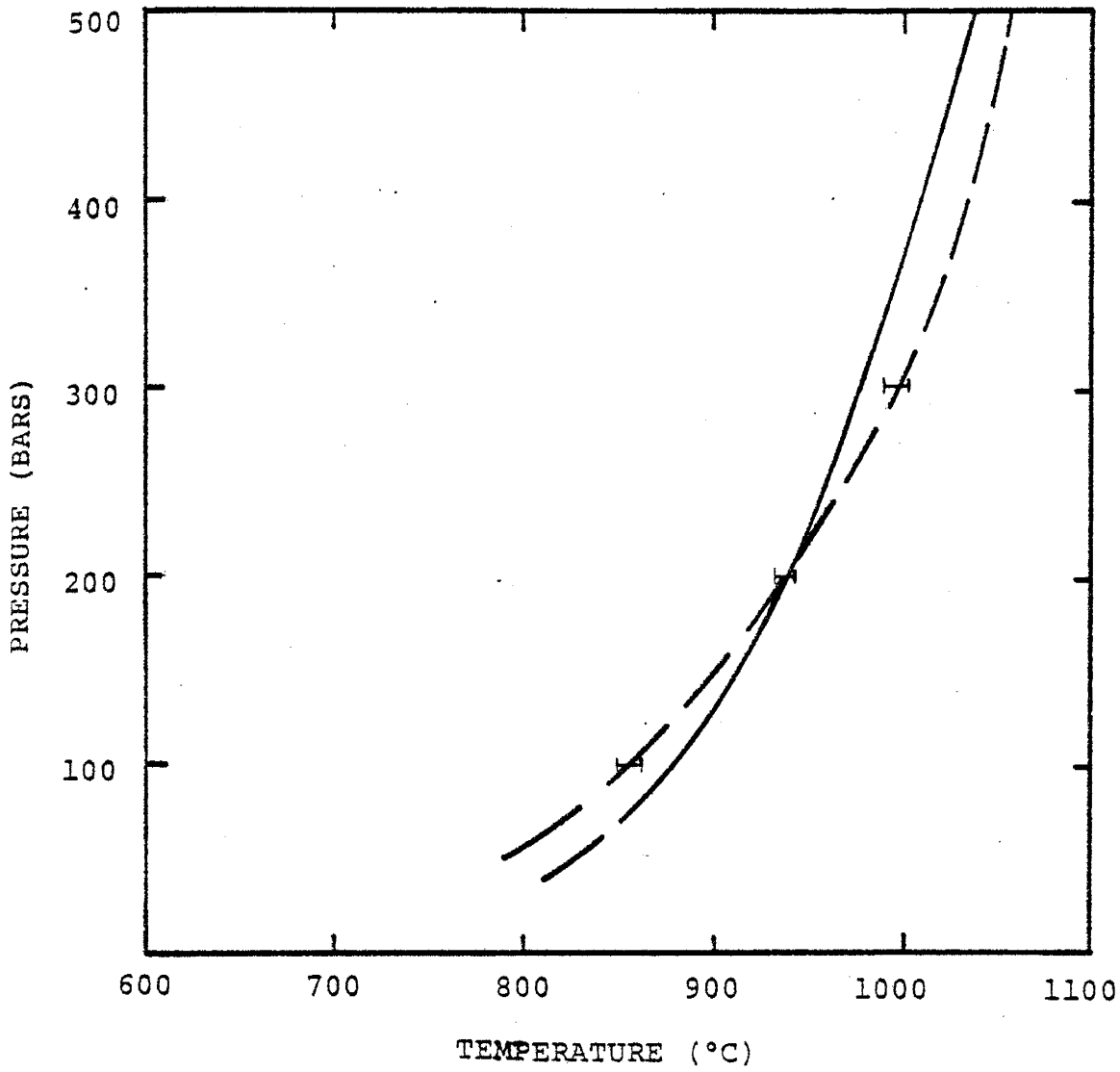

Figure 9. Pressure-temperature equilibrium curves for the reaction $Ca_5Si_2O_7(CO_3)_2$ (tilleyite) $\rightleftharpoons$ $2Ca_2SiO_4 \cdot CaCO_3$ (spurrite) + CO_2 (gas). The solid line represents the calculated equilibrium curve and the dashed line represents the experimentally determined equilibrium curve of Zharikov and Shmulovich (1970).

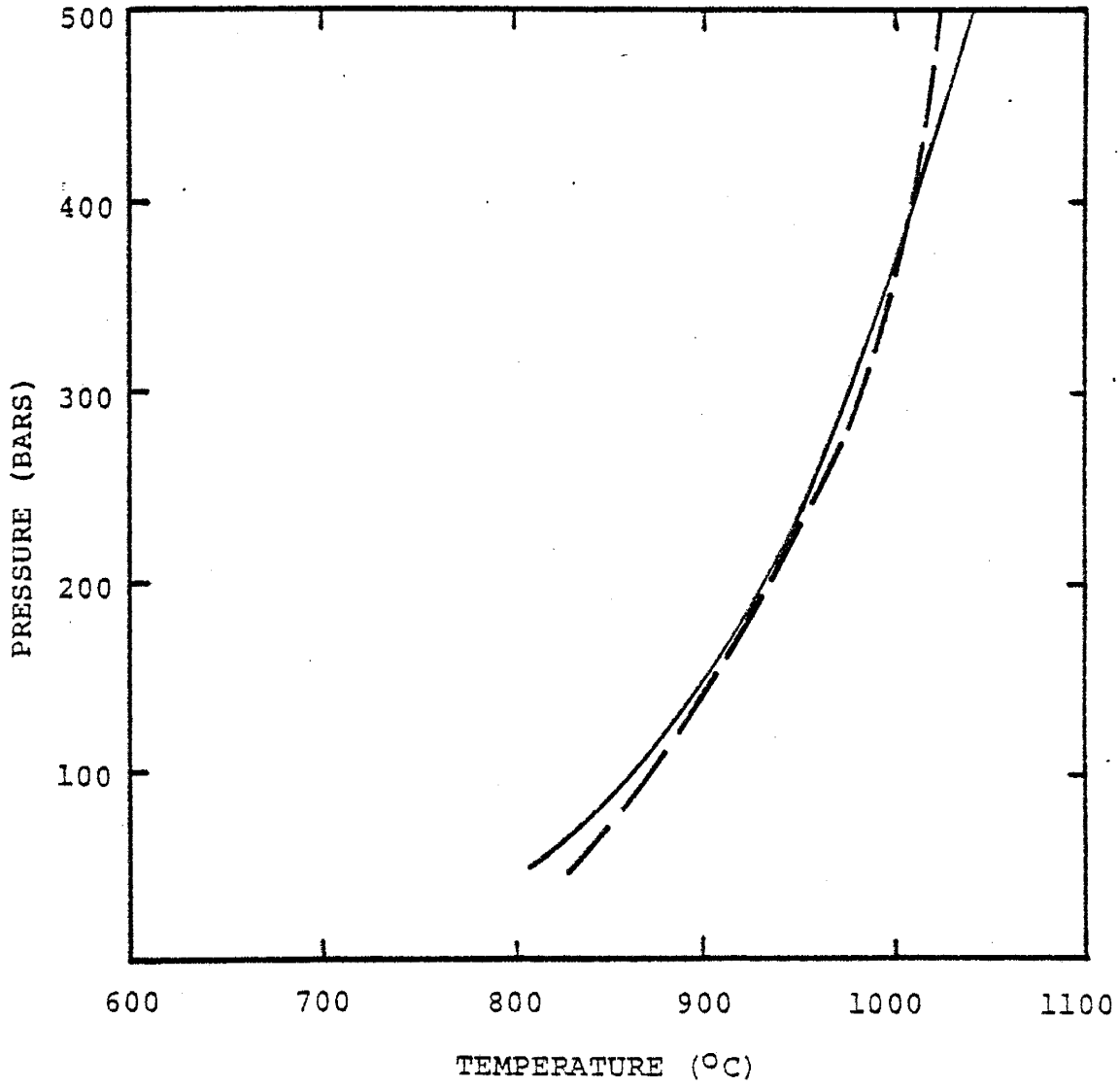

Figure 10. Pressure-temperature equilibrium curves for the reaction $Ca_5Si_2O_7(CO_3)_2$ (tilleyite) + $4CaSiO_3$ (wollastonite) $\rightleftharpoons$ $3Ca_3Si_2O_7$ (rankinite) + $2CO_2$ (gas). The solid line represents the calculated equilibrium curve and the dashed line represents the experimentally determined equilibrium curve of Zharikov and Shmulovich (1970).

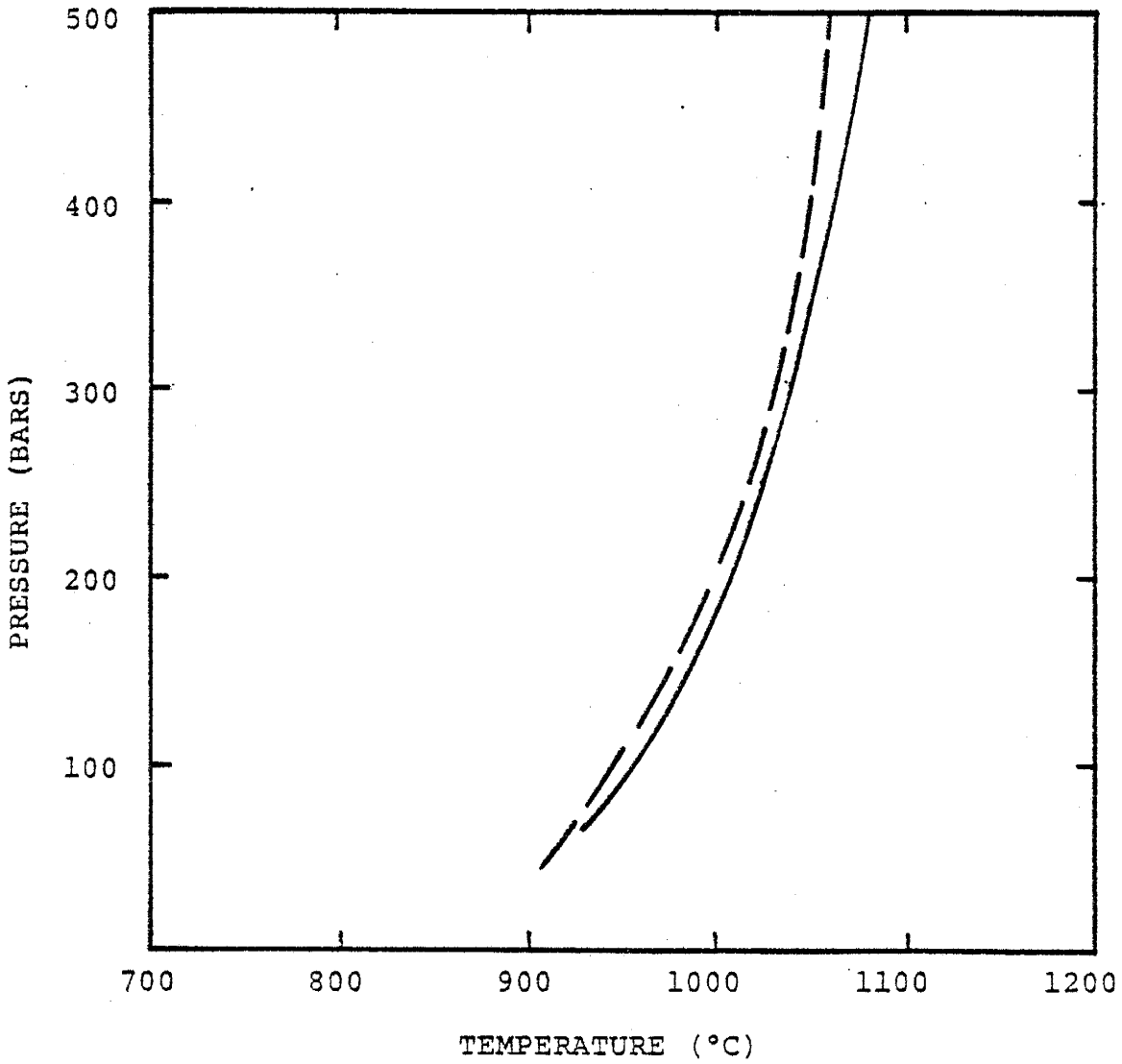

Figure 11. Pressure-temperature equilibrium curves for the reaction $2Ca_2SiO_4 \cdot CaCO_3$ (spurrite) + $Ca_3Si_2O_7$ (rankinite) $\rightleftharpoons$ $4\beta\text{-}Ca_2SiO_4$ (β-larnite) + CO_2 (gas). The solid line represents the calculated equilibrium curve and the dashed line represents the experimentally determined equilibrium curve of Zharikov and Shmulovich (1970).

experimental results that was first noticed in the calculation of the thermodynamic data for spurrite. Even though the estimated thermodynamic data for tilleyite reproduced the experimental curves to a high degree of accuracy, the spurrite data yielded a curve noticeably steeper than that of Zharikov and Shmulovich for the tilleyite-spurrite transition because the estimated entropy of spurrite could not be used to generate a consistent value of the enthalpy at Zharikov and Shmulovich's equilibrium points. However, reaction (10) also contains spurrite and the calculated equilibrium curve coincides almost exactly with the curve of Zharikov and Shmulovich. This seems to indicate that the estimated data for spurrite was accurate after all and that the equilibrium curve of Zharikov and Shmulovich for reaction (8) was positioned incorrectly. This theory is supported by the fact that the agreement between the calculated and experimental curves for the reaction

$$3\ CaCO_3 + 2\ CaSiO_3 \rightleftharpoons 2Ca_2SiO_4 \cdot CaCO_3 + 2\ CO_2 \qquad (6)$$

as determined by different experimentalists, Tuttle and Harker in 1957, is also quite good with the calculated curve falling $20^{\circ}C$ or less below the experimental one.

The calculated equilibrium curves for the reactions

$$CaMgSi_2O_6 + Mg_2SiO_4 + 2\ CaCO_3 \rightleftharpoons 3\ CaMgSiO_4 + 2\ CO_2 \qquad (4)$$

and

$$CaMgSi_2O_6 + CaCO_3 \rightleftharpoons Ca_2MgSi_2O_7 + CO_2 \qquad (5)$$

match the experimental curves of Walter (1963a,b) quite closely but the calculated curve of equilibrium for the reaction

$$CaCO_3 + \beta\text{-}SiO_2 \rightleftharpoons CaSiO_3 + CO_2 \qquad (3)$$

lies at a constant $50^{\circ}C$ below the experimental curve of Harker and Tuttle

(1956). The equilibrium curve calculated to represent the thermal dissociation of dolomite to calcite, periclase and CO_2 also lies at higher temperatures than the experimental curve of Harker and Tuttle (1955), with the deviation ranging from + 20°C at 100 bars to + 70°C at 3000 bars. This might be a result of the fact that the thermodynamic data used in this paper for dolomite is suspect although no revised values have been published for it as yet.

Temperature-X_{CO_2} Diagrams

The effect of an added variable in decarbonation reactions, that is, the mixing of H_2O and CO_2 in the fluid phase, will be illustrated by means of temperature-X_{CO_2} diagrams. Temperature-X_{CO_2} diagrams can be thought of as a bridge between the classical study of metamorphism from a purely physical point of view and the more recent study of metamorphism from a chemical point of view because the changing mole fraction of CO_2 can be equated with the changing chemical potential of CO_2 in the fluid phase.

Consider the hypothetical reaction

$$A + B \rightleftharpoons C + D + H_2O + CO_2 \quad . \tag{34}$$

According to the choice of standard states in this paper,

$$\log K_{r,T,P} = \log \left(\frac{a_C\, a_D\, a_{H_2O}\, a_{CO_2}}{a_A\, a_B} \right) = \log \left(a_{H_2O} \cdot a_{CO_2} \right). \tag{35}$$

Because we are now dealing with mixtures of gases, consideration must be given to the ideality, or non-ideality, of their mixing. Greenwood (1967) states that according to his experiments, CO_2 and H_2O appear to mix ideally below 2 kbar and above 500°C—that is, each gas in the CO_2-H_2O mixture is characterized by the same thermodynamic properties that it had as a pure gas-and its properties are therefore independent of the composition

of the mixture. This assumption of ideal mixing is expressed by the Lewis-Randall fugacity rule

$$f_i = f_i^o N_i \qquad (36)$$

where f_i^o represents the fugacity of the pure gas i at some temperature and pressure, f_i is the fugacity of gas i in a mixture at the same temperature and pressure, and N_i is the mole fraction of gas i in the mixture. The reference fugacity is related to the total pressure by:

$$f_i^o = \gamma_i^o P_T \quad , \qquad (37)$$

and because

$$P_i = N_i P_T \quad , \qquad (38)$$

the fugacity in a mixture is, from equations (37) and (38),

$$\begin{aligned} f_i &= \gamma_i^o P_T N_i \\ &= \gamma_i^o P_i \end{aligned} \qquad (39)$$

where P_T is the total pressure, P_i is the partial pressure of gas i, and γ_i^o represents the fugacity coefficient of the pure gas i at some temperature and pressure. Equation (39) seems to be relatively accurate if the total pressure is low and if the mole fraction of the gas whose fugacity is to be determined is high (Ryzhenko and Malinin, 1971).

However, in this paper we will be dealing with conditions for which the Lewis-Randall fugacity rule is not applicable; namely, pressures up to 1000 bars, low mole fractions of CO_2 and H_2O and temperatures below 500°C at which CO_2 and H_2O appear to form non-ideal mixtures. Therefore, use must be made of fugacity or activity coefficients for CO_2 and H_2O which take into account their non-ideal mixing. Greenwood (1973) lists activity

coefficients for varying mole fractions of CO_2 in mixtures with H_2O between 450° and 800°C and from 0 to 500 bars, but owing to the limited range of his data, the fugacity coefficients for mixtures of CO_2 and H_2O were chosen from the work of Ryzhenko and Malinin (1971), who used P-V-T-X data on CO_2 - H_2O mixtures in the equation

$$RT\ln \gamma_i = -\int_0^P (V_{id} - \bar{V}_i)\, dP \qquad (40)$$

where $\bar{V}_i$ represents the partial molar volume of gas i at T, P_T and N_i, and V_{id} is the ideal volume of gas i at the same T, P_T and N_i, in order to determine fugacity coefficients for each component in various mixtures within the ranges of 400° to 750°C and 400 to 2000 bars.

Equation (40) reveals that Ryzhenko and Malinin (1971) have chosen basically the same standard state for gases as was adopted in this paper - namely, the pure gas at 1 atm. and any specified temperature. Greenwood (1973), on the other hand, chose as his standard state the pure gas at any temperature and pressure, and was thus committed to determining activity coefficients for each gas in the mixture rather than fugacity coefficients as determined by Ryzhenko and Malinin. This is a result of the fact that when the standard state is a sliding one with respect to pressure, P_i^o and thus f_i^o are not necessarily equal to one because γ_i^o can be closely approximated by one only at high temperatures and low pressures ($\sim$ 1 atm). However, when the standard state of Ryzhenko and Malinin is chosen, P_i^o is equal to one atm. by definition. Consequently, f_i^o is approximately equal to one at high temperatures and low pressures and thus the activity of CO_2 or H_2O in a mixture can be approximated by its fugacity in the mixture; i.e.,

$$\frac{\gamma_i P_i}{\gamma_i^o P_i^o} = \frac{f_i}{f_i^o} = a_i \quad . \tag{41}$$

With the ability to determine the fugacities of CO_2 and H_2O at some temperature, pressure and X_{CO_2}, it is possible to evaluate log K_r in terms of the fugacities of the gases involved in the reaction at a series of temperatures at a constant total pressure and X_{CO_2} by comparing the computed curve with a similar plot of log K_r as calculated from equations (22) and (21) versus temperature. The intersection of the two curves yields a point along the equilibrium reaction curve at a specified temperature, total pressure and X_{CO_2}. Repetition of this process for varying X_{CO_2} at a series of pressures will ultimately provide an equilibrium curve for the reaction on a diagram having temperature and X_{CO_2} as variables at each of the total pressures considered.

This procedure can also be employed to calculate temperature-X_{CO_2} equilibrium curves for decarbonation reactions which do not explicitly involve H_2O, such as

$$CaMg(CO_3)_2 + 2\propto SiO_2 \rightleftharpoons CaMgSi_2O_6 + 2\ CO_2 \quad . \tag{17}$$

Even though the fugacity of H_2O is not involved in the calculation of log $K_{r,T,P}$, its presence will have a definite effect upon the fugacity of CO_2, and the fugacity coefficient of CO_2 utilized in calculating log $K_{r,T,P}$ must be the appropriate one for the conditions of temperature, total pressure and X_{CO_2}.

Skippen (1971,1974) made an extensive experimental investigation into the system CaO-MgO-SiO_2-H_2O-CO_2 and constructed temperature-X_{CO_2}

topologies at total pressures of 500, 1000, 2000 and 3000 bars. Slaughter, Kerrick and Wall (1975) utilized both experimental data and thermochemical calculations to construct some of the same equilibrium curves at 1000, 2000 and 5000 bars total pressure. Metz and Trommsdorf (1968) have also published detailed temperature-X_{CO_2} topologies but their equilibrium curves tend to lie at significantly higher temperatures than those of Skippen or Slaughter et al. Because the temperature-X_{CO_2} topologies calculated in this paper tended to agree with those of Skippen and Slaughter et al., the equilibrium curves of Metz were considered no further in this paper except to suggest that they are quite anomalous when compared to other experimental data.

Because Ryzhenko and Malinin's fugacity coefficients for the CO_2 - H_2O system terminate at less than 2000 bars in the temperature range 400° to 650°C, only 500 and 1000 bar total pressure temperature-X_{CO_2} diagrams could be constructed for the bivariant reactions listed in Table 15. They are illustrated in Figures 12 to 21 along with the corresponding topologies of Skippen and Slaughter et al. for purposes of comparison.

The equilibrium curves for the reactions

$$Ca_2Mg_5Si_8O_{22}(OH)_2 + 3\ CaCO_3 + 2\alpha SiO_2 \rightleftharpoons 5\ CaMgSi_2O_6 + 3\ CO_2 + 3\ H_2O \qquad (15)$$

and

$$3\ Ca_2Mg_5Si_8O_{22}(OH)_2 + 5\ CaCO_3 \rightleftharpoons 11\ CaMgSi_2O_6 + 2\ Mg_2SiO_4 + 5\ CO_2 + 3H_2O \qquad (16)$$

at 500 and 1000 bars total pressure match the equilibrium curves determined by Skippen at higher X_{CO_2} values but fall off slightly in accuracy at lower X_{CO_2}. Slaughter et al. determined an equilibrium curve for reaction

TABLE 15.

BIVARIANT REACTIONS IN THE SYSTEM $CaO-MgO-SiO_2-H_2O-CO_2$

11) 3 Dolomite + 4 α-quartz + H_2O ⇌ talc + 3 calcite + 3 CO_2

$3\ CaMg(CO_3)_2 + 4\alpha SiO_2 + H_2O \rightleftharpoons Mg_3Si_4O_{10}(OH)_2 + 3\ CaCO_3 + 3\ CO_2$

12) 2 Talc + 3 calcite ⇌ tremolite + dolomite + H_2O + CO_2

$2\ Mg_3Si_4O_{10}(OH)_2 + 3\ CaCO_3 \rightleftharpoons Ca_2Mg_5Si_8O_{22}(OH)_2 + H_2O + CO_2 + CaMg(CO_3)_2$

13) 5 Talc + 6 calcite + 4 α-quartz ⇌ 3 tremolite + 6 CO_2 + 2 H_2O

$5\ Mg_3Si_4O_{10}(OH)_2 + 6\ CaCO_3 + 4\alpha SiO_2 \rightleftharpoons 3\ Ca_2Mg_5Si_8O_{22}(OH)_2$

$+ 6\ CO_2 + 2\ H_2O$

14) 5 Dolomite + 8 α-quartz + H_2O ⇌ tremolite + 3 calcite + 7 CO_2

$5\ CaMg(CO_3)_2 + 8\alpha SiO_2 + H_2O \rightleftharpoons Ca_2Mg_5Si_8O_{22}(OH)_2 + 3\ CaCO_3 + 7\ CO_2$

15) Tremolite + 3 calcite + 2α quartz ⇌ 5 diopside + 3 CO_2 + H_2O

$Ca_2\ Mg_5Si_8O_{22}(OH)_2 + 3\ CaCO_3 + 2\ \alpha\ SiO_2 \rightleftharpoons 5\ CaMgSi_2O_6$

$+ 3\ CO_2 + H_2O$

16) 3 Tremolite + 5 calcite ⇌ 11 diopside + 2 forsterite + 5 CO_2 + 3 H_2O

$3\ Ca_2Mg_5Si_8O_{22}(OH)_2 + 5\ CaCO_3 \rightleftharpoons 11\ CaMgSi_2O_6 + 2\ Mg_2SiO_4$

$+ 5\ CO_2 + 3\ H_2O$

17) Dolomite + 2 α-quartz ⇌ diopside + 2 CO_2

$CaMg(CO_3)_2 + 2\alpha SiO_2 \rightleftharpoons CaMgSi_2O_6 + 2\ CO_2$

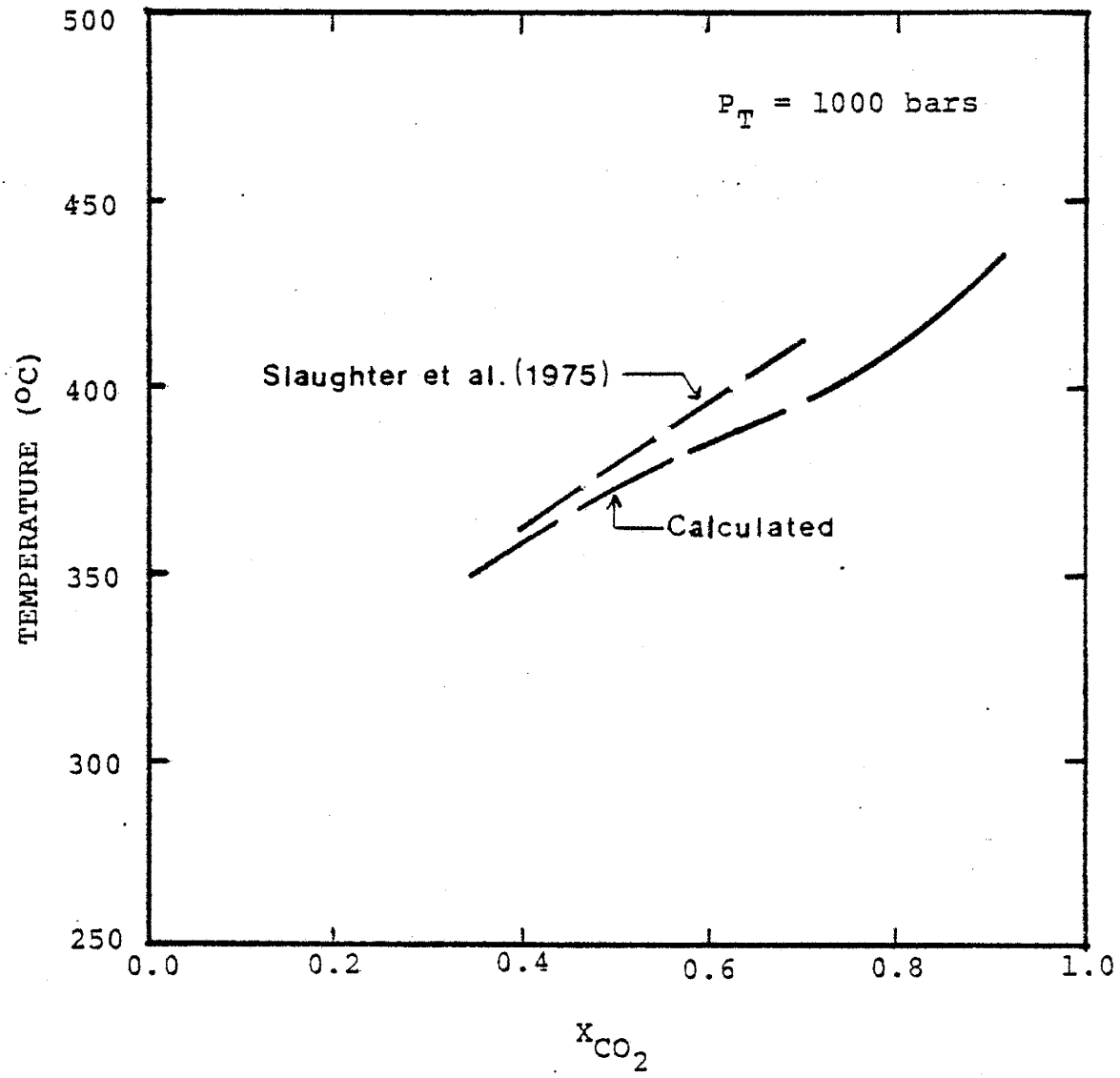

Figure 12. Temperature-X_{CO_2} equilibrium curves for the reaction

$$3CaMg(CO_3)_{2\ (dolomite)} + 4\alpha SiO_{2\ (\alpha\text{-quartz})} + H_2O_{(gas)} \rightleftharpoons Mg_3Si_4O_{10}(OH)_{2\ (talc)} + 3CaCO_{3\ (calcite)} + 3\ CO_{2\ (gas)} \quad (11)$$

at 1000 bars total pressure. The solid line represents the calculated equilibrium curve and the dashed line represents the equilibrium curve determined by Slaughter et al. (1975).

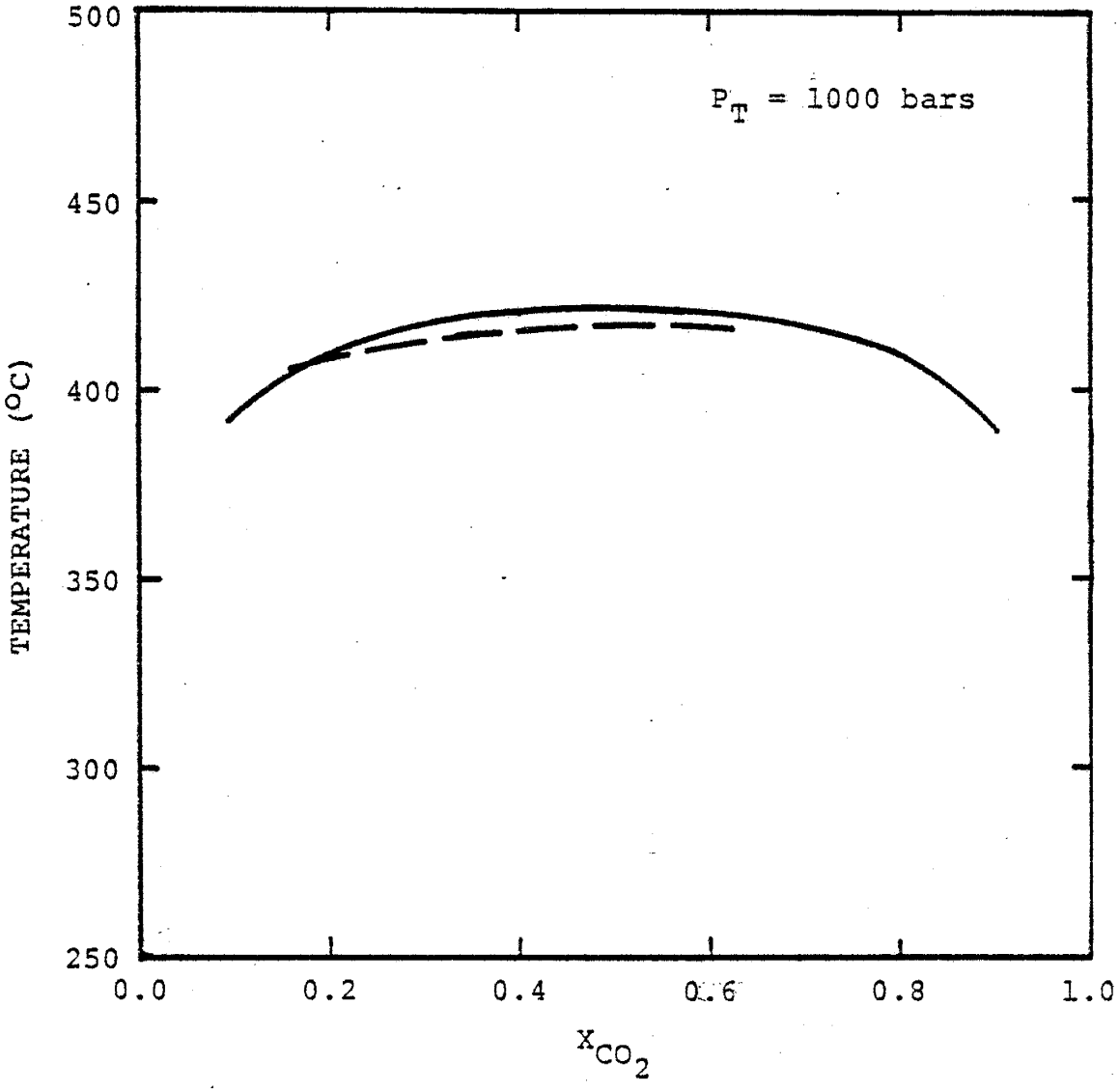

Figure 13. Temperature-X_{CO_2} equilibrium curves for the reaction $2Mg_3Si_4O_{10}(OH)_2$ (talc) + $3CaCO_3$ (calcite) $\rightleftharpoons$ $Ca_2Mg_5Si_8O_{22}(OH)_2$ (tremolite) + $CaMg(CO_3)_2$ (dolomite) + CO_2 (gas) + H_2O (gas) (12) at 1000 bars total pressure. The solid line represents the calculated equilibrium curve and the dashed line represents the equilibrium curve determined by Slaughter et al. (1975).

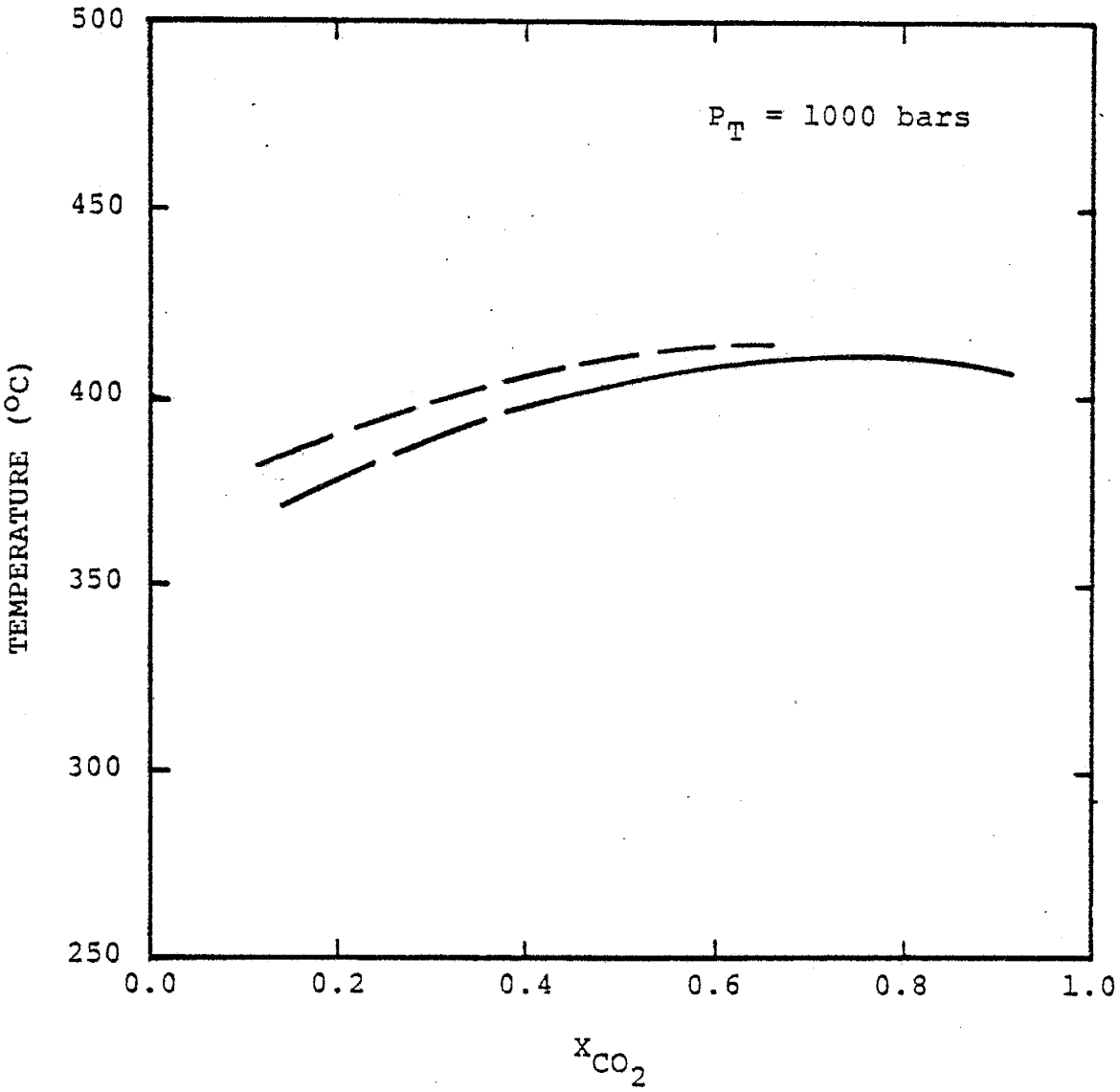

Figure 14. Temperature-X_{CO_2} equilibrium curves for the reaction

$5Mg_3Si_4O_{10}(OH)_2$ (talc) + $6CaCO_3$ (calcite) + 4α-SiO_2 (α-quartz)
$\rightleftharpoons$ $3Ca_2Mg_5Si_8O_{22}(OH)_2$ (tremolite) + $6CO_2$ (gas) + $2H_2O$ (gas)

(13) at 1000 bars total pressure. The solid line represents the calculated equilibrium curve and the dashed line represents the equilibrium curve determined by Slaughter et al. (1975).

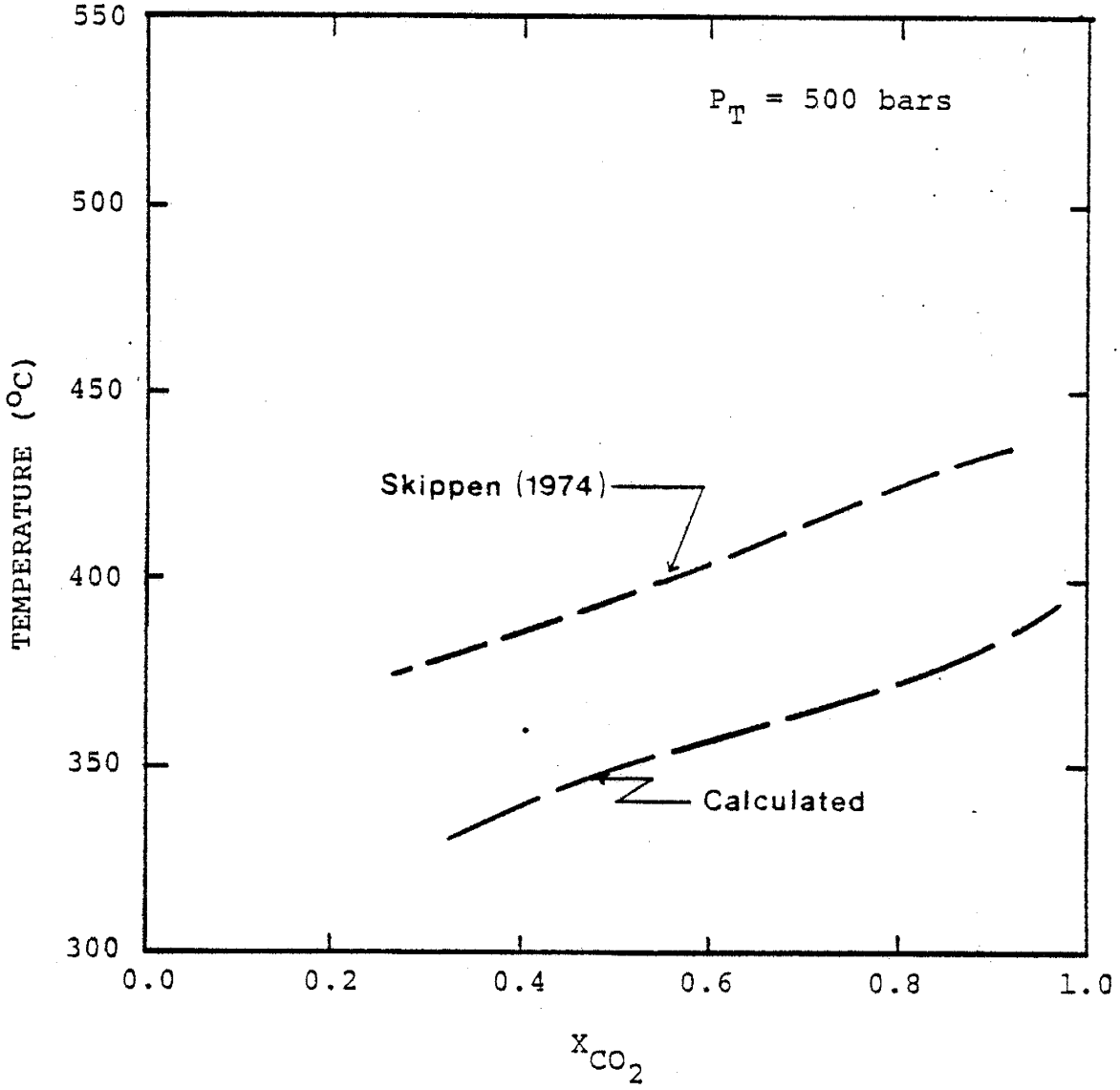

Figure 15. Temperature-X_{CO_2} equilibrium curves for the reaction $5CaMg(CO_3)_2$ (dolomite) + $8\alpha\text{-}SiO_2$ (α-quartz) + H_2O (gas) $\rightleftharpoons$ $Ca_2Mg_5Si_8O_{22}(OH)_2$ (tremolite) + $3CaCO_3$ (calcite) + $7CO_2$ (gas) (14) at 500 bars total pressure. The solid line represents the calculated equilibrium curve and the dashed line represents the experimentally determined equilibrium curve of Skippen (1974).

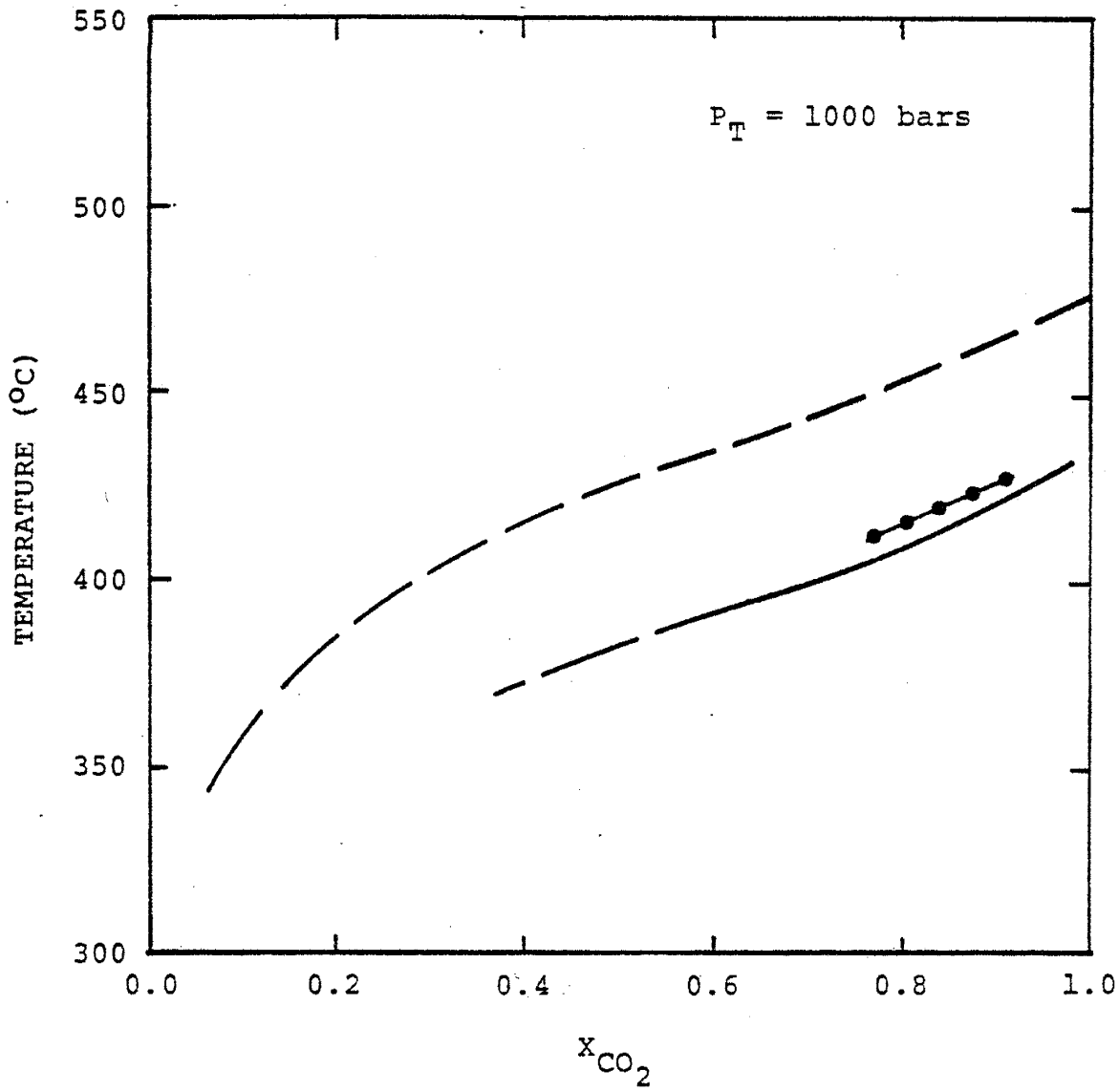

Figure 16. Temperature-X_{CO_2} equilibrium curves for the reaction $5CaMg(CO_3)_2$ (dolomite) + $8\alpha\text{-}SiO_2$ (α-quartz) + H_2O (gas) $\rightleftharpoons$ $Ca_2Mg_5Si_8O_{22}(OH)_2$ (tremolite) + $3CaCO_3$ (calcite) + $7CO_2$ (gas) (14) at 1000 bars total pressure. The solid line represents the calculated equilibrium curve, the dashed line represents the experimentally determined equilibrium curve of Skippen (1974) and the dotted line traces the equilibrium curve determined by Slaughter et al. (1975).

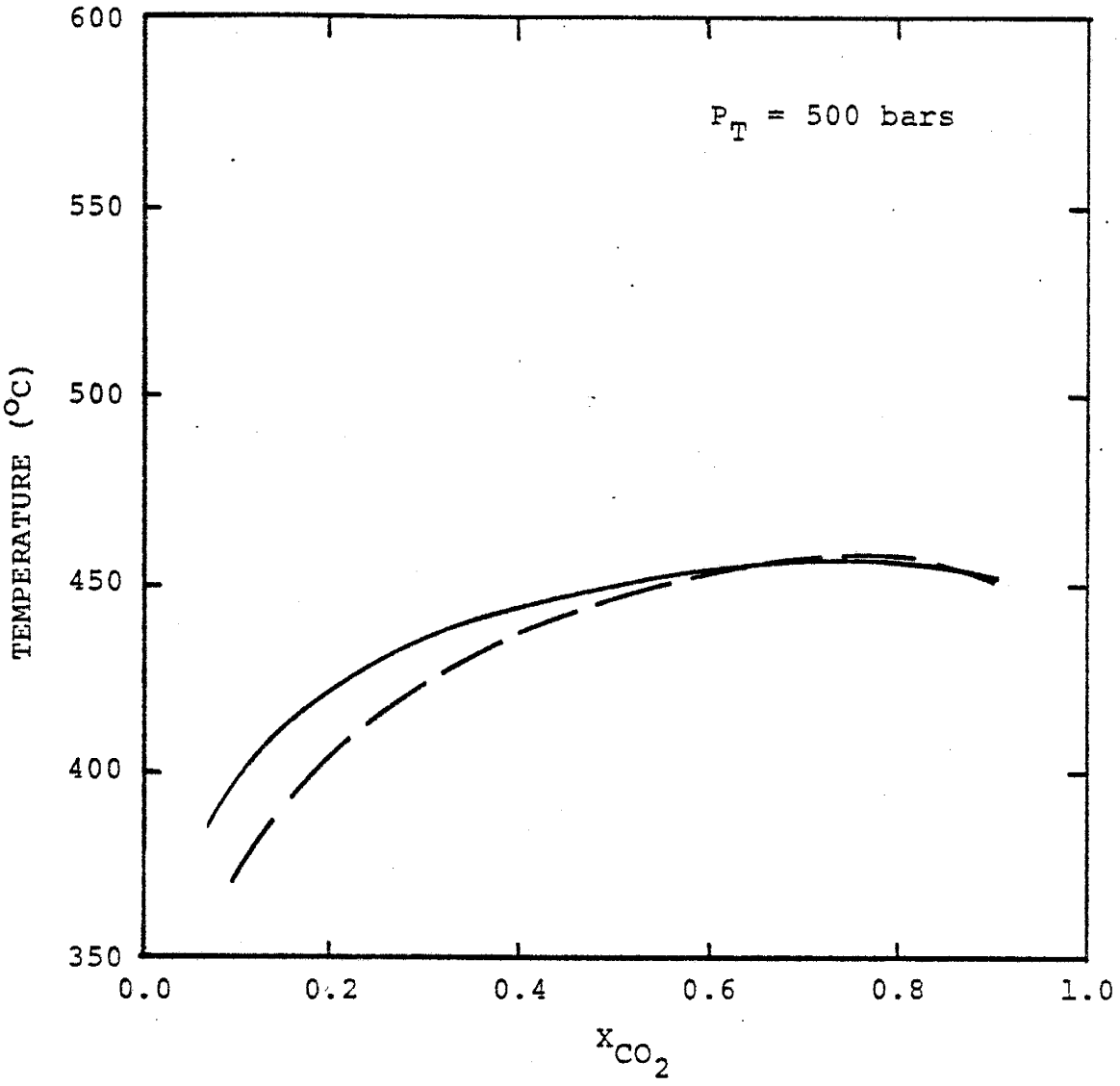

Figure 17. Temperature-X_{CO_2} equilibrium curves for the reaction $Ca_2Mg_5Si_8O_{22}(OH)_2$ (tremolite) + $3CaCO_3$ (calcite) + 2α-SiO_2 (α-quartz) $\rightleftharpoons$ $5CaMgSi_2O_6$ (diopside) + $3CO_2$ (gas) + H_2O (gas) (15) at 500 bars total pressure. The solid line represents the calculated equilibrium curve and the dashed line represents the experimentally determined equilibrium curve of Skippen (1974).

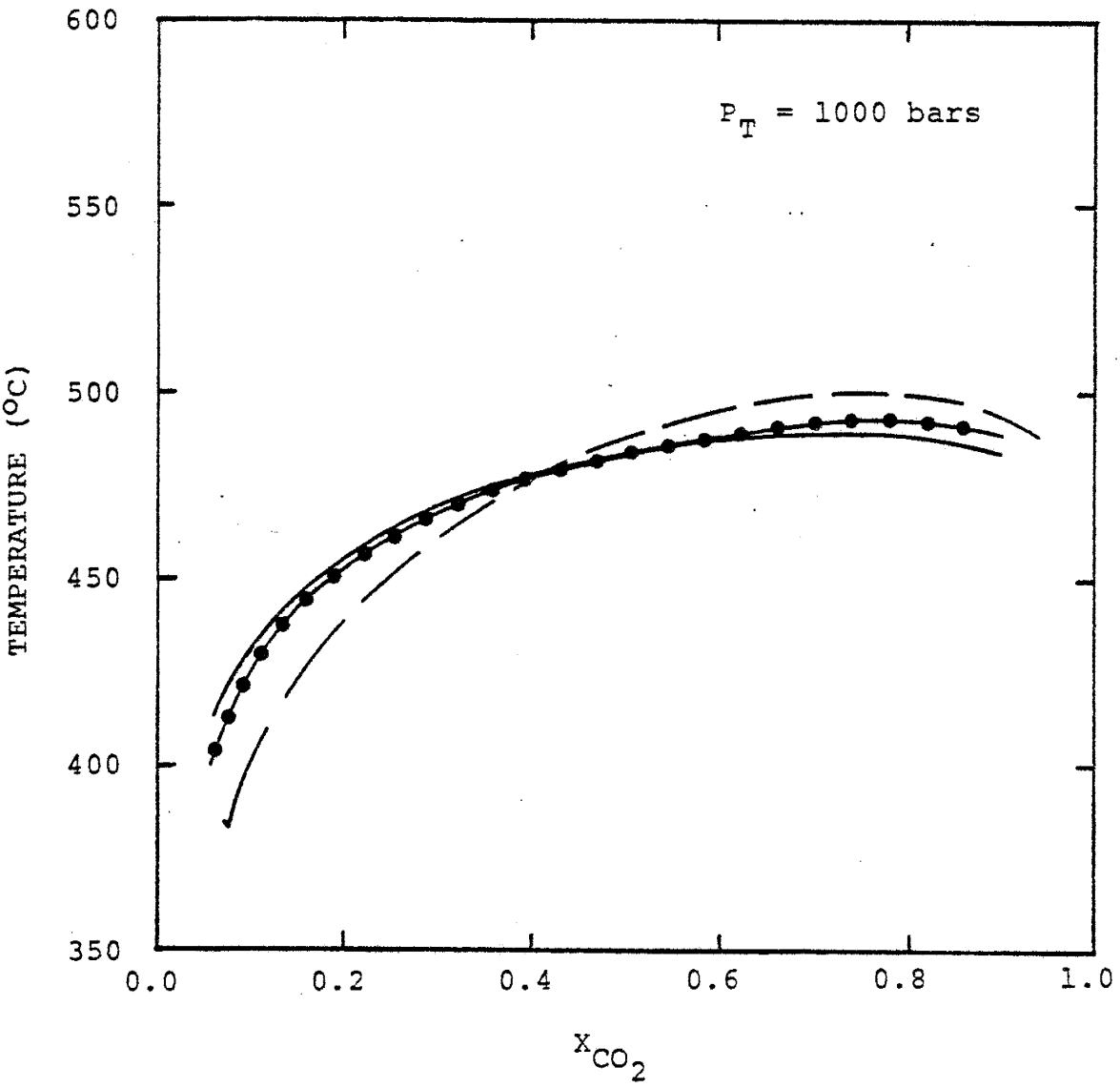

Figure 18. Temperature-X_{CO_2} equilibrium curves for the reaction $Ca_2Mg_5Si_8O_{22}(OH)_2$ (tremolite) + $3CaCO_3$ (calcite) + 2α-SiO_2 (α-quartz) $\rightleftharpoons$ $5CaMgSi_2O_6$ (diopside) + $3CO_2$(gas) + H_2O (gas) (15) at 1000 bars total pressure. The solid line represents the calculated equilibrium curve, the dashed line represents the experimentally determined equilibrium curve of Skippen (1974) and the dotted line traces the equilibrium curve determined by Slaughter et al. (1975).

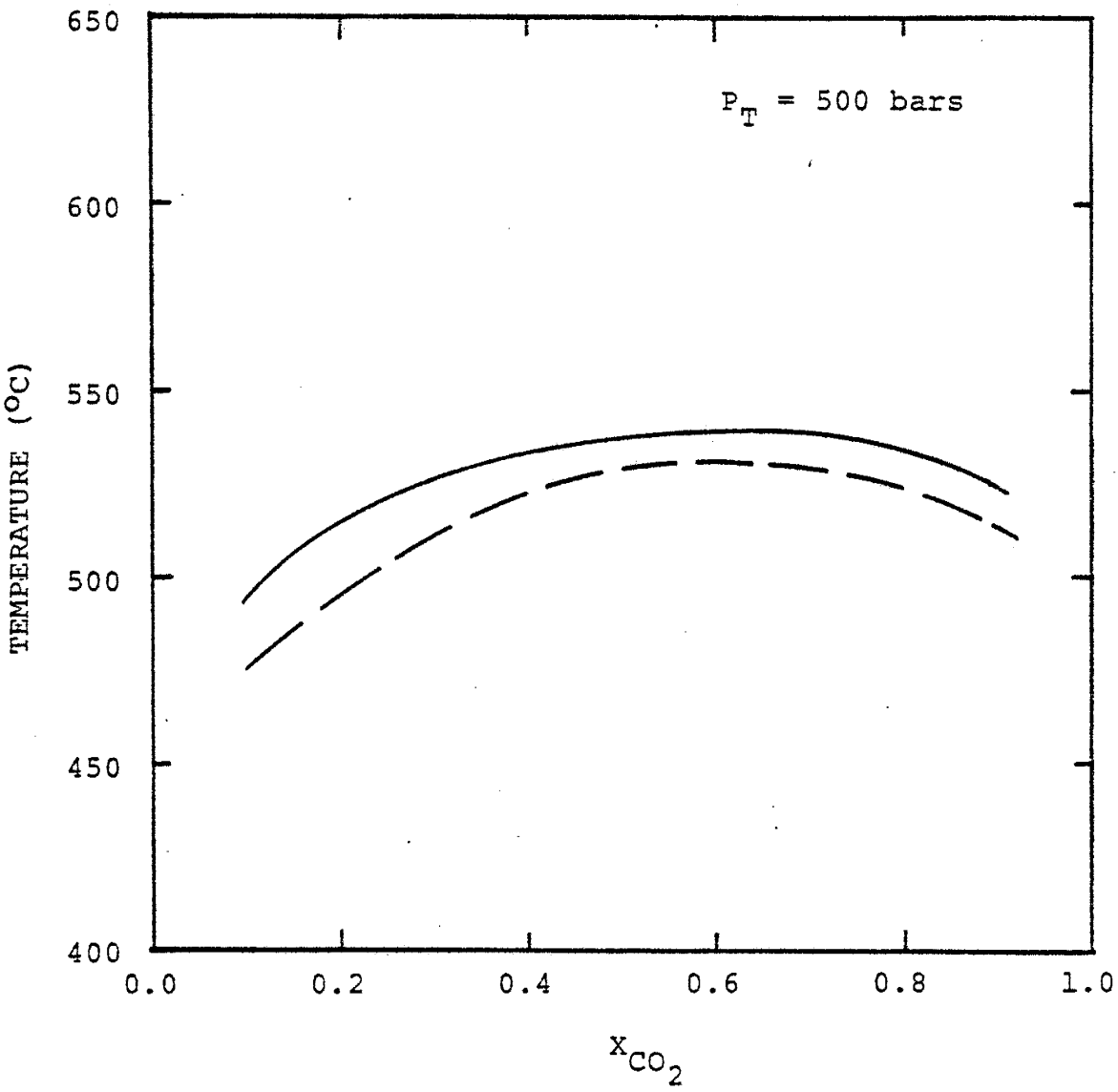

Figure 19. Temperature-X_{CO_2} equilibrium curves for the reaction $3Ca_2Mg_5Si_8O_{22}(OH)_2$ (tremolite) + $5CaCO_3$ (calcite) $\rightleftharpoons$ $5CO_2$ (gas) + 11 $CaMgSi_2O_6$ (diopside) + $2Mg_2SiO_4$ (forsterite) + $3H_2O$ (gas) (16) at 500 bars total pressure. The solid line represents the calculated equilibrium curve and the dashed line represents the experimentally determined equilibrium curve of Skippen (1974).

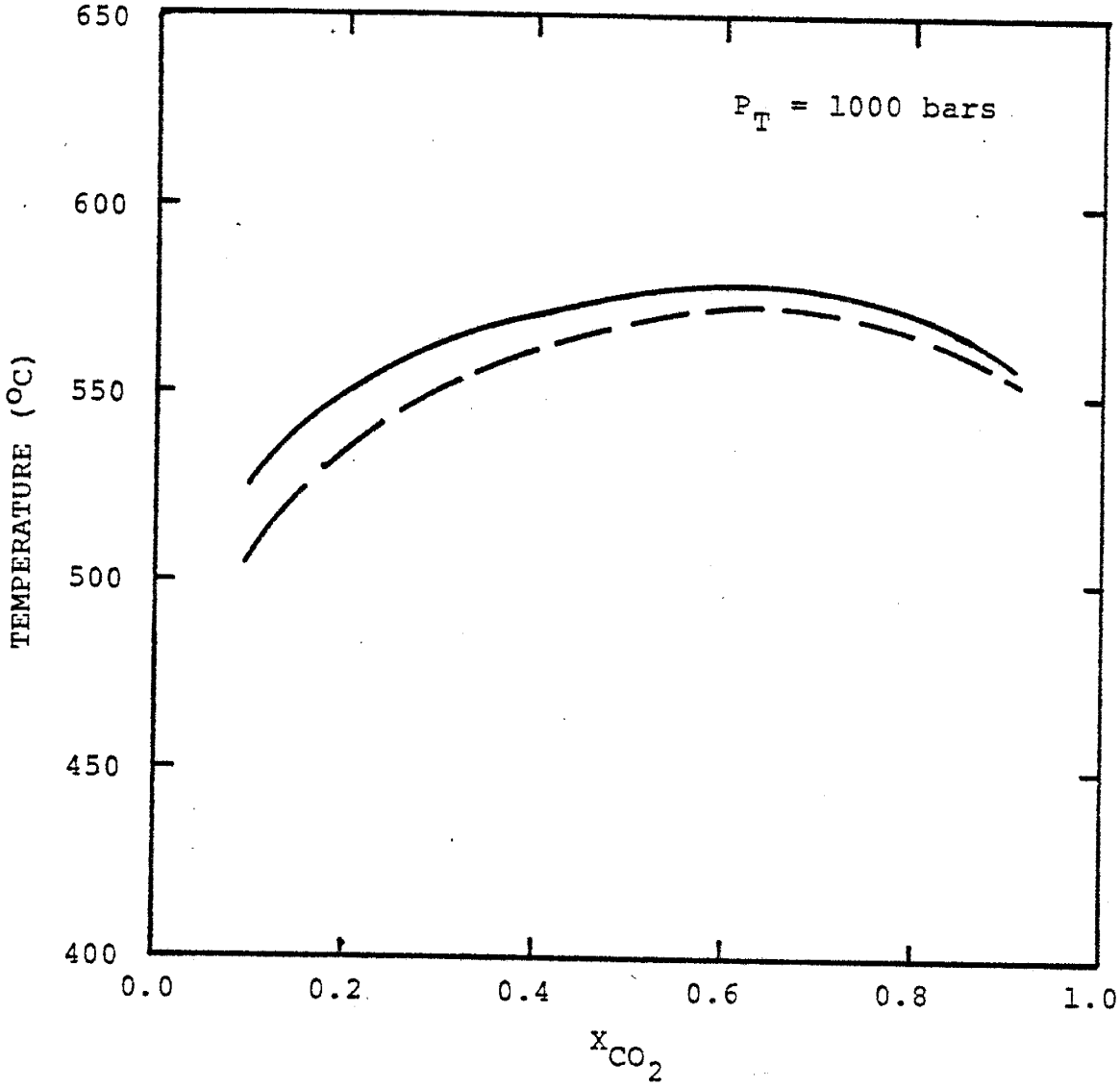

Figure 20. Temperature-X_{CO_2} equilibrium curve for the reaction $3Ca_2Mg_5Si_8O_{22}(OH)_2$ (tremolite) + $5CaCO_3$ (calcite) $\rightleftharpoons$ $11CaMgSi_2O_6$ (diopside) + $2Mg_2SiO_4$ (forsterite) + $5CO_2$ (gas) + $3H_2O$ (gas) (16) at 1000 bars total pressure. The solid line represents the calculated equilibrium curve and the dashed line represents the experimentally determined equilibrium curve of Skippen (1974).

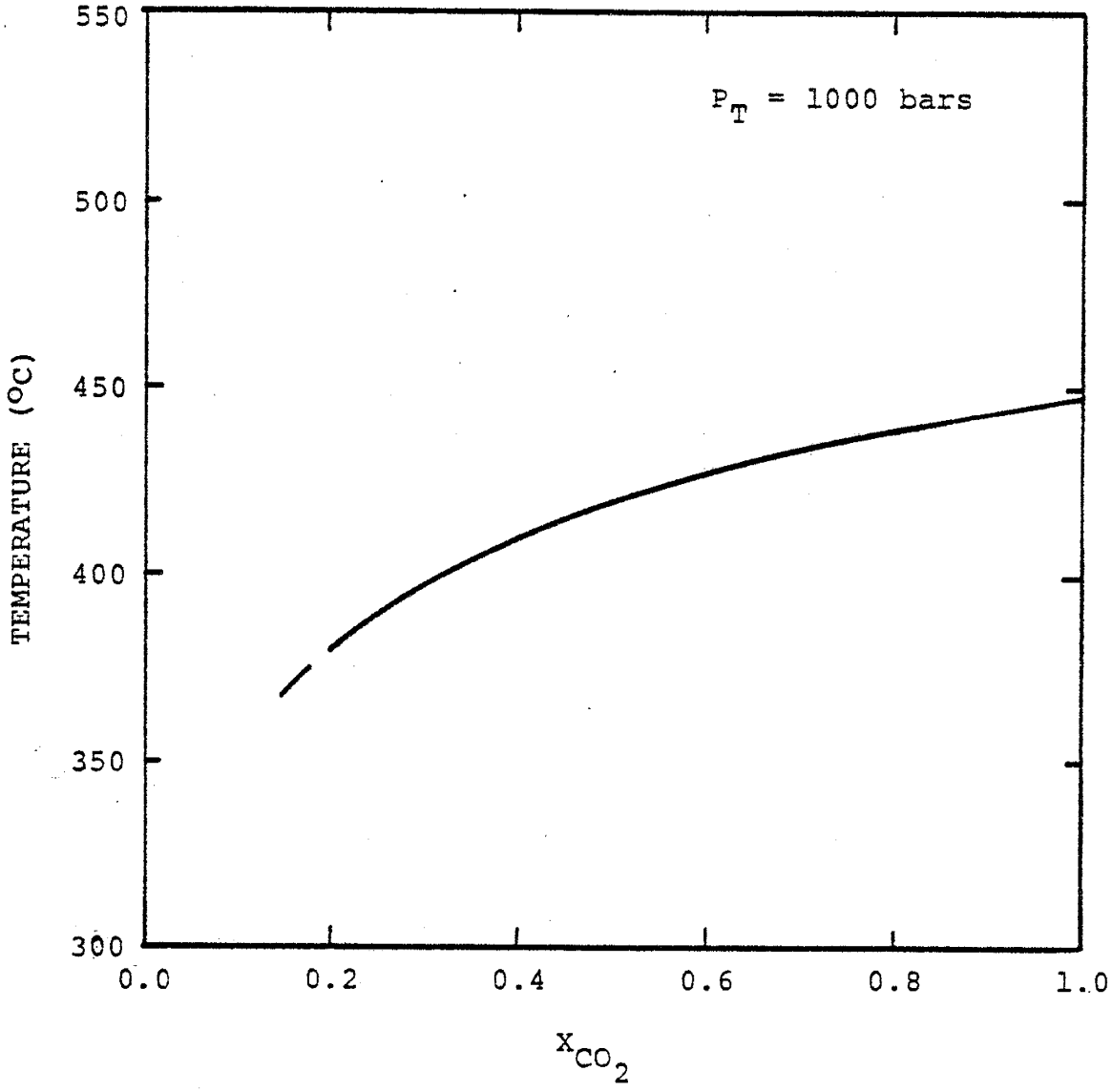

Figure 21. Calculated temperature-X_{CO_2} equilibrium curve for the reaction $CaMg(CO_3)_2$ (dolomite) + 2α-SiO_2 (α-quartz) $\rightleftharpoons$ $CaMgSi_2O_6$ (diopside) + $2CO_2$ (gas) (17) at 1000 bars total pressure.

(15) at 1000 bars total pressure and their combination of experimental and thermochemical data yielded curves almost identical to those calculated in this paper even at low X_{CO_2}. The equilibrium curve for reaction (14),

$$5\ CaMg(CO_3)_2 + 8\alpha SiO_2 + H_2O \rightleftharpoons Ca_2Mg_5Si_8O_{22}(OH)_2 + 3\ CaCO_3 + 7\ CO_2 \qquad (14)$$

corresponds with that of Slaughter et al. relatively well at 1000 bars total pressure but both the curves of Slaughter et al. and this paper fall about 40°C below the temperature-X_{CO_2} topology of Skippen. The deviation increases to about 50°C at 500 bars total pressure.

Constructing temperature-X_{CO_2} topologies for reactions involving talc presented a special problem. Bricker, Nesbitt and Gunter (1973) point out that, according to the Gibbs free energy of talc cited by Robie and Waldbaum (ΔG_f^o = -1324.386 ± 1.720 kcal/mole), surface sea water and interstitial pore fluids from marine bottom muds are supersaturated with respect to talc, which does not seem to be the case in nature.

Attempting to resolve this discrepancy, Bricker et al. estimated ΔG_f^o to be -1320 kcal/mole from three independent lines of evidence, a value which they felt was consistent with natural occurrences of talc. They also noted the difference between Robie and Waldbaum's tabulated $S^o_{298.15}$ of talc (62.34 cal/mole-deg) and the entropy predicted from the summation of the entropies of the pure oxides with a 0.6 volume correction as proposed by Fyfe et al. in 1958 (67.0 cal/mole-deg). Because the latter method usually predicts the entropy of a mineral to

within ± 5%, Bricker et al. decided to use 67.0 cal/mole-deg as the standard third law entropy of talc in their calculations. Unfortunately, they did not attempt to reproduce experimental equilibrium curves with their estimated entropy data to check its accuracy. Assuming $S^{o}_{298.15}$ = 67.0 cal/mole-deg and ΔG^{o}_{f} = -1320 kcal/mole, ΔH^{o}_{f} of talc is equal to -1409000 cal/mole.

Hemley (1975) proposed a Gibbs free energy of talc of -1320323 cal/mole which is quite similar to that suggested by Bricker et al. However, if $S^{o}_{298.15}$ of talc is assumed to be equal to 62.34 cal/mole-deg this time, ΔH^{o}_{f} = -1411041 cal/mole.

Other values of the thermodynamic properties of talc can be found in the literature but, in general, all seem to designate a ΔH^{o}_{f} of talc that is more positive than the value published by Robie and Waldbaum. When the revised data for talc, namely, ΔH^{o}_{f} = -1409000 cal/mole, $S^{o}_{298.15}$ = 67.0 cal/mole-deg and ΔH^{o}_{f} = -1411041 cal/mole, $S^{o}_{298.15}$ = 62.34 cal/mole-deg, is used to calculate temperature-X_{CO_2} topologies for reactions (11), (12) and (13) in Table 14, equilibrium curves which are about 50° to 100°C distant from the topologies of Slaughter et al. are obtained, even though their curves matched those calculated quite closely in reactions (14) through (16). In view of these discrepancies, it was decided to use established temperature-X_{CO_2} topologies to back calculate the thermodynamic properties of talc in a manner similar to that in which the thermodynamic data for spurrite, tilleyite and rankinite was obtained.

After consideration of the available experimental data on reactions involving talc, the equilibrium curves of reactions (12) and (13) determined by Slaughter et al. were utilized to calculate ΔH^{o}_{f} of talc.

Slaughter et al. used a combination of thermochemical and experimental data to construct their equilibrium curves using an experimentally determined equilibrium point from which they could base their calculations without enthalpy data. However, in their calculations, they did assume $S^{o}_{298.15}$ of talc to be 62.34 cal/mole-deg.

Points along the equilibrium curves for reactions (12) and (13) were chosen and ΔH^{o}_{f} of talc was calculated at each using the entropy 62.34 cal/mole-deg assumed to be correct by Slaughter et al. An average value of ΔH^{o}_{f} of talc was then used to construct the same equilibrium curve from which it was derived to evaluate its ability to reproduce the experimental data; the value of ΔH^{o}_{f} of talc that best fit the available data when $S^{o}_{298.15}$ of talc equalled 62.34 cal/mole-deg was -1415700 cal/mole. The temperature-X_{CO_2} topologies shown in Figures 12 to 14 were then calculated using this computed talc data and therefore, at least in the case of reactions (12) and (13), their correspondence with the equilibrium curves of Slaughter et al. should be quite good.

DESCRIPTION OF MINERAL EQUILIBRIA IN TERMS OF CHEMICAL VARIATION

Introduction

The change of the Gibbs free energy of a system can be expressed by the relation

$$dG = VdP - SdT + \sum_i \mu_i dn_i \qquad (42)$$

where G is the total Gibbs free energy of the system, μ_i is equal to the chemical potential of the ith component and n_i is the number of moles of the ith component. From this equation, it is clear that free energy is not only a function of temperature and pressure but is also a function of the changing composition of the system because chemical potential, also known as the partial molal Gibbs free energy, is defined by

$$\mu_i = \left(\frac{\partial G}{\partial n_i}\right)_{T,P,n_j} \qquad (43)$$

where n_j represents the number of moles of each of the components in the system except i. Chemical potential therefore reflects the dependence of the Gibbs free energy of a system on the change in the number of moles of a component in the system at constant temperature, pressure and n_j. In fact, the chemical potential of each component in the system may be regarded as that component's contribution to the system's total free energy. Because changes in the total Gibbs free energy of a system are reflected by changes in its mineralogy, a system's compositional change, represented by changes in the chemical potentials of its components, is of as much importance as temperature and pressure in defining mineral equilibria.

Composition and Chemical Potential

Triangular composition diagrams in which tie lines are drawn between coexisting pairs of minerals are often used to illustrate mineral equilibria in a given system at a specified temperature and pressure. A series of these compositional triangles constructed over a range of temperature and pressure reflects the succession of equilibrium states attained in the system. However, Helgeson (1968) also recommends the use of orthogonal plots of mineral composition because of their relation to chemical potential diagrams.

Helgeson pointed out that equilibrium between two minerals at a given temperature and pressure requires that the chemical potential of any given component must be the same in each phase. Extending this consequence of equilibrium to all components in the two minerals results in the equation

$$n_{\phi_1} \sum_{i}^{q} n_{i(\phi_1)} d\mu_i = n_{\phi_2} \sum_{i}^{q} n_{i(\phi_2)} d\mu_i \qquad (44)$$

where n_{ϕ_1} and n_{ϕ_2} refer to the number of moles of mineral phases ϕ_1 and ϕ_2 in the equilibrium state, n_i is equal to the number of moles of component i in each mole of the mineral and μ_i refers to the chemical potential of the ith component.

Assuming the presence of three components, equation (44) can be expanded and rearranged such that

$$\frac{d\mu_1}{d\mu_2} = -\frac{n_{\phi_1} n_{2(\phi_1)} - n_{\phi_2} n_{2(\phi_2)}}{n_{\phi_1} n_{1(\phi_1)} - n_{\phi_2} n_{1(\phi_2)}} - \left(\frac{n_{\phi_1} n_{3(\phi_1)} - n_{\phi_2} n_{3(\phi_2)}}{n_{\phi_1} n_{1(\phi_1)} - n_{\phi_2} n_{1(\phi_2)}} \cdot \frac{d\mu_3}{d\mu_2} \right). \qquad (45)$$

If i=3 is conserved in the solid phases, that is,

$$n_{\phi_1} n_{3(\phi_1)} = n_{\phi_2} n_{3(\phi_2)} \quad , \tag{46}$$

equation (45) can be written as

$$\frac{d\mu_1}{d\mu_2} = - \frac{n_{\phi_1} n_{2(\phi_1)} - n_{\phi_2} n_{2(\phi_2)}}{n_{\phi_1} n_{1(\phi_1)} - n_{\phi_2} n_{1(\phi_2)}} = - \frac{n_{2(\phi_1)}/n_{3(\phi_1)} - n_{2(\phi_2)}/n_{3(\phi_2)}}{n_{1(\phi_1)}/n_{3(\phi_1)} - n_{1(\phi_2)}/n_{3(\phi_2)}} \quad . \tag{47}$$

Equation (47) states that the negative reciprocals of the slopes of tie lines on orthogonal composition diagrams constructed in this manner are equivalent to the slopes on the corresponding chemical potential diagrams at the same temperature and pressure. An orthogonal composition diagram illustrating the appropriate mineral stabilities at the temperature and pressure of interest can therefore be used to construct a diagram, portraying the same equilibrium phase relations in terms of variations in the chemical potentials of the components taken into consideration, directly from geometric relationships.

Figure 22, a triangular composition diagram illustrating experimental phase equilibria in the system CaO-MgO-SiO_2 at 800°C and 1 bar, was obtained from Brown (1971) and recast into the orthogonal plots shown in Figures 23 and 24. Note that in Figure 23, CaO is conserved among the solid phases but that in Figure 24 SiO_2 is conserved. The choice of the component to be conserved is one of convenience. It is usually one of the least descriptive variables in the system, such that little information about the state of the system is lost upon its conservation. Therefore, Figure 23 might conveniently illustrate phase relations in impure but CaO-rich limestones, whereas Figure 24 might be of great use in describing phase relations in systems rich in quartz or other silicates.

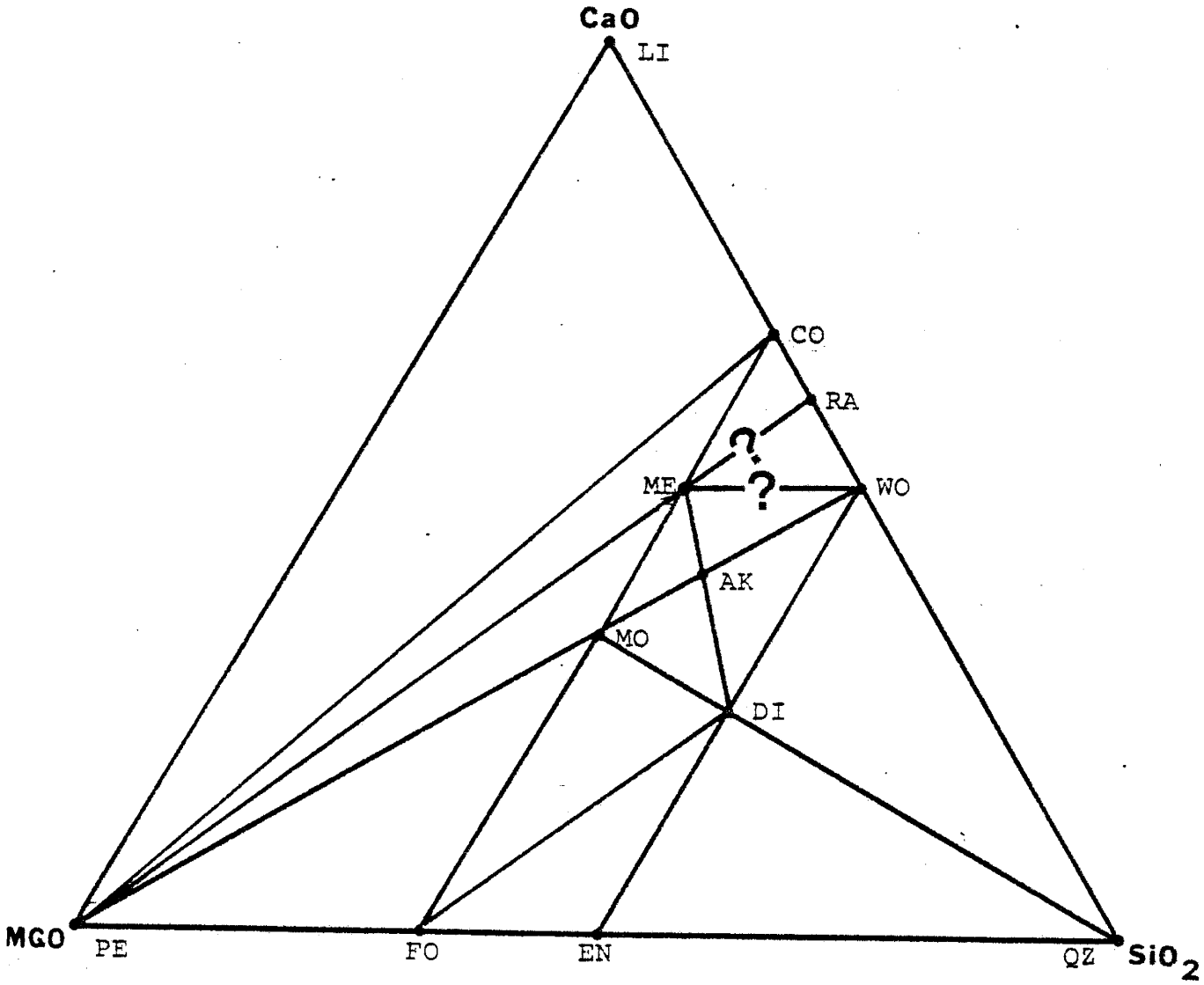

Figure 22. Triangular composition diagram illustrating equilibrium phase relations in the system CaO-MgO-SiO_2 at 800°C and 1 bar (Brown, 1971). LI=lime, CO=Ca-olivine, RA=rankinite, WO=wollastonite, QZ=quartz, PE=periclase, FO=forsterite, EN=clinoenstatite, DI=diopside, MO=monticellite, ME=merwinite, AK=akermanite.

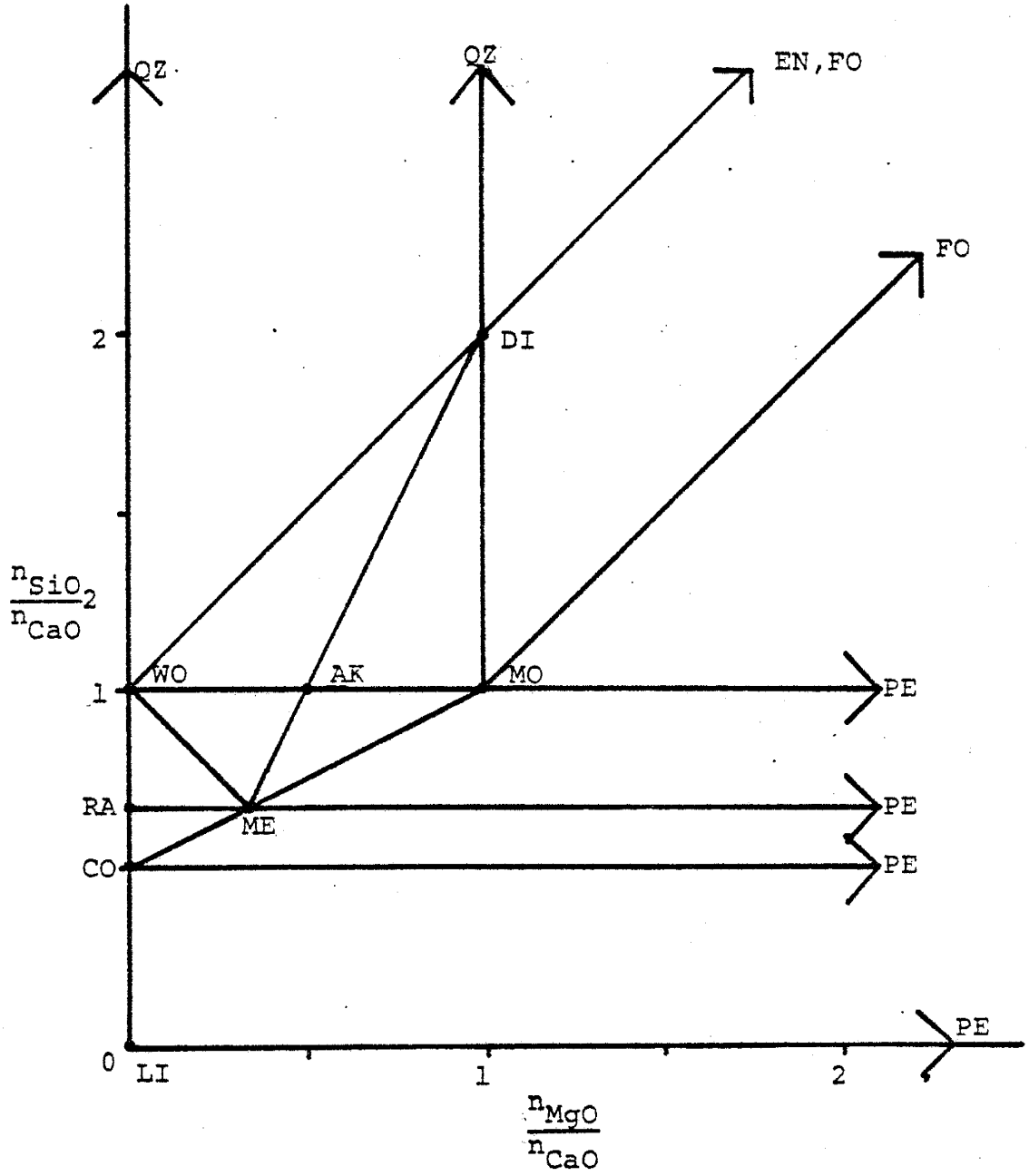

Figure 23. Orthogonal composition diagram illustrating the same phase equilibria as depicted in Figure 22 at 800°C and 1 bar in the system CaO-MgO-SiO_2 but conserving CaO in the solid phases.

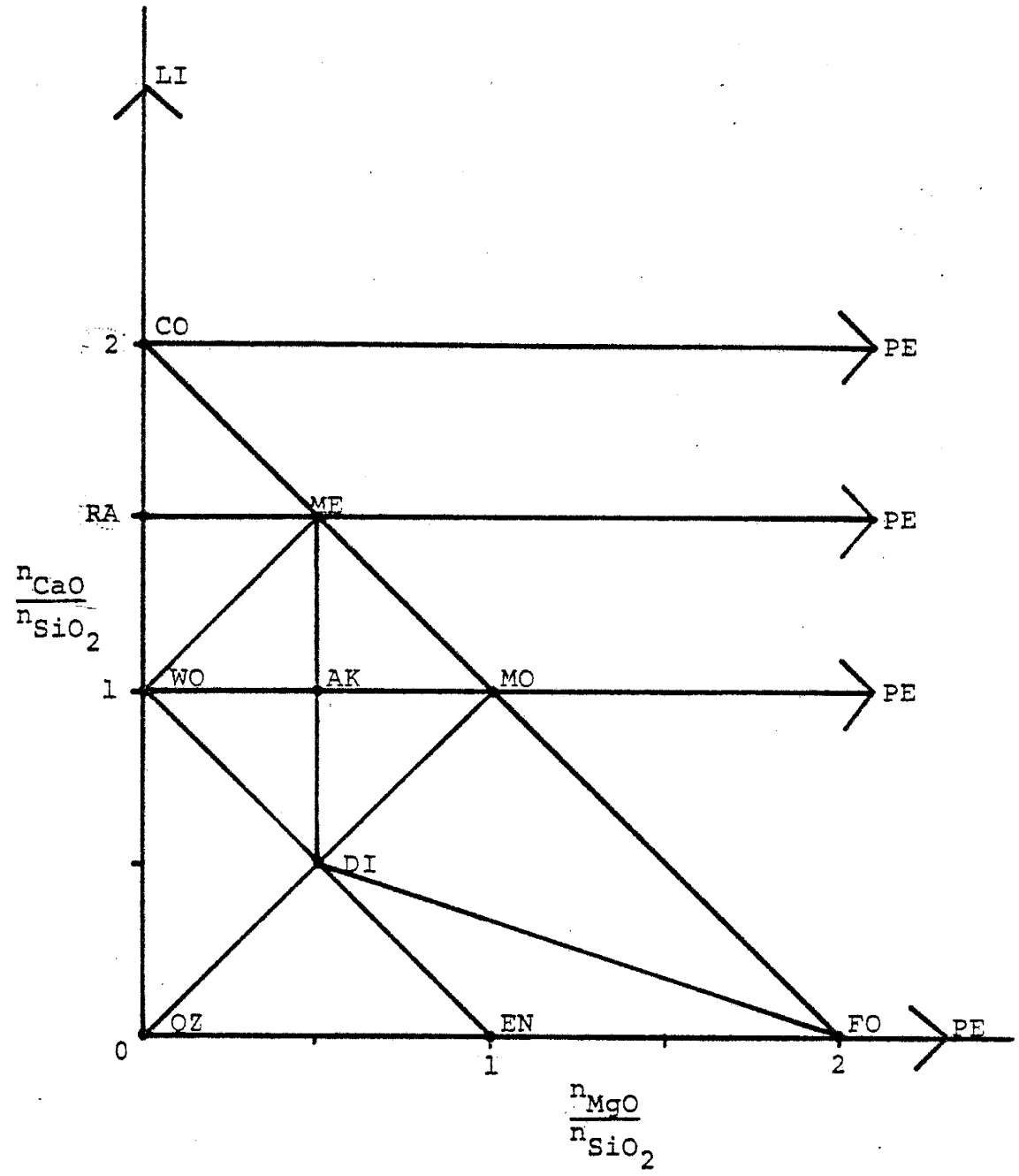

Figure 24. Orthogonal composition diagram illustrating the same phase equilibria as depicted in Figure 22 at 800°C and 1 bar in the system CaO-MgO-SiO_2 but conserving SiO_2 in the solid phases.

The tie lines between wollastonite and merwinite and between merwinite and rankinite denoted by question marks in Figure 22 are not well documented by experimental data at this temperature and pressure and therefore the equilibrium phase relations in this part of the diagram are unclear. Thermodynamic data can be used to establish the equilibrium phase relations among the minerals involved— namely, wollastonite, merwinite, rankinite, Ca-olivine and akermanite— in order to determine which tie lines between these minerals represent thermodynamically stable assemblages. It was assumed that the experimentally determined solid tie lines in Figure 22 are accurate.

There are a total of four mineral pairs that could exist in the compositional space within the area bounded by the minerals listed above: 1) wollastonite-merwinite, 2) rankinite-merwinite, 3) akermanite-rankinite, and 4) akermanite-Ca-olivine. Consideration of the Gibbs free energy of reaction at the temperature and pressure of interest (calculated by evaluating equation 22) between any two of these mineral pairs whose tie lines cross permits the identification of the stable pair— that is, the pair with the lowest Gibbs free energy under the prevailing conditions. Repetition of this procedure for all possible combinations of the mineral pairs using the thermodynamic data in Appendix A yielded the equilibrium phase relations illustrated in Figures 23 and 24 at 800°C and 1 bar.

According to equation (47), chemical potential diagrams drawn in terms of μ_{SiO_2} versus μ_{MgO} and μ_{CaO} versus μ_{MgO} could be constructed from the orthogonal composition diagrams in Figures 23 and 24, respectively. However, the diagrams would be merely schematic and would not reflect quantitative relationships which would facilitate their application to natural systems. Therefore, a quantitative means of representing equilib-

rium phase relations in terms of chemical potential or a related variable is needed.

Activity-Activity Diagrams

Many mineral assemblages exist in equilibrium with an aqueous phase and researchers, seeking a practical means of describing the chemical variation of such a system, have found it convenient to represent the chemical potentials of a system's components in terms of the composition of the coexisting aqueous phase. If the solid phases comprising the mineral assemblage are assumed to be in equilibrium with the aqueous phase, the chemical potential of any given component in the mineral assemblage is equal to its chemical potential in the associated aqueous phase. Therefore, one can represent the changing chemical potential of the components in the mineral assemblage by the changing composition of the aqueous phase. As a matter of convenience, the oxides are used to define the composition of the phases in the system.

For example, consider the reaction

$$CaO(c) + 2H^{+} \rightleftharpoons Ca^{++} + H_2O \qquad (48)$$

for which

$$\log K_{r,T,P} = \log \frac{a_{Ca^{++}}}{(a_{H^{+}})^2} - \log a_{CaO(c)} \qquad (49)$$

where $a_{CaO(c)}$ refers to the activity of the CaO component in the mineral assemblage at the specified temperature and pressure assuming $a_{H_2O} = 1$. Rearranging equation (49) yields

$$\log a_{CaO(c)} = \log \frac{a_{Ca^{++}}}{(a_{H^{+}})^2} - \log K_{r,T,P} \; . \qquad (50)$$

Because

$$\mu_{CaO(c)} = \mu^{\circ}_{CaO(c)} + RT\ln a_{CaO(c)} \quad , \tag{51}$$

a combination of this equation with equation (50) gives

$$\mu_{CaO(c)} = \mu^{\circ}_{CaO(c)} + RT\left(\ln \frac{a_{Ca^{++}}}{(a_{H^+})^2} - \ln K_{r,T,P}\right) \quad , \tag{52}$$

which, when differentiated, yields

$$d\mu_{CaO(c)} = RT d\ln \frac{a_{Ca^{++}}}{(a_{H^+})^2} \quad . \tag{53}$$

Thus, the changing ratio of $a_{Ca^{++}}/(a_{H^+})^2$ in the aqueous phase can be used to represent the changing chemical potential of the CaO component in the solid phases.

Activity-activity diagrams are used to represent the equilibrium relations among minerals and an aqueous phase in terms of the logarithm of the activity ratios chosen as the axes of the diagrams. The computer program DIAGRAM (Brown, 1970) carries out the calculations involved in constructing activity-activity diagrams and also includes a CALCOMP plotting routine to draw the diagrams.

For example, consider the construction of an activity-activity diagram plotting log $a_{Ca^{++}}/(a_{H^+})^2$ versus log $a_{Mg^{++}}/(a_{H^+})^2$ and the positioning of the stability field boundary between wollastonite and diopside on this diagram, conserving SiO_2 between the two solids. Equilibrium between wollastonite and diopside in the presence of an aqueous phase can be expressed by

$$2H^+ + Mg^{++} + 2CaSiO_3 \rightleftharpoons CaMgSi_2O_6 + Ca^{++} + 2H^+ \tag{54}$$

for which

$$\log K_{r,T,P} = \log \frac{a_{Ca}^{++}}{(a_{H}^{+})^2} - \log \frac{a_{Mg}^{++}}{(a_{H}^{+})^2} \quad . \qquad (55)$$

Upon rearranging equation (55) in the form of a straight line ($y = mx + b$) on the appropriate activity-activity diagram such that

$$\log \frac{a_{Ca}^{++}}{(a_{H}^{+})^2} = \log \frac{a_{Mg}^{++}}{(a_{H}^{+})^2} + \log K_{r,T,P} \quad , \qquad (56)$$

it is evident that $\log K_{r,T,P}$ represents the intercept (b) of the wollastonite-diopside stability field boundary on the diagram and that the slope (m) of this boundary is +1. Repetition of this procedure for all possible mineral pairs in the system under consideration will yield a mineral stability diagram such as Figure 34 which depicts stability fields of minerals in terms of the composition of the aqueous phase. Only the minerals that are stable under the prevailing physical and chemical conditions will be represented.

Although the positioning of the stability field boundaries between minerals on these diagrams will shift with changing temperature and pressure owing to the change in the values of $\log K_{r,T,P}$, the geometry of the field boundaries will remain the same because it is dependent only on the stoichiometry of the reactions. It must also be remembered that even though the aqueous phase does not appear explicitly in these diagrams, it is a coexisting phase in all stability fields.

In order to justify the theoretical basis for constructing activity-activity diagrams in terms of the composition of the aqueous phase, it was necessary to assume that an aqueous phase coexists with such mineral assemblages. However, it is also possible to directly compute the chemical potential of the oxide components in the minerals without specifying the

presence of an aqueous phase. To accomplish this, the standard or reference state for oxide components such as $SiO_2(c)$, CaO(c) and MgO(c) is assumed to be the pure solid oxide at the temperature and pressure of interest. Thus, $\Delta G^\circ_{r,T,P}$ of the pure solid oxide and the oxide component are identical and $\Delta G_{r,T,P}$ for a reaction such as CaO(s) $\rightleftharpoons$ CaO(c) is equal to $RT\ln a_{CaO(c)}$. That is, ΔG°_r at any temperature and pressure for the reaction

$$CaO(s) \rightleftharpoons CaO(c) \tag{57}$$

is equal to zero according to the standard states chosen in this paper and therefore

$$\Delta G_{r,T,P} = RT\ln a_{CaO(c)} \tag{58}$$

which represents the free energy associated with the conversion of CaO from a pure phase to a component in a crystalline phase. Consequently, equilibria between minerals can be written in terms of their dissociation to their component oxides instead of their hydrolysis in the aqueous phase. A treatment similar to that described above will yield activity-activity diagrams such as Figure 26 in which $\log a_{CaO(c)}$ versus $\log a_{MgO(c)}$ is plotted. These diagrams, in contrast to those described earlier, can be constructed at all temperatures and pressures irregardless of the presence (or absence) of an aqueous phase.

A comparison of an activity-activity diagram constructed by assuming the presence of an aqueous phase with a diagram at the same temperature and pressure plotting the activities of the component oxides themselves reveals that although the two have the same geometry, their stability field boundaries differ numerically. Equation (49) shows that the proportionality constant between the stability field boundaries is equal to $\log K_{r,T,P} - \log f_{H_2O}$ where r refers to a reaction of the type

$$CaO(c) + 2H^{+} \rightleftharpoons Ca^{++} + H_2O \qquad (48)$$

and therefore

$$\log K_{r,T,P} - \log f_{H_2O} = \log \frac{a_{Ca^{++}}}{(a_{H^+})^2} - \log a_{CaO(c)} \quad . \qquad (49)$$

Differentiation of equation (49) yields

$$\text{dlog } a_{CaO(c)} = \text{dlog } \frac{a_{Ca^{++}}}{(a_{H^+})^2} \qquad (59)$$

which demonstrates that the two types of diagrams, when determined at the same temperature and pressure, are equivalent in derivative space, i.e., slopes of the tie lines:

$$\frac{\text{dlog } \dfrac{a_{Ca^{++}}}{(a_{H^+})^2}}{\text{dlog } \dfrac{a_{Mg^{++}}}{(a_{H^+})^2}} = \frac{\text{dlog } a_{CaO(c)}}{\text{dlog } a_{MgO(c)}} \quad . \qquad (60)$$

In addition, a comparison of the slopes on both of these diagrams with the slopes of the tie lines on the corresponding orthogonal composition diagrams reveals that they are the negative reciprocals of each other. The relationship between slopes on an orthogonal composition diagram and a chemical potential diagram has been carried over to both of these diagrams because, according to extensions of equations (53) and (51), respectively,

$$\frac{d\mu_{CaO(c)}}{d\mu_{MgO(c)}} = \frac{RT\text{dln } \dfrac{a_{Ca^{++}}}{(a_{H^+})^2}}{RT\text{dln } \dfrac{a_{Mg^{++}}}{(a_{H^+})^2}} = \frac{\text{dlog } \dfrac{a_{Ca^{++}}}{(a_{H^+})^2}}{\text{dlog } \dfrac{a_{Mg^{++}}}{(a_{H^+})^2}} \qquad (61)$$

and

$$\frac{d\mu_{CaO(c)}}{d\mu_{MgO(c)}} = \frac{RTd\ln a_{CaO(c)}}{RTd\ln a_{MgO(c)}} = \frac{d\log a_{CaO(c)}}{d\log a_{MgO(c)}} \quad . \qquad (62)$$

The thermodynamic data used to construct the activity diagrams in this paper is listed in Appendix A. Several simplifying assumptions were made both to facilitate calculations and because of the unavailability of certain types of data at the time of this study. For example, the net compressibility and thermal expansion of a given reaction involving only condensed phases were assumed to be zero. In addition, the net change of the volume of ions involved in reactions between minerals was assumed to be independent of temperature and pressure because of the lack of an adequate equation of state for aqueous electrolytes. However, it is known that volumes of ions vary significantly at elevated temperatures and pressures and therefore activity-activity diagrams plotting the ratios of the activities of ions were limited to temperatures and pressures below 300°C and 1000 bars. To illustrate mineral equilibria above these limits, activity -activity diagrams utilizing the activities of the component oxides as variables were constructed because these diagrams are not affected by the phenomena described above.

The Utilization of Activity-Activity Diagrams in the Study of Mineral Equilibria

A comparison of the activity diagrams in Figures 25 and 26 with the orthogonal composition diagrams in Figures 23 and 24 drawn at 800°C and 1 bar verifies the relationship described by equation (47); namely, the slopes on diagrams plotting the activity of the oxide components are the negative reciprocals of the slopes on the corresponding orthogonal com-

Figure 25. Activity diagram for the system CaO-MgO-SiO_2 at 800°C and 1 bar. Abbreviations used in this and all following diagrams are: AQTZ= α-quartz, BQTZ= β-quartz, CA-O=Ca-olivine , CLIN= clinoenstatite, DIOP=diopside, FORS=forsterite, MERW=merwinite, MONT=monticellite, RANK=rankinite , SPUR=spurrite, TALC=talc, TILL=tilleyite, TREM=tremolite, WOLL=wollastonite. Saturation lines for the designated minerals are superimposed on the diagrams.

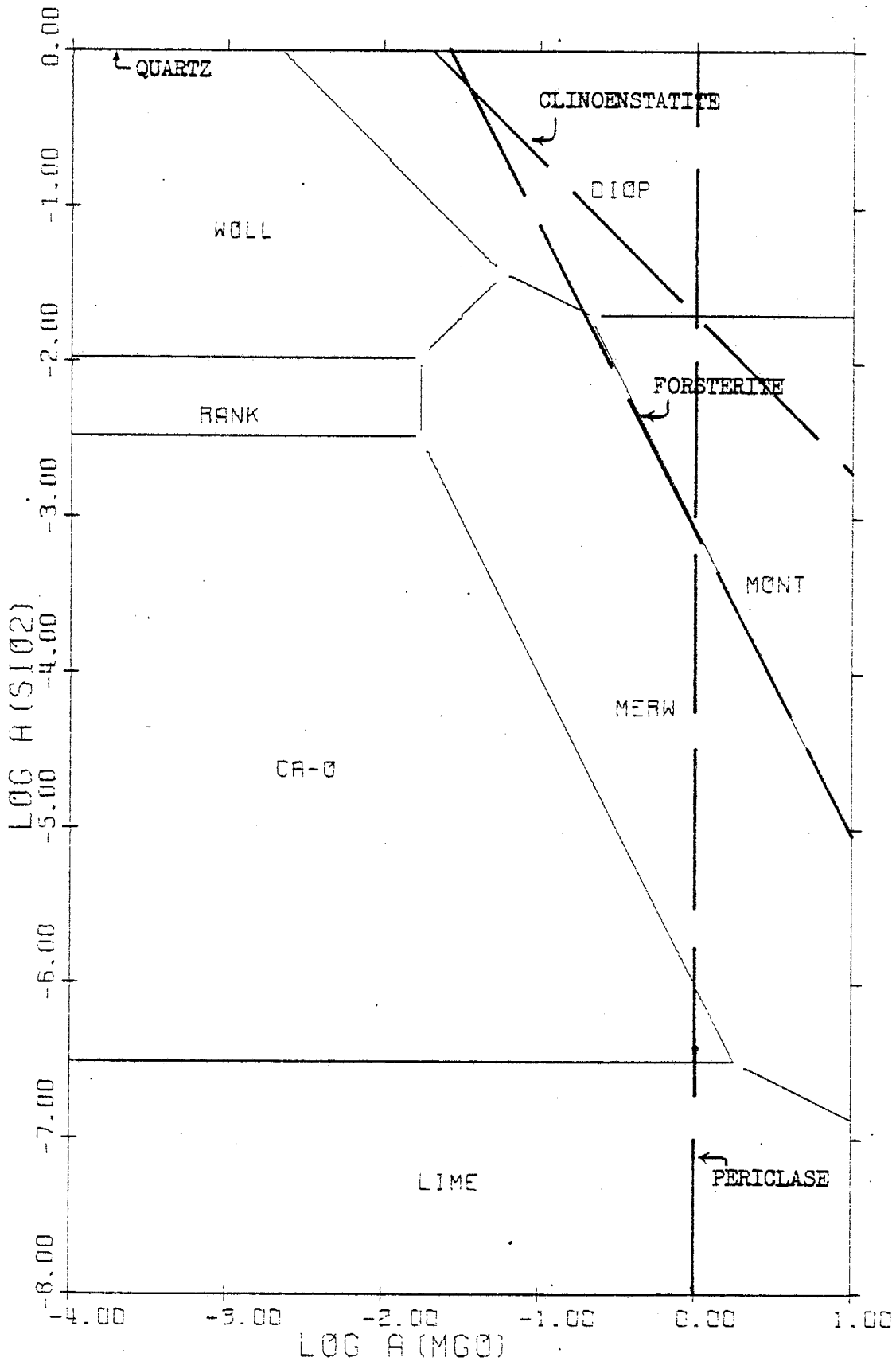
QUARTZ
CLINOENSTATITE
DIOP
WOLL
RANK
FORSTERITE
MONT
MERW
CA-O
LIME
PERICLASE
0.00
-1.00
-2.00
-3.00
-4.00
-5.00
-6.00
-7.00
-8.00
LOG A(SIO2)
-4.00
-3.00
-2.00
-1.00
0.00
1.00
LOG A(MGO)

Figure 26. Activity diagram for the system $CaO-MgO-SiO_2$ at 800°C and 1 bar.

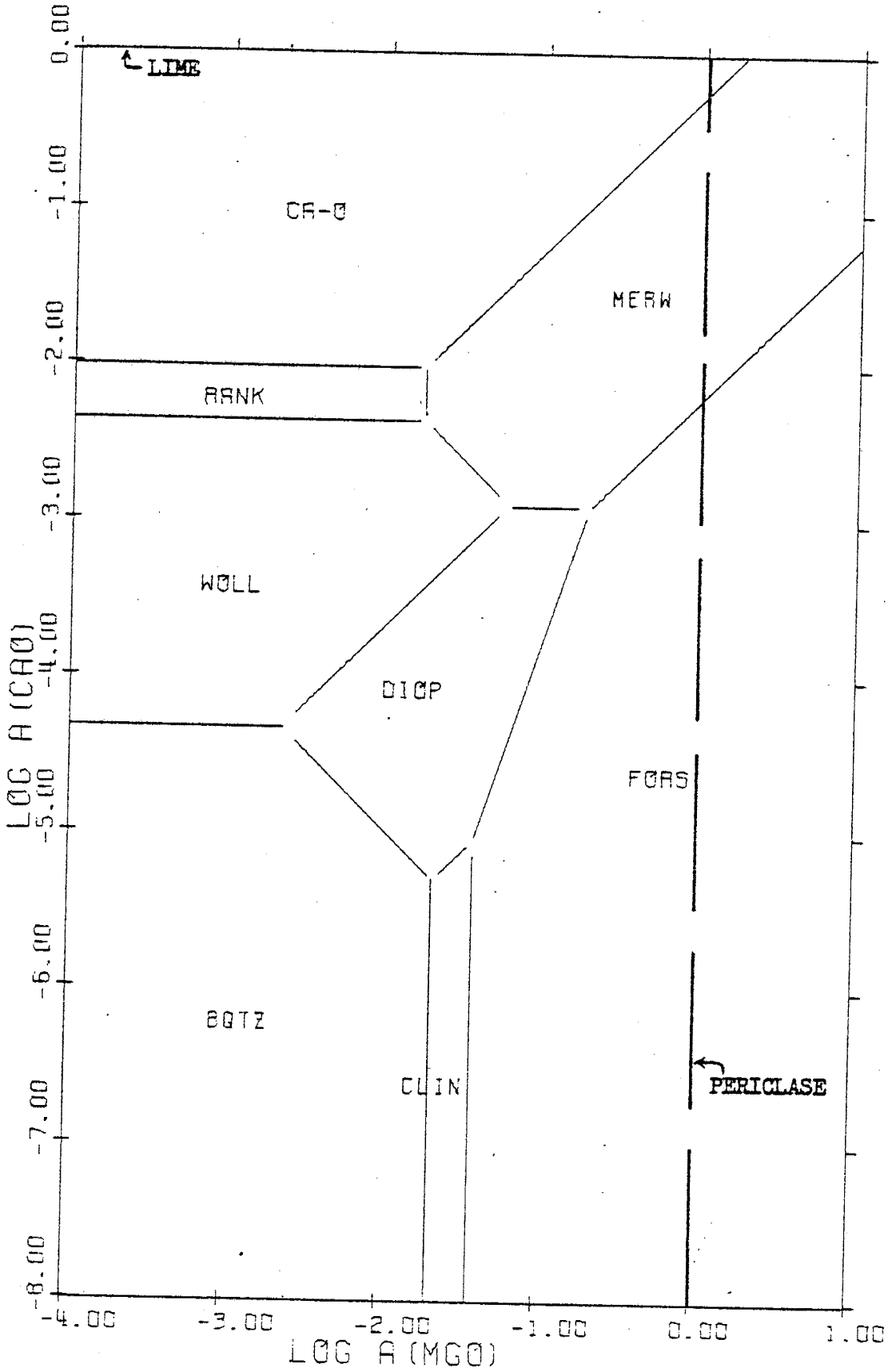
LIME
CA-O
MERW
RANK
WOLL
DIOP
FORS
BOTZ
CLIN
PERICLASE
0.00
-1.00
-2.00
-3.00
-4.00
-5.00
-6.00
-7.00
-8.00
LOG A(CAO)
-4.00
-3.00
-2.00
-1.00
0.00
1.00
LOG A(MGO)

position diagrams. Because these activity diagrams were constructed wholly from thermodynamic data, it is not surprising that they exhibit some equilibrium phase relations which are different than those suggested by analogous experimental data. The major discrepancies between the computed activity diagrams and the corresponding experimental composition diagrams are: 1) the absence of monticellite in Figure 26, and 2) the absence of akermanite in both Figures 25 and 26. The absence of akermanite at 800°C and 1 bar in contrast to its presence in the composition diagrams would seem to indicate that the thermodynamic data for this mineral is not in keeping with its natural occurrences. A similar explanation would account for the absence of monticellite in Figure 26. However, it should be noted that monticellite does occupy a stability field in Figure 25, drawn at the same temperature and pressure. This apparent discrepancy is probably related to the assumptions involved in constructing the activity diagrams; that is, both diagrams illustrate phase relations in the system CaO-MgO-SiO_2 but utilize changes in the activities of different components to do so (i.e., descriptive variables). Minerals that occupy stability fields on one diagram yet not the other at the same temperature and pressure reflect the effects of changing the activity of SiO_2(c) in one diagram while maintaining it at a constant value in another and varying the activity of CaO(c) instead.

The stability fields labelled lime in Figure 25 and β-quartz in Figure 26 represent chemical potential space in which none of the minerals in the system are stable except for the pure oxide equivalent of the oxide component conserved in the solid phases. If an aqueous phase is assumed to be present, these fields refer to chemical potential space in which the

aqueous phase is not saturated with respect to any minerals except that component which was originally assumed to be conserved in the solid phases and thus is in equilibrium with the aqueous solution. Note that the state of the oxide component is the thermodynamically stable one at the temperature and pressure of interest (i.e., β-quartz instead of α-quartz at 800°C and 1 bar, as in Figure 26).

Unfortunately, the log $a_{SiO_2(c)}$ versus log $a_{MgO(c)}$ diagrams cannot depict the stability of minerals which do not contain CaO because this component is assumed to be conserved, and thus present, in all solid phases. Therefore, the stability of minerals such as clinoenstatite and forsterite must be represented by means of saturation lines instead. These lines are constructed by calculating log $K_{r,T,P}$ for the dissociation of these minerals to their component oxides and then evaluating their slopes on the activity diagrams in terms of the variables represented on the diagram's axes. For example, consider the construction of the saturation line for clinoenstatite for which log K_r at 800°C and 1 bar is equal to -1.68. The dissociation of clinoenstatite is represented by

$$MgSiO_3 \rightleftharpoons MgO(c) + SiO_2(c) \qquad (63)$$

such that

$$\log K_{r,T,P} = \log a_{MgO(c)} + \log a_{SiO_2(c)} = -1.68 \quad . \qquad (64)$$

The slope of the clinoenstatite saturation line on a diagram plotting log $a_{SiO_2(c)}$ versus log $a_{MgO(c)}$ would therefore be -1, its intercept -1.68. This same procedure was carried out to determine the saturation lines shown in Figure 25. When hydrous phases such as talc were involved in calculating saturation lines, necessary log f_{H_2O} data was obtained from Helgeson (1974).

In all activity diagrams, there are certain mandatory restrictions

upon potential solution composition. For example, on the diagrams plotting the logarithm of the activity of the oxide components, upper limits are automatically imposed upon the activities of the oxide components as soon as they achieve equilibrium with either their corresponding solid oxide or hydroxide. Similar saturation lines serve to restrict possible solution composition on activity diagrams plotting the ratios of activities of ions. For example, in Figure 34, drawn at 100°C, 1 bar and log f_{H_2O} = -0.007, the aqueous solution becomes saturated with respect to brucite at any value of log $a_{Ca^{++}}/(a_{H^+})^2$ when log $a_{Mg^{++}}/(a_{H^+})^2$ = 13.08, such that the reaction

$$Mg(OH)_2 + 2H^+ \rightleftharpoons Mg^{++} + 2H_2O \qquad (65)$$

is at equilibrium. Because

$$\log K_{r,T,P} = \log \frac{a_{Mg^{++}}}{(a_{H^+})^2} + 2\log f_{H_2O} \qquad (66)$$

for this reaction at equilibrium and log $K_{r,T,P}$ and log f_{H_2O} are fixed at the temperature and pressure under consideration, log $a_{Mg^{++}}/(a_{H^+})^2$ must also be fixed. From this example, it is apparent that the equilibration of minerals not otherwise occupying stability fields on the activity diagrams imposes upper limits upon the chemical potential of the components in the system. Additional restrictions on component chemical potential as reflected by solution composition may be incurred if the system contains CO_2 because the saturation lines of calcite, magnesite and dolomite must also be taken into account. Saturation lines are therefore crucial to the identification of stable mineral assemblages at a specified temperature, pressure, log f_{H_2O} and log f_{CO_2} because mineral stability fields beyond the limiting saturation lines cannot be reached in terms of component chemical potential. Consequently, the minerals they represent are not thermodynamically

stable under the prevailing conditions.

Because activity diagrams plotting log $a_{CaO(c)}$ versus log $a_{MgO(c)}$ and conserving SiO_2 in the solid phases are perhaps most useful in defining possible equilibria among the many silicate minerals in the system CaO-MgO-SiO_2-H_2O-CO_2, this type of diagram was used to illustrate equilibrium phase relations in the system mentioned above from 100° to 800°C and from 1 to 1000 bars in Figures 27 to 66. It should be noted that even though each activity diagram at a specified temperature and pressure depicts the stability of minerals in terms of the activities of the components in the system, a series of these diagrams over a range of temperature and pressure will also reveal the influence of these factors upon mineral equilibria. In fact, it is possible to trace a point of known chemical potential of the oxide components on an activity diagram through temperature-pressure space to study changing mineral stabilities from an isochemical viewpoint. Because the information obtained in this manner is analogous to that obtained from isochemical pressure-temperature diagrams, it should be possible to discern the dehydration, decarbonation and solid-solid reactions affecting mineral equilibria in response to changing temperature and pressure on these activity diagrams.

Equilibrium phase relations in the anhydrous system CaO-MgO-SiO_2 will be studied first as a function of temperature, pressure and component chemical potential to introduce several basic characteristics of the system. H_2O and CO_2 will then be added to the system to evaluate the effects of each upon mineral equilibria.

Figures 27, 28 and 29 were drawn at 400°, 600° and 800°C at 1 bar pressure to illustrate the response of minerals in the anhydrous system

Figure 27. Activity diagram for the system CaO-MgO-SiO_2 at 400°C and 1 bar.

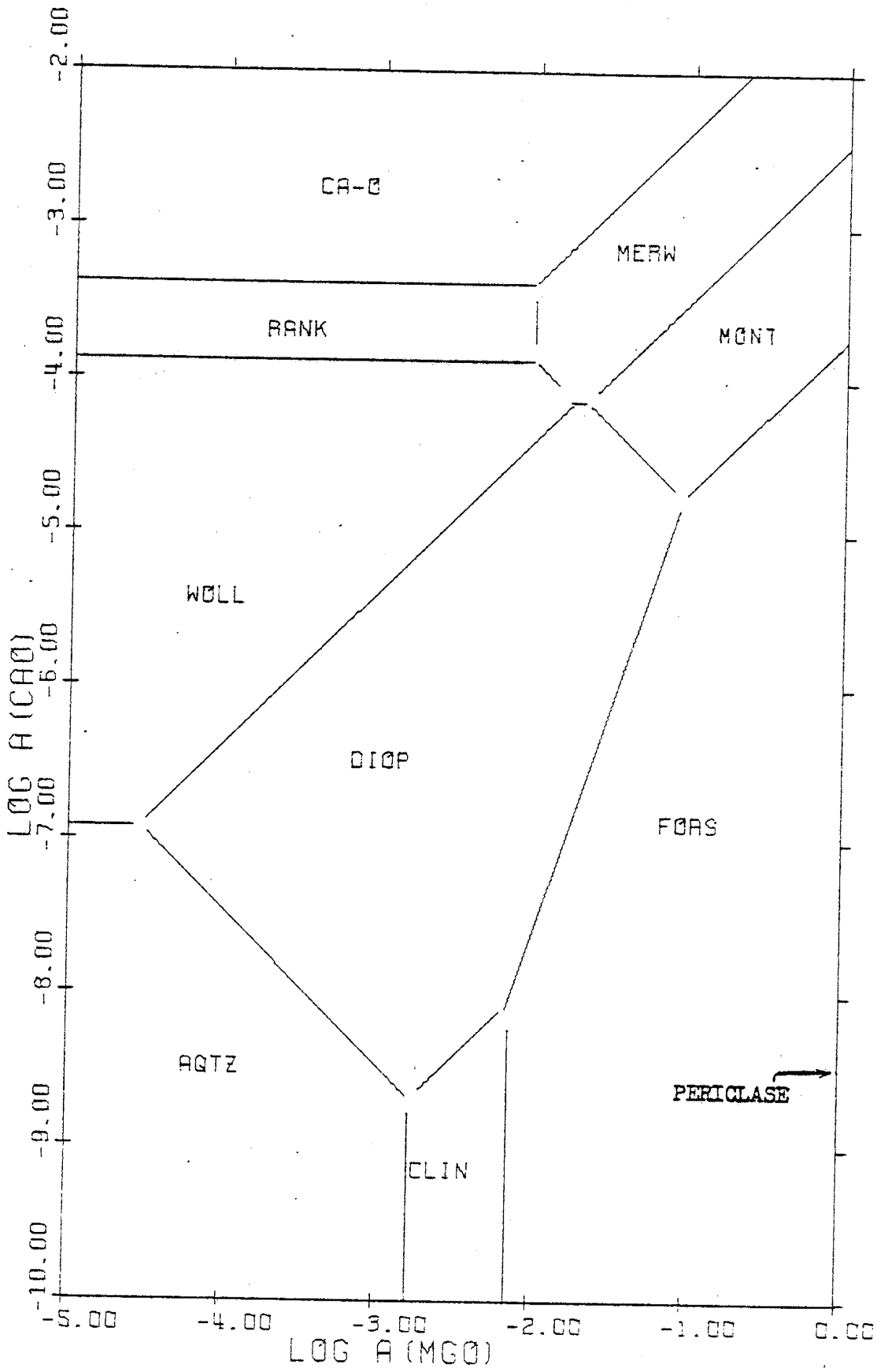
CA-C
MERW
RANK
MONT
WOLL
DIOP
FORS
AQTZ
PERICLASE
CLIN
-2.00
-3.00
-4.00
-5.00
-6.00
-7.00
-8.00
-9.00
-10.00
LOG A(CAO)
-5.00
-4.00
-3.00
-2.00
-1.00
0.00
LOG A(MGO)

Figure 28. Activity diagram for the system $CaO-MgO-SiO_2$ at 600°C and 1 bar.

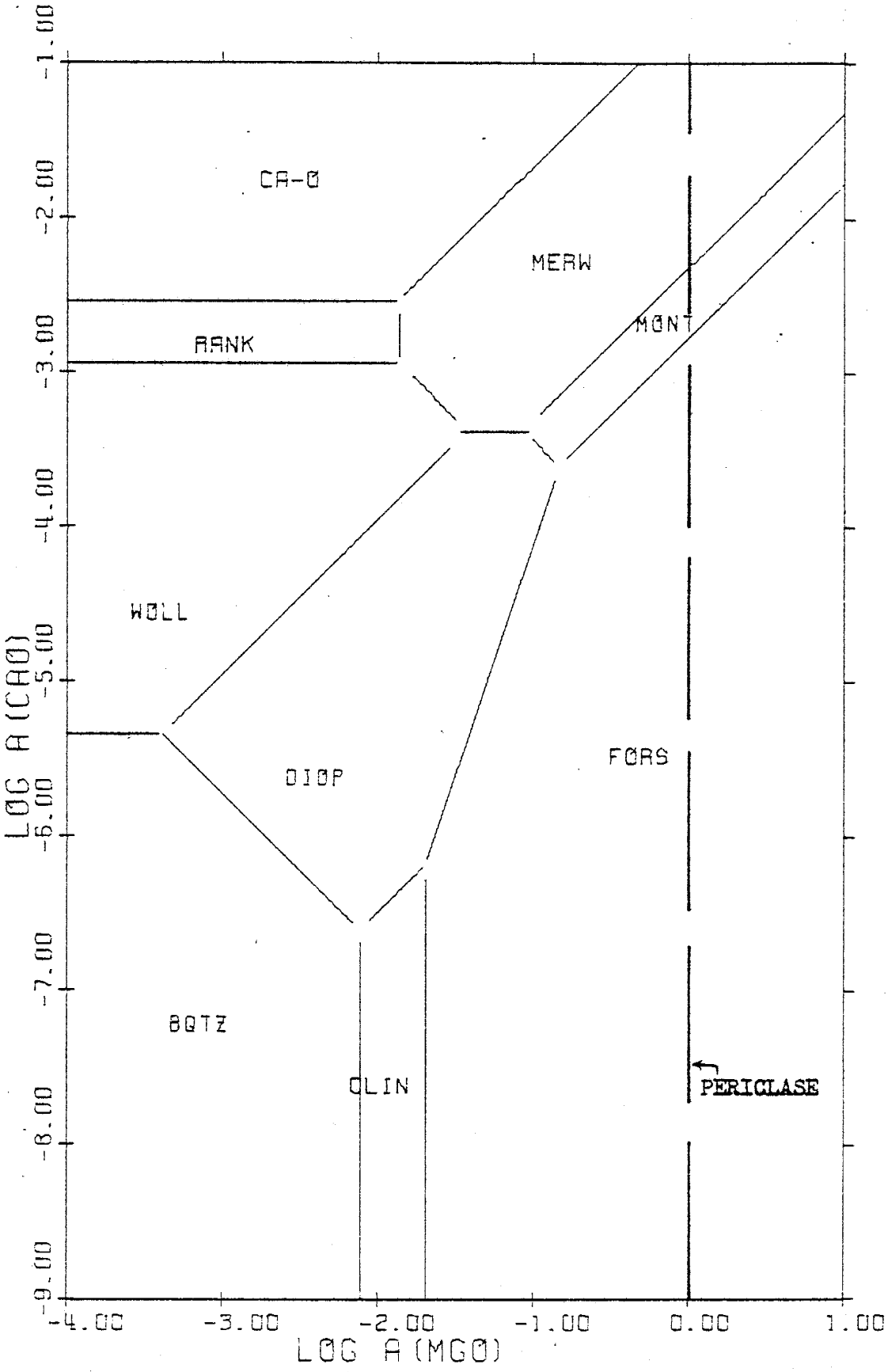
CA-O
MERW
MONT
RANK
WOLL
DIOP
FORS
QTZ
CLIN
PERICLASE
LOG A(CAO)
LOG A(MGO)
-1.00
-2.00
-3.00
-4.00
-5.00
-6.00
-7.00
-8.00
-9.00
-4.00
-3.00
-2.00
-1.00
0.00
1.00

Figure 29. Activity diagram for the system $CaO-MgO-SiO_2$ at 800°C and 1 bar.

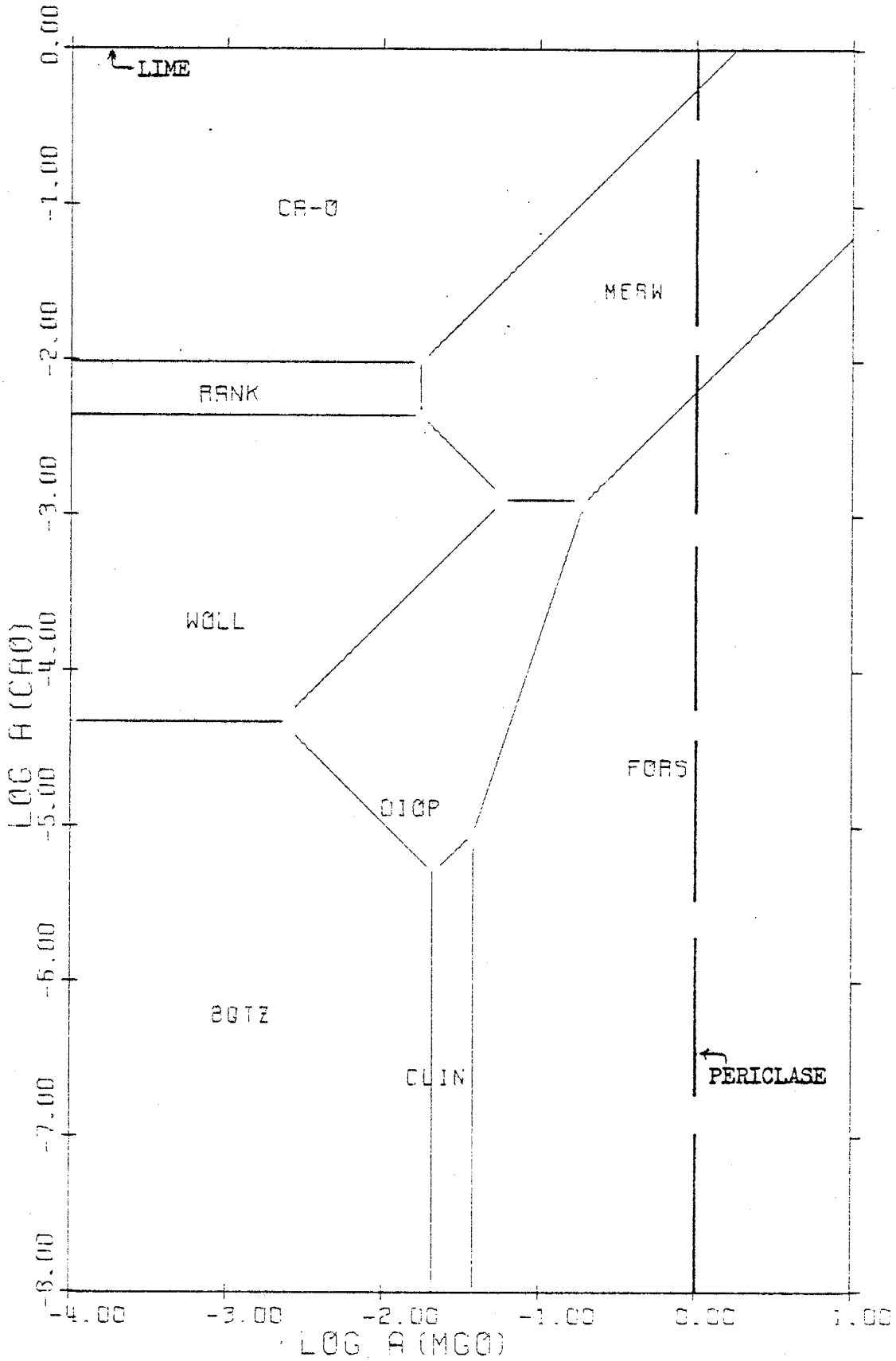
LIME
CA-O
MERW
RANK
WOLL
FORS
DIOP
BOTZ
CLIN
PERICLASE
LOG A (CAO)
LOG A (MGO)
0.00
-1.00
-2.00
-3.00
-4.00
-5.00
-6.00
-7.00
-8.00
-4.00
-3.00
-2.00
-1.00
0.00
1.00

$CaO-MgO-SiO_2$ to increasing temperature. They show that the stability field of the conserved component SiO_2 expands in size markedly with temperature. This is related to the log $K_{r,T,P}$ of reaction between quartz and the minerals bordering its stability field because log $K_{r,T,P}$ must become more positive as temperature increases to cause the expansion of the SiO_2 stability field. However, if we assume an aqueous phase to be present, this phenomenon more precisely represents the increasing solubility of minerals with rising temperature, such that greater activities of the oxide components are required to cause them to precipitate. The stability fields of diopside, wollastonite and clinoenstatite decrease in size with increasing temperature as a result of the expansion of the quartz field. Whereas rankinite becomes only slightly less stable as temperature increases, the stability field of monticellite totally disappears from these diagrams above 600°C, its stability field engulfed by that of merwinite which rapidly becomes more stable as temperature rises.

Figures 30, 31 and 32 attempt to show the effect of pressure upon the same anhydrous system at 600°C and 1, 500 and 1000 bars. Because the mineral stability fields depicted on these diagrams do not change appreciably with increasing pressure at a constant temperature, it appears that pressure has very little effect on anhydrous systems. This is a result of the fact that the volume change involved in solid-solid reactions is quite small and therefore its contribution to the Gibbs free energy of reaction (as shown in equation 22) is minimal. (As mentioned previously, it was assumed in this study that the net compressibility of the solid phases in solid-solid reactions was zero in order to facilitate calculations without significant error.)

Figure 33 was included in this series of diagrams to illustrate the result of omitting a phase such as rankinite from consideration on activity

Figure 30. Activity diagram for the system $CaO-MgO-SiO_2$ at 600°C and 1 bar.

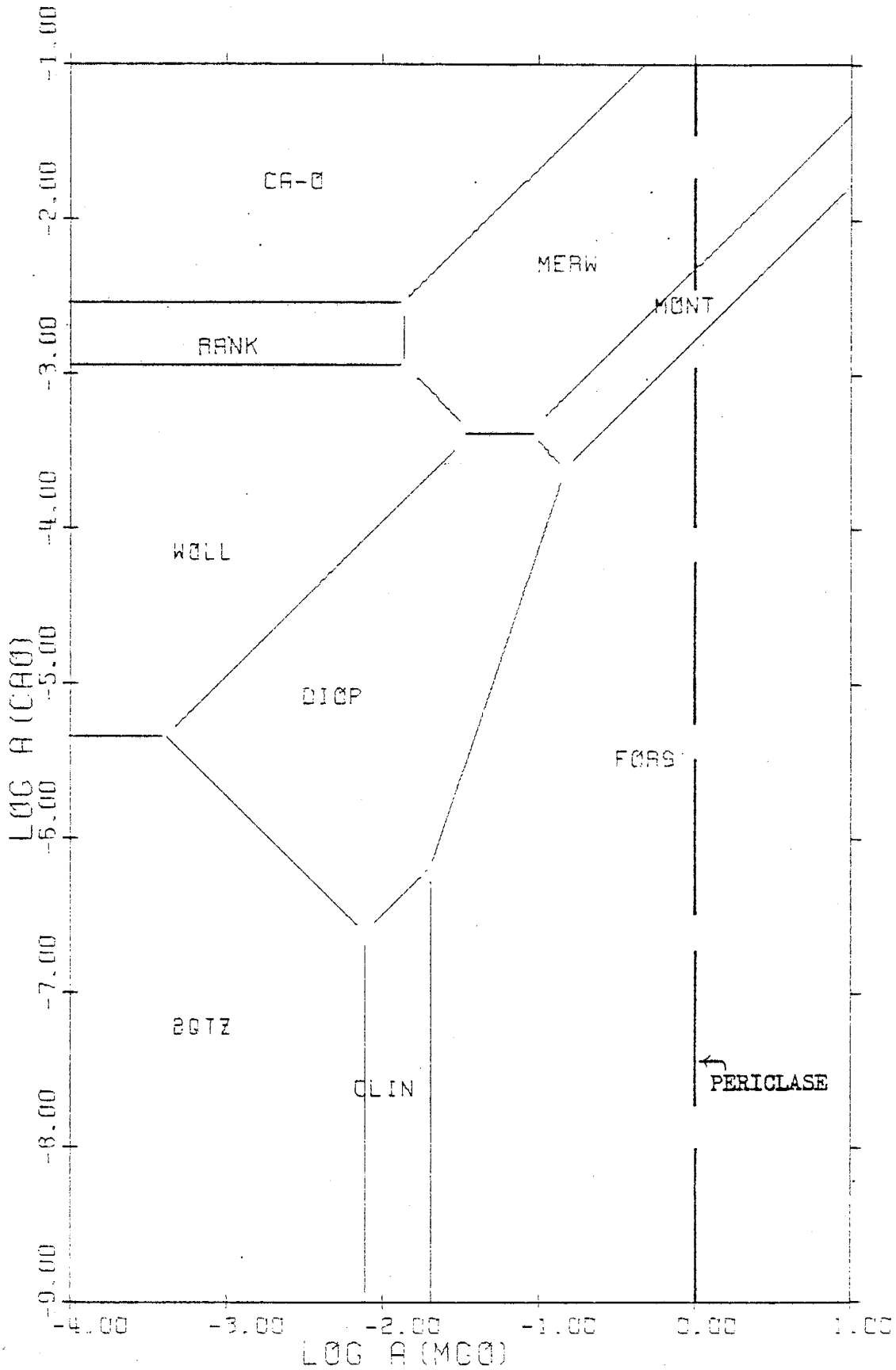
CA-O
MERW
MONT
RANK
WOLL
DIOP
FORS
ZOTZ
CLIN
PERICLASE
LOG A (CAO)
LOG A (MGO)
-1.00
-2.00
-3.00
-4.00
-5.00
-6.00
-7.00
-8.00
-9.00
-4.00
-3.00
-2.00
-1.00
0.00
1.00

Figure 31. Activity diagram for the system CaO-MgO-SiO_2 at 600°C and 500 bars.

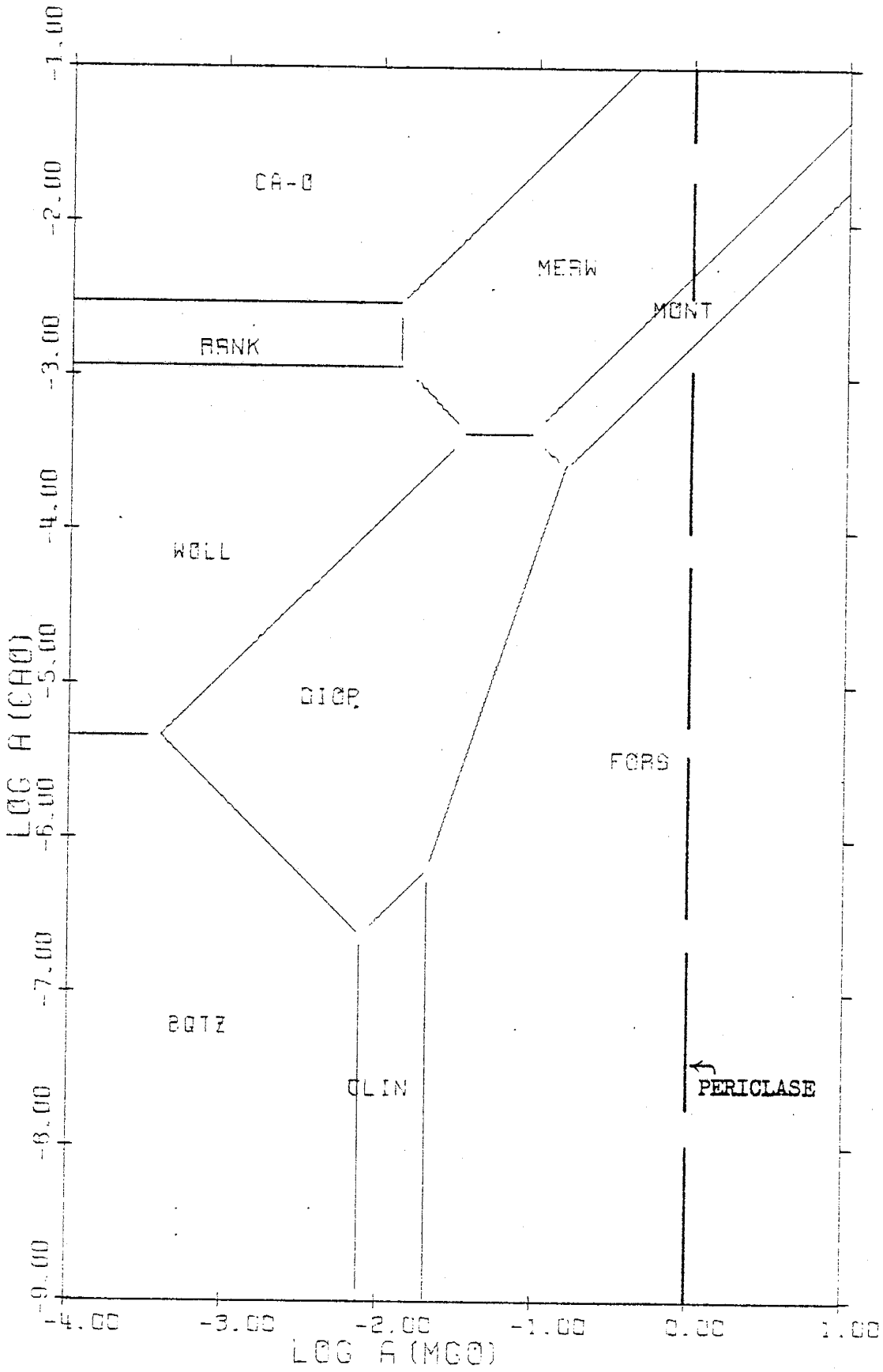
CA-O
MERW
MONT
RANK
WOLL
DIOP
FORS
OLIV
PERICLASE
LOG A(CAO)
LOG A(MGO)
-1.00
-2.00
-3.00
-4.00
-5.00
-6.00
-7.00
-8.00
-9.00
-4.00
-3.00
-2.00
-1.00
0.00
1.00

Figure 32. Activity diagram for the system CaO-MgO-SiO_2 at 600°C and 1000 bars.

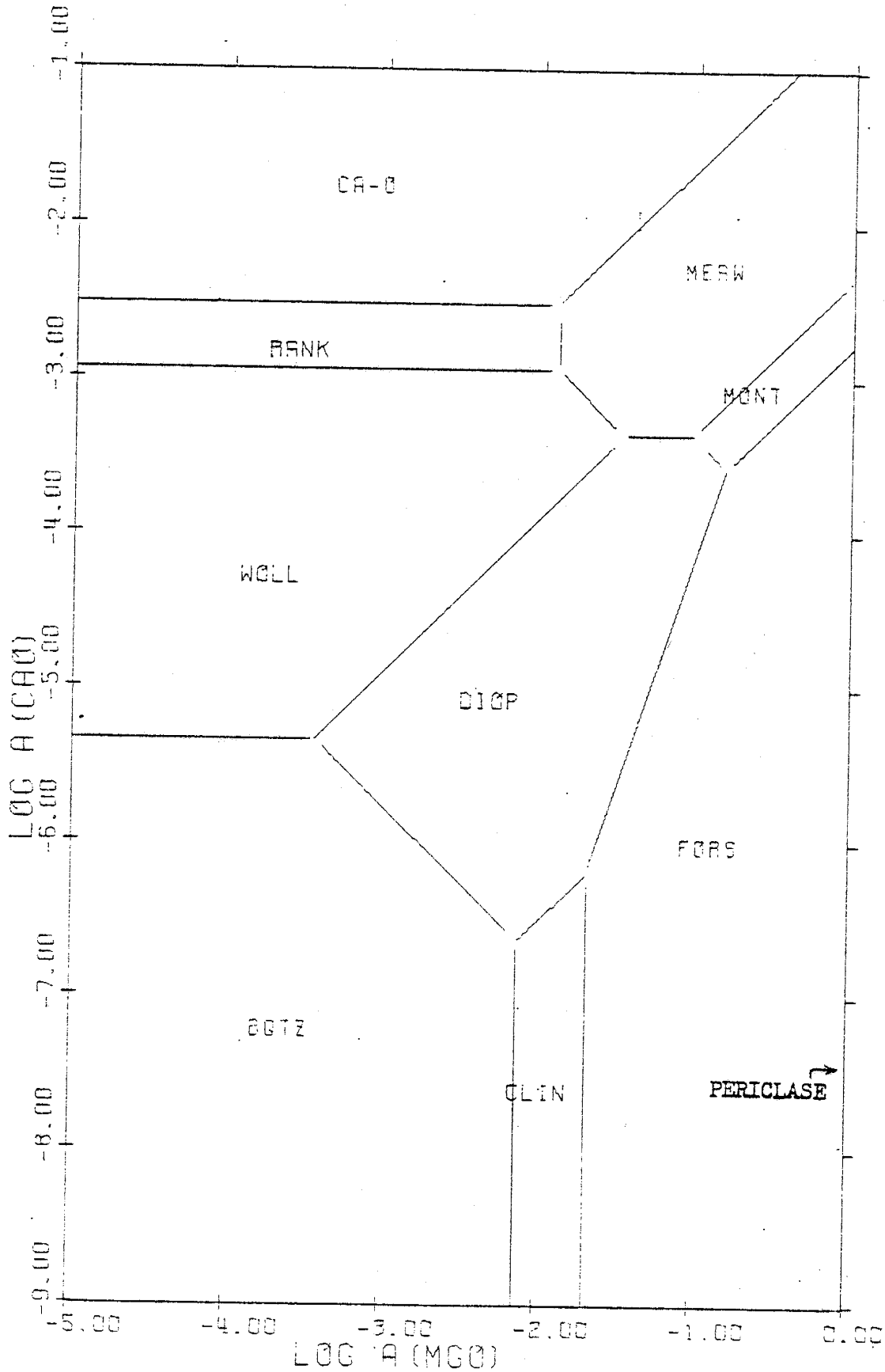
CA-O
MERW
RANK
MONT
WOLL
DIOP
FORS
OGTZ
CLIN
PERICLASE
LOG A(CAO)
LOG A(MGO)
-1.00
-2.00
-3.00
-4.00
-5.00
-6.00
-7.00
-8.00
-9.00
-5.00
-4.00
-3.00
-2.00
-1.00
0.00

Figure 33. Activity diagram for the system CaO-MgO-SiO_2 (excluding rankinite) at 600°C and 1000 bars.

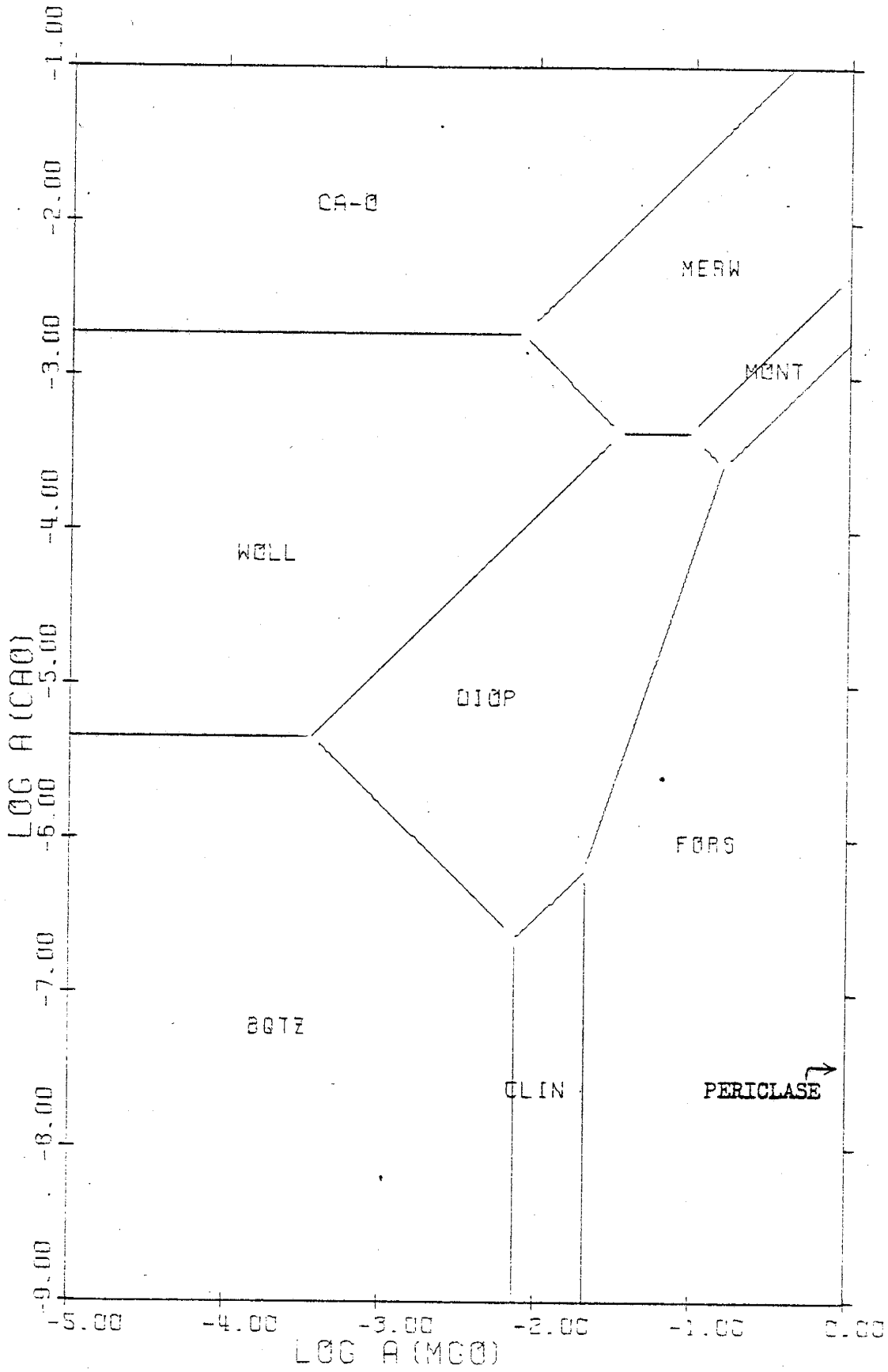
CA-O
MERW
MONT
WOLL
DIOP
FORS
ORTZ
CLIN
PERICLASE
LOG A(CAO)
LOG A(MGO)
-1.00
-2.00
-3.00
-4.00
-5.00
-6.00
-7.00
-8.00
-9.00
-5.00
-4.00
-3.00
-2.00
-1.00
0.00

diagrams. Rankinite, owing to its intermediate Ca:Si ratio with respect to wollastonite and Ca-olivine, would normally occupy a stability field between these two minerals. However, upon its omission in the 600°C, 1000 bar diagram, the stability fields of wollastonite and Ca-olivine simply expand and converge to form a new wollastonite-Ca-olivine stability field boundary.

Figures 34a,b to 50 represent the addition of pure H_2O to the anhydrous CaO-MgO-SiO_2 system in hopes of illustrating the effect of a fluid phase upon mineral stabilities. The fugacities of H_2O at all temperatures and pressures were taken from the work of Helgeson and Kirkham (1974). It is immediately apparent from Figures 34a,b to 37 that the presence of H_2O tends to stabilize hydrous phases such as serpentine, talc and tremolite at the expense of forsterite and clinoenstatite at low temperatures (100°-400°C). However, as temperature increases at a constant pressure (Figures 34a,b to 38), the stability fields of these hydrous minerals tend to steadily decrease in size and become replaced by forsterite and clinoenstatite. This is not unexpected because these minerals are known to undergo dehydration and convert to the anhydrous phases which are seen to encroach upon their stability fields as temperature increases. Saturation lines in this series of diagrams also illustrate the dehydration of brucite to periclase. That is, at a specified temperature and pressure, the stability of brucite as opposed to that of periclase is indicated by the positioning of their saturation lines. For example, at 1 bar, the saturation line of brucite lies at lower values of log $a_{Mg^{++}}/(a_{H^+})^2$ than that of periclase at temperatures up to and including 300°C. However, at 400°C, the periclase saturation line represents the upper limit on solution composition rather than the saturation line of brucite. In this manner, the dehydration of

Figure 34a. Activity diagram for the system $CaO-MgO-SiO_2-H_2O$ at 100°C, 1 bar and log f_{H_2O} = -0.007 (fugacities of H_2O in this and all following diagrams are from Helgeson, 1974).

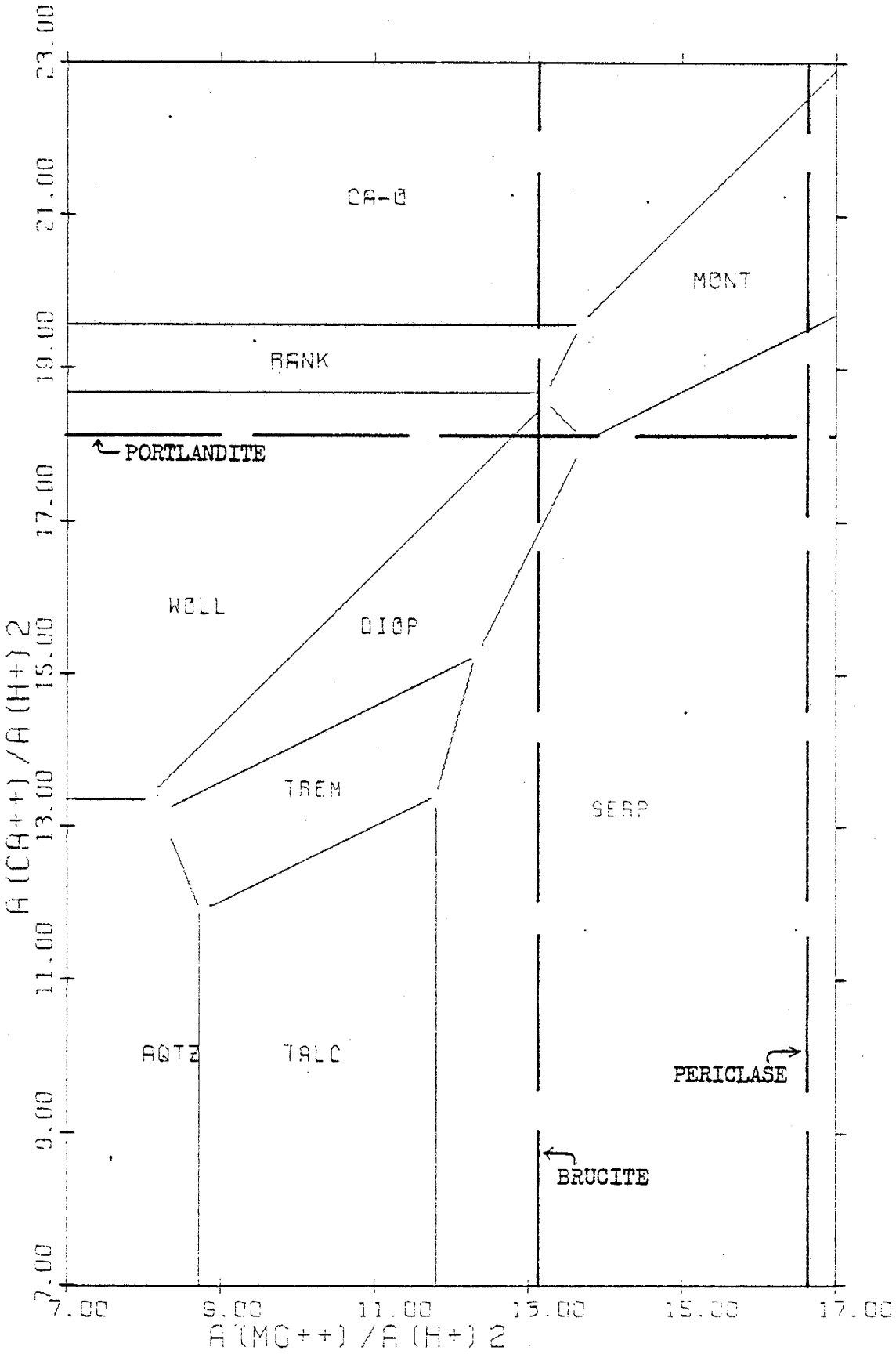
CA-O
MONT
BANK
PORTLANDITE
WOLL
DIOP
TREM
SERP
AQTZ
TALC
PERICLASE
BRUCITE
A (CA++) /A (H+) 2
A (MG++) /A (H+) 2
23.00
21.00
19.00
17.00
15.00
13.00
11.00
9.00
7.00
7.00
9.00
11.00
13.00
15.00
17.00

Figure 34b. Activity diagram for the system $CaO-MgO-SiO_2-H_2O$ at 100°C, 1 bar and log f_{H_2O} = -0.007.

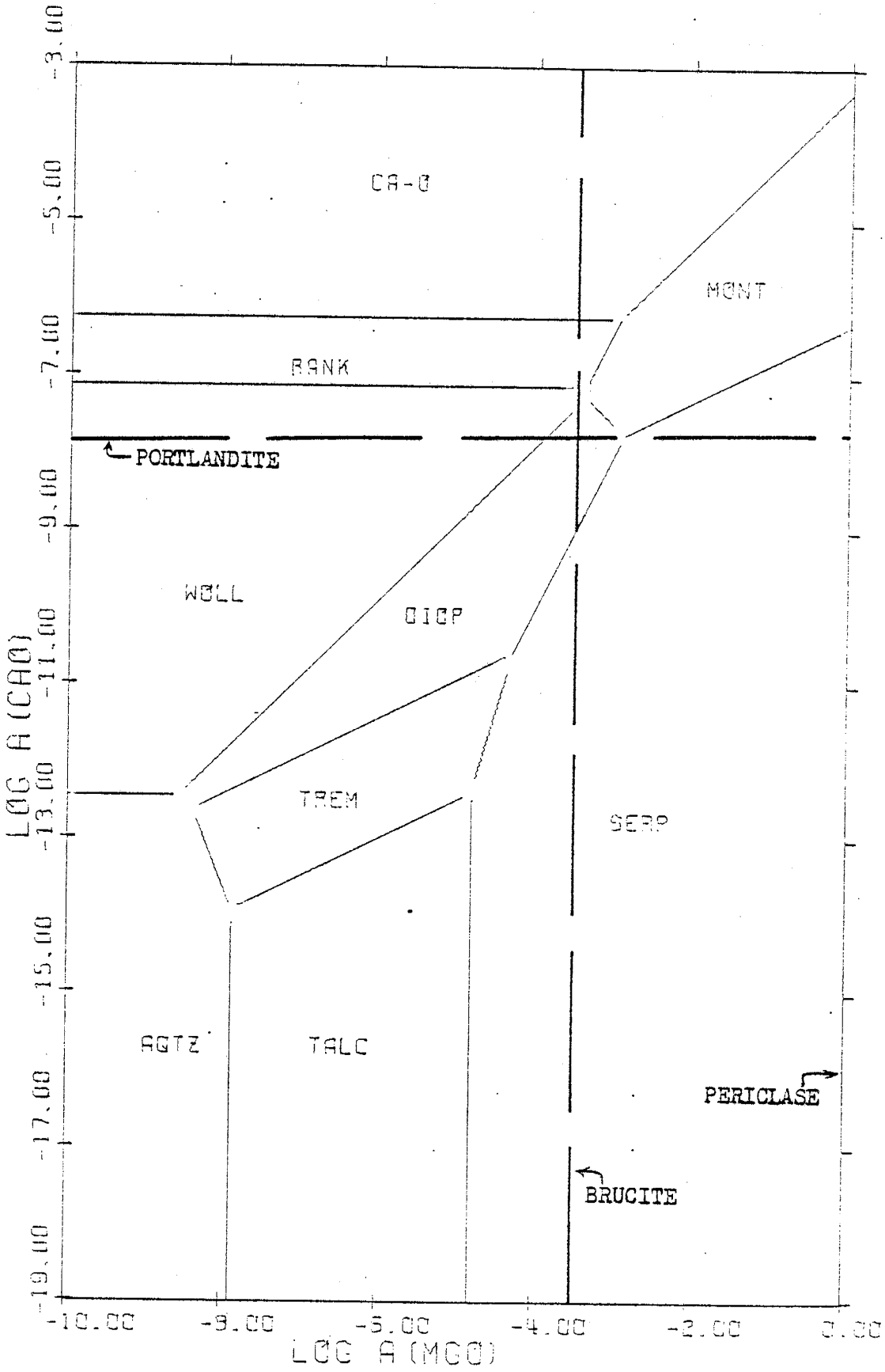
CA-C
MONT
BANK
PORTLANDITE
WOLL
DIOP
TREM
SERP
AGTZ
TALC
PERICLASE
BRUCITE
LOG A (CAO)
LOG A (MGO)
-3.00
-5.00
-7.00
-9.00
-11.00
-13.00
-15.00
-17.00
-19.00
-10.00
-8.00
-6.00
-4.00
-2.00
0.00

Figure 35. Activity diagram for the system $CaO-MgO-SiO_2-H_2O$ at 200°C, 1 bar and log f_{H_2O} = -0.002.

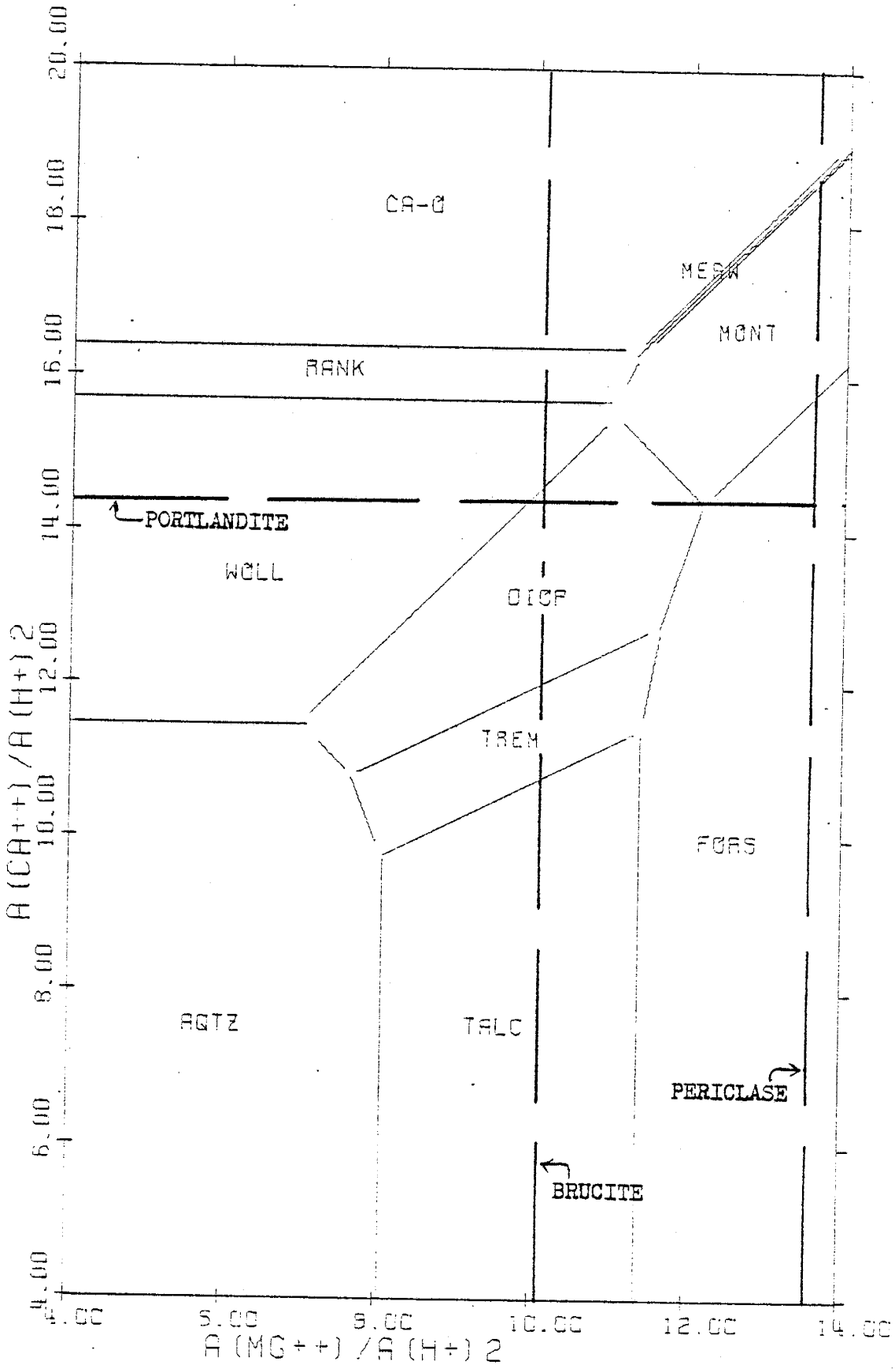
20.00
18.00
16.00
14.00
12.00
10.00
8.00
6.00
4.00
A(CA++)/A(H+)2
CA-G
MES-W
MONT
RANK
PORTLANDITE
WOLL
DICP
TREM
FORS
AGTZ
TALC
PERICLASE
BRUCITE
4.00
5.00
9.00
10.00
12.00
14.00
A(MG++)/A(H+)2

Figure 36. Activity diagram for the system CaO-MgO-SiO_2-H_2O at 300°C, 1 bar and log f_{H_2O} = -0.001.

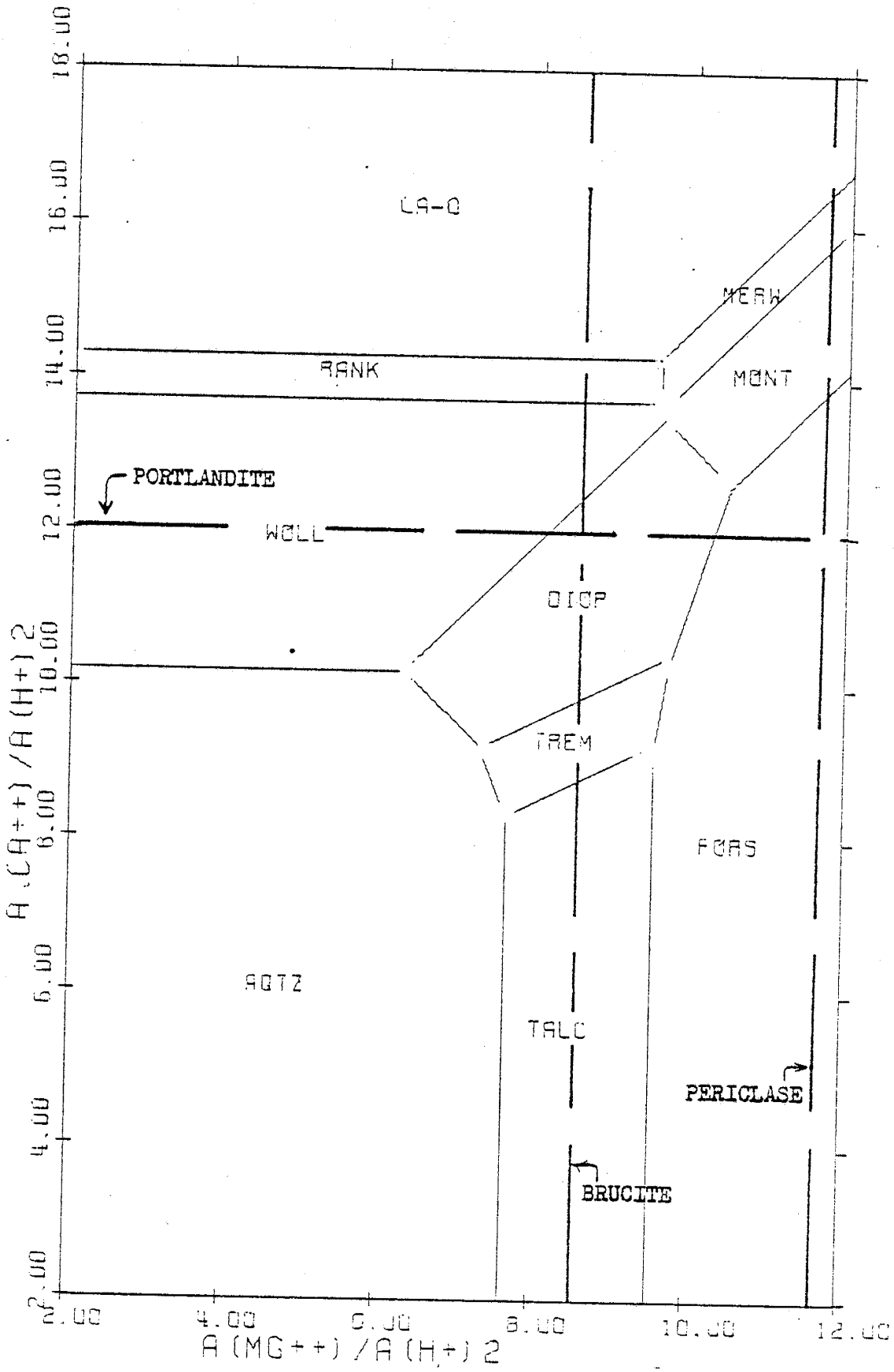
LA-Q
MERW
RANK
MONT
PORTLANDITE
WOLL
DIOP
TREM
FORS
AGTZ
TALC
PERICLASE
BRUCITE
A (CA++) /A (H+) 2
A (MG++) /A (H+) 2
16.00
14.00
12.00
10.00
8.00
6.00
4.00
2.00
2.00
4.00
6.00
8.00
10.00
12.00

Figure 37. Activity diagram for the system $CaO-MgO-SiO_2-H_2O$ at 400°C, 1 bar and log f_{H_2O} = 0.0.

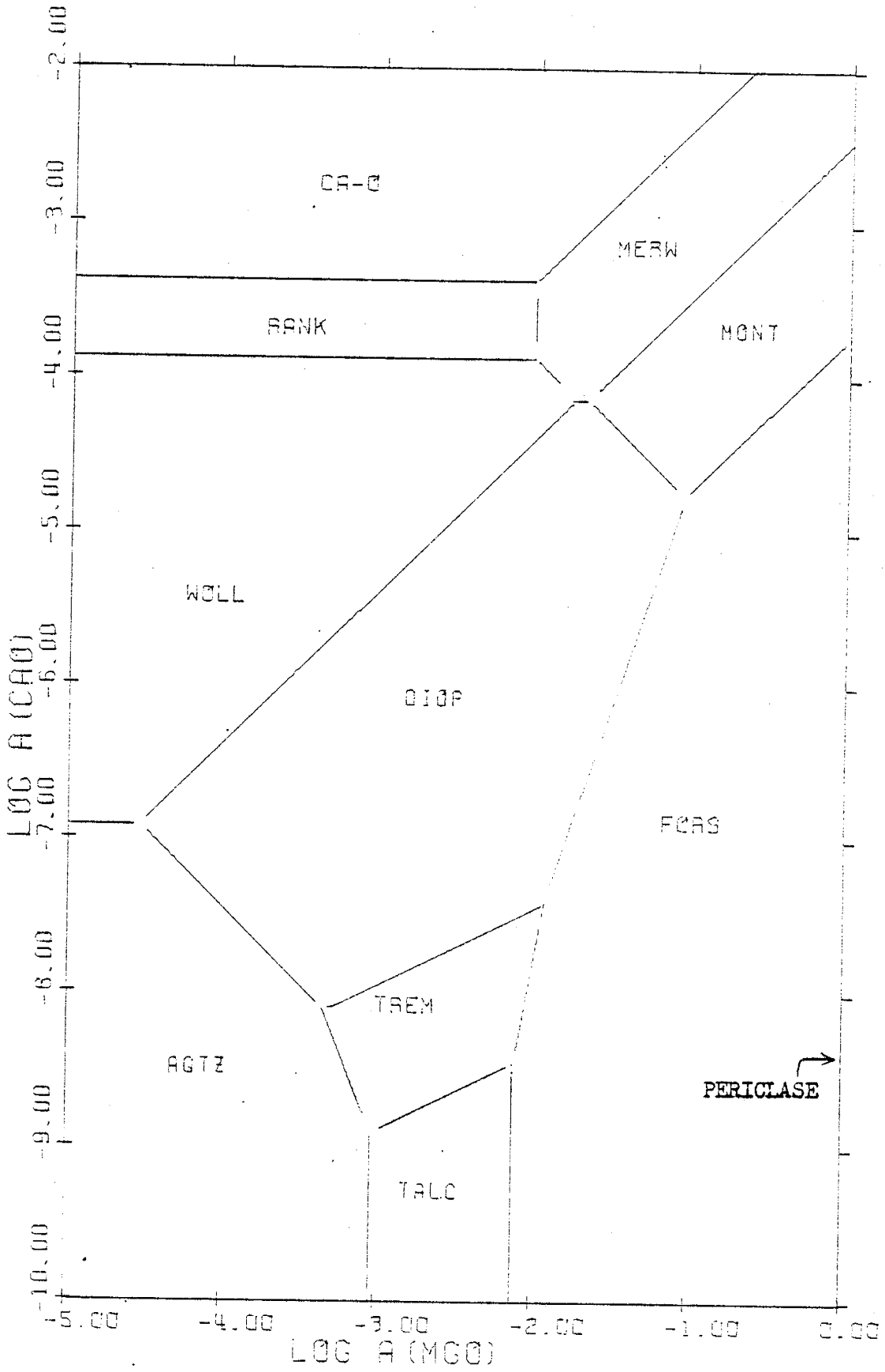
CA-C
MERW
RANK
MONT
WOLL
DIOP
FORS
TREM
AGTZ
TALC
PERICLASE
-2.00
-3.00
-4.00
-5.00
-6.00
-7.00
-8.00
-9.00
-10.00
LOG A(CAO)
-5.00
-4.00
-3.00
-2.00
-1.00
0.00
LOG A(MGO)

Figure 38. Activity diagram for the system $CaO-MgO-SiO_2-H_2O$ at 600°C, 1 bar and log f_{H_2O} = 0.0.

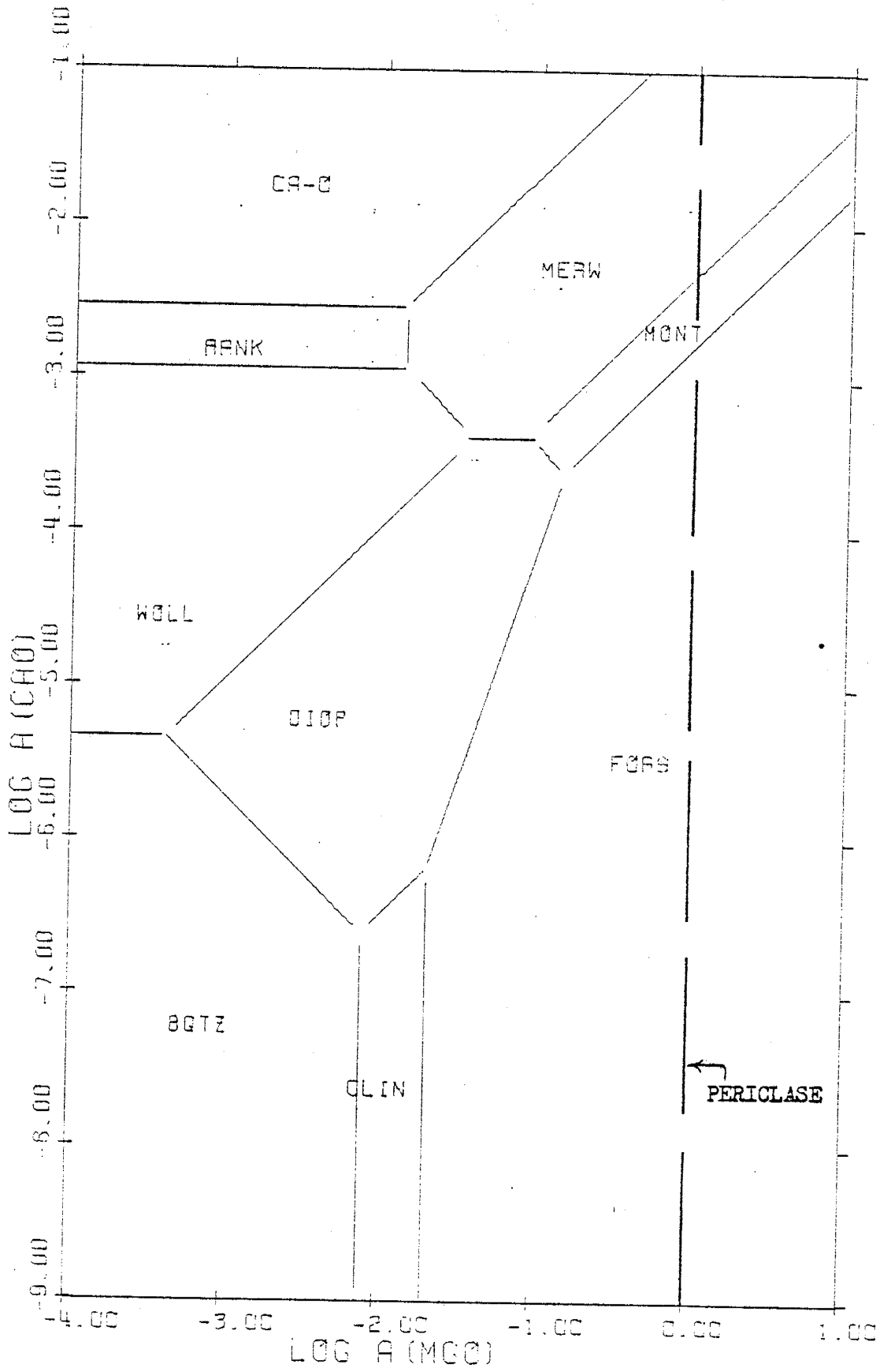
CA-C
MERW
MONT
ARAK
WOLL
DIOP
FORS
BGTZ
CLIN
PERICLASE
LOG A(CAO)
LOG A(MGO)
-1.00
-2.00
-3.00
-4.00
-5.00
-6.00
-7.00
-8.00
-9.00
-4.00
-3.00
-2.00
-1.00
0.00
1.00

Figure 39. Activity diagram for the system $CaO-MgO-SiO_2-H_2O$ at 100°C, 500 bars and log f_{H_2O} = 0.128.

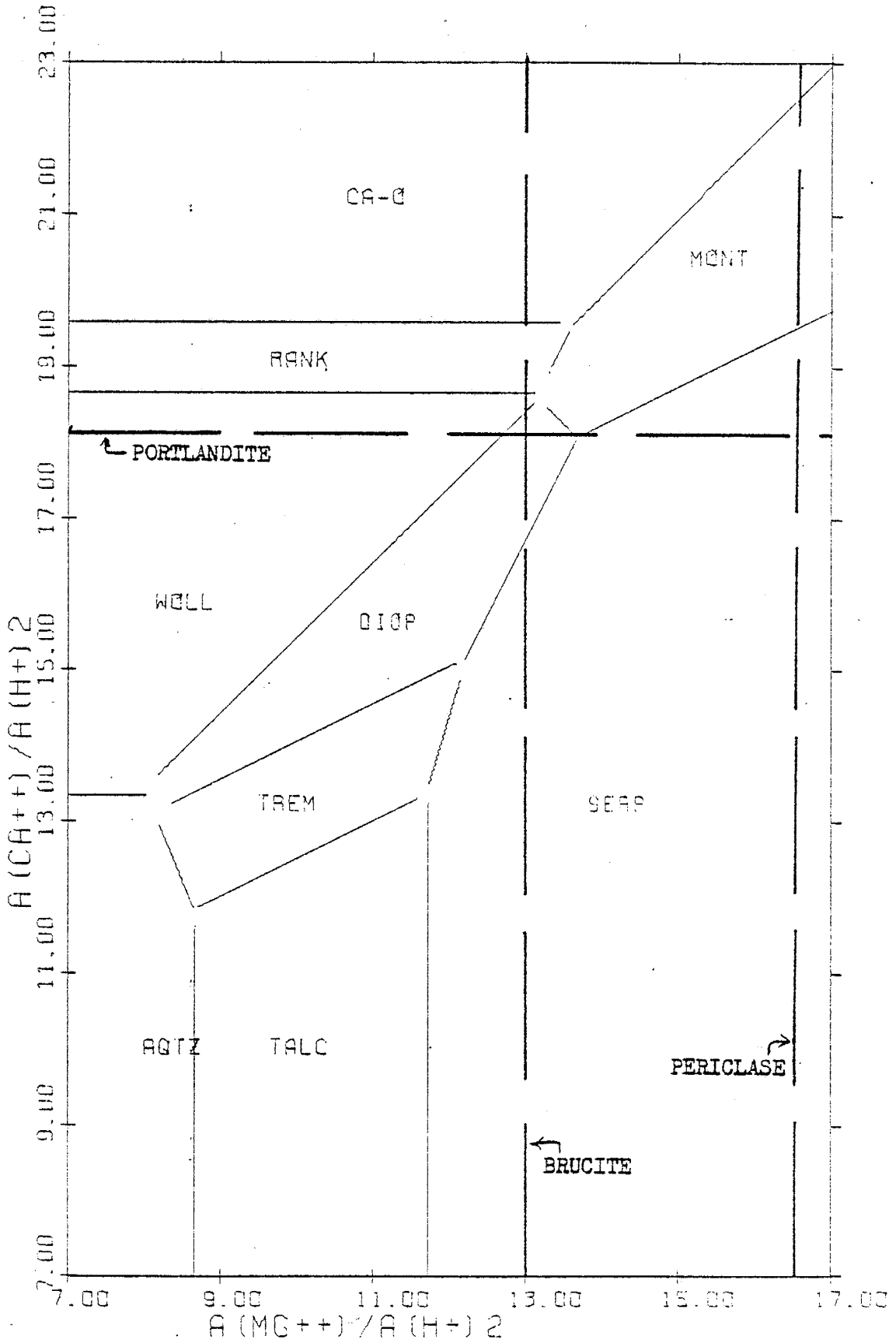
CA-C
MONT
RANK
PORTLANDITE
WOLL
DIOP
TREM
SERP
QTZ
TALC
PERICLASE
BRUCITE
A (CA++) / A (H+) 2
A (MG++) / A (H+) 2
23.00
21.00
19.00
17.00
15.00
13.00
11.00
9.00
7.00
7.00
9.00
11.00
13.00
15.00
17.00

Figure 40. Activity diagram for the system $CaO-MgO-SiO_2-H_2O$ at 200°C, 500 bars and log f_{H_2O} = 1.263.

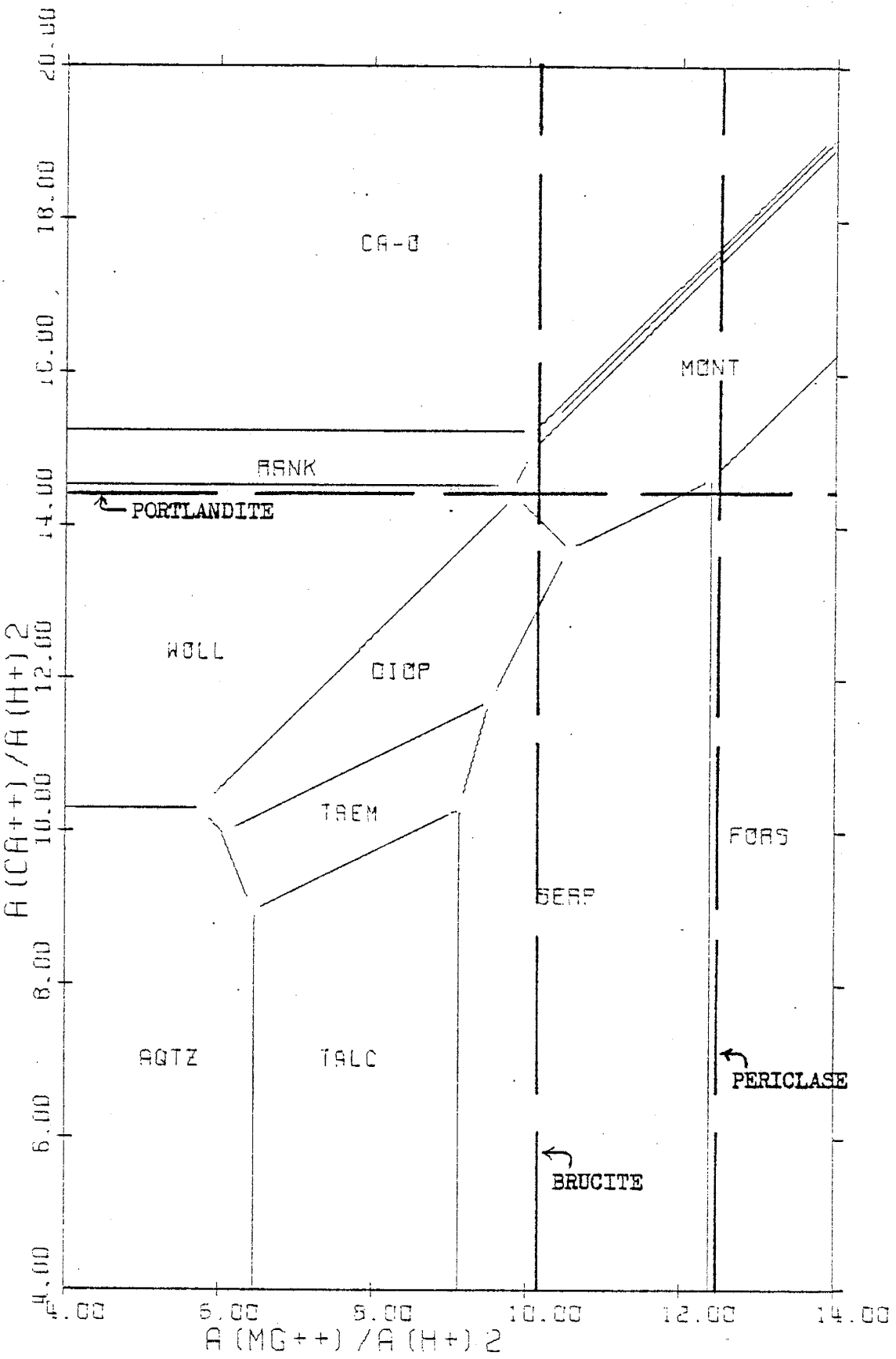
CA-O
MONT
BRNK
PORTLANDITE
WOLL
DIOP
TREM
FORS
SERP
AQTZ
TALC
PERICLASE
BRUCITE
A(CA++)/A(H+)2
A(MG++)/A(H+)2
20.00
18.00
16.00
14.00
12.00
10.00
8.00
6.00
4.00
4.00
6.00
8.00
10.00
12.00
14.00

Figure 41. Activity diagram for the system $CaO-MgO-SiO_2-H_2O$ at 300°C, 500 bars and log f_{H_2O} = 1.919.

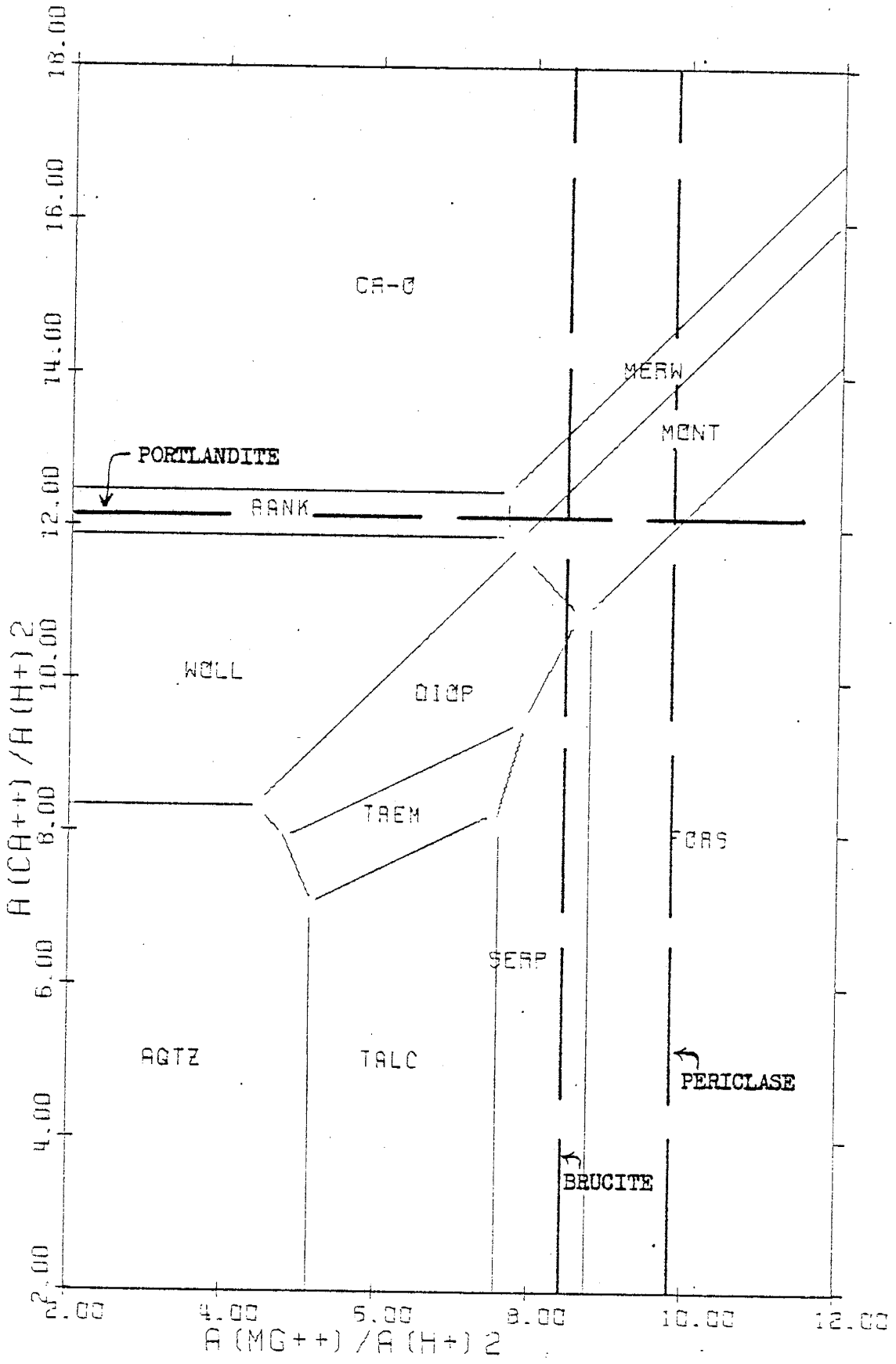
CA-O
MERW
MONT
PORTLANDITE
BANK
WOLL
DIOP
TREM
FORS
SERP
AGTZ
TALC
PERICLASE
BRUCITE
A (CA++) /A (H+) 2
A (MG++) /A (H+) 2
18.00
16.00
14.00
12.00
10.00
8.00
6.00
4.00
2.00
2.00
4.00
5.00
8.00
10.00
12.00

Figure 42. Activity diagram for the system $CaO-MgO-SiO_2-H_2O$ at 400°C, 500 bars and log f_{H_2O} = 2.31.

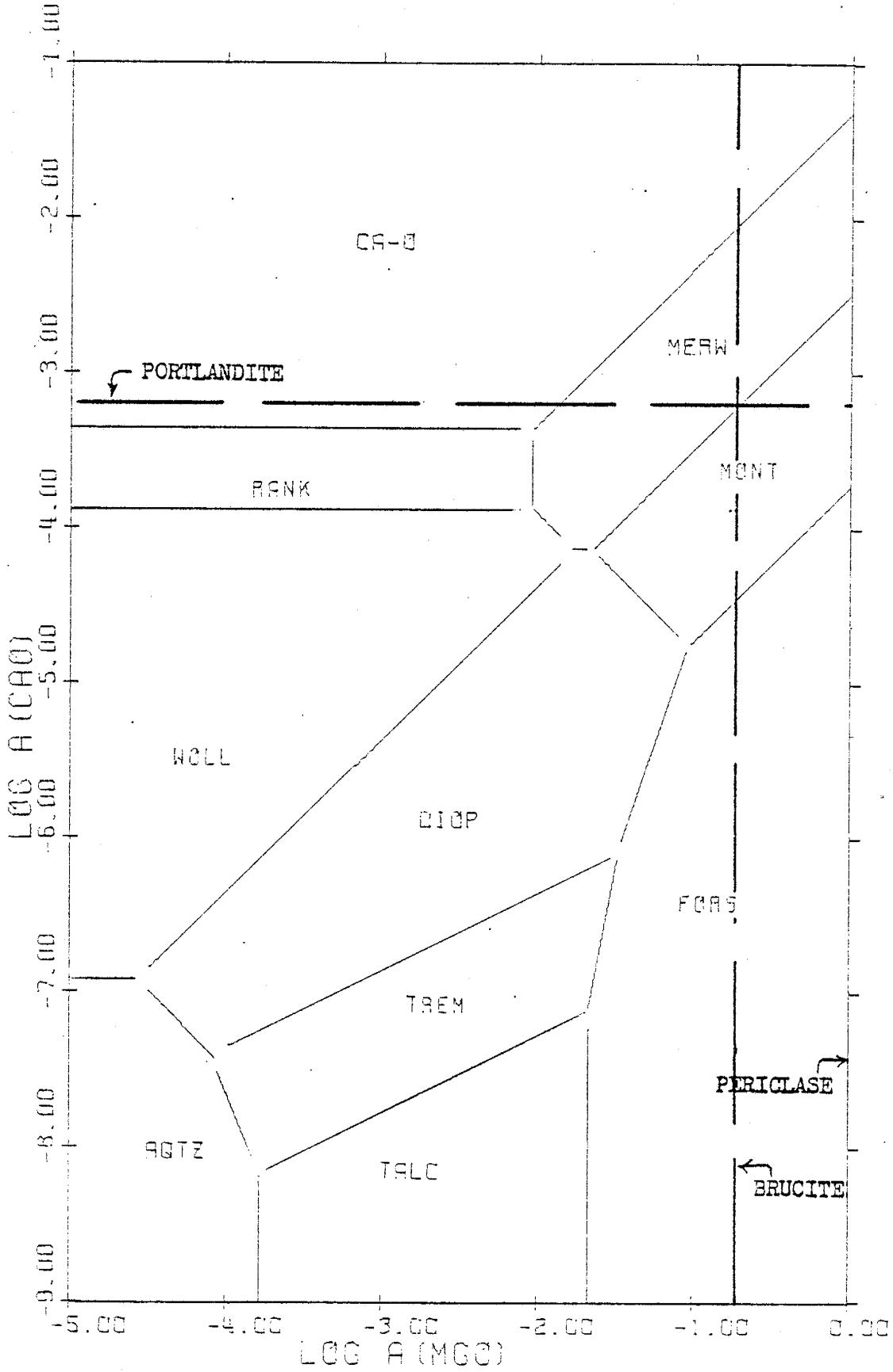
-1.00
-2.00
-3.00
-4.00
-5.00
-6.00
-7.00
-8.00
-9.00
LOG A(CAO)
CA-O
PORTLANDITE
MERW
MONT
RANK
WOLL
DIOP
FORS
TREM
PERICLASE
AGTZ
TALC
BRUCITE
-5.00
-4.00
-3.00
-2.00
-1.00
0.00
LOG A(MGO)

Figure 43. Activity diagram for the system $CaO-MgO-SiO_2-H_2O$ at 600°C, 500 bars and log f_{H_2O} = 2.59.

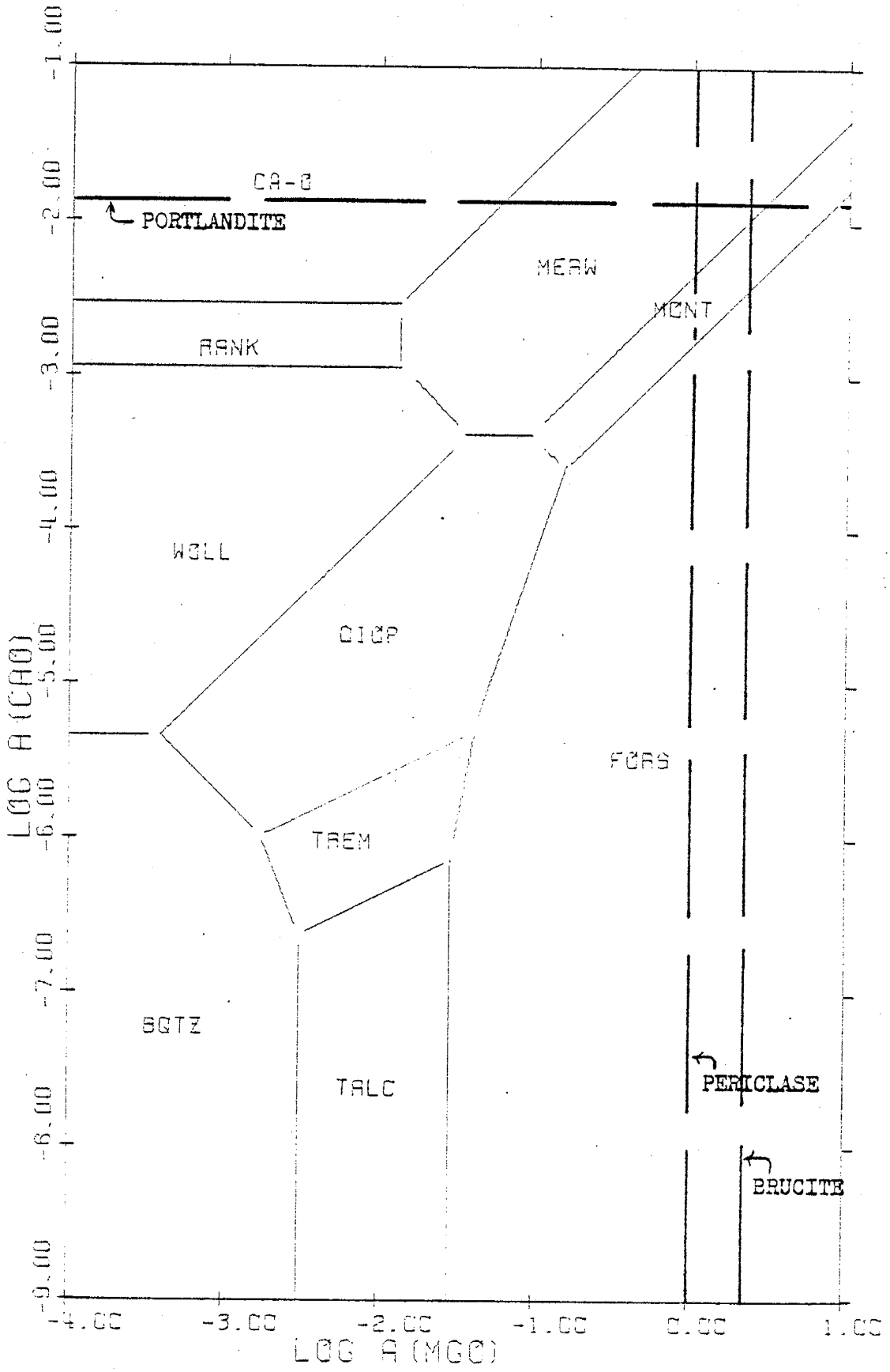
-1.00
-2.00
-3.00
-4.00
-5.00
-6.00
-7.00
-8.00
-9.00
LOG A(CAO)
-4.00
-3.00
-2.00
-1.00
0.00
1.00
LOG A(MGO)
CA-C
PORTLANDITE
MEAW
MCNT
RANK
WOLL
DICP
FORS
TREM
BGTZ
TALC
PERICLASE
BRUCITE

Figure 44. Activity diagram for the system $CaO-MgO-SiO_2-H_2O$ at 800°C, 500 bars and log f_{H_2O} = 2.66.

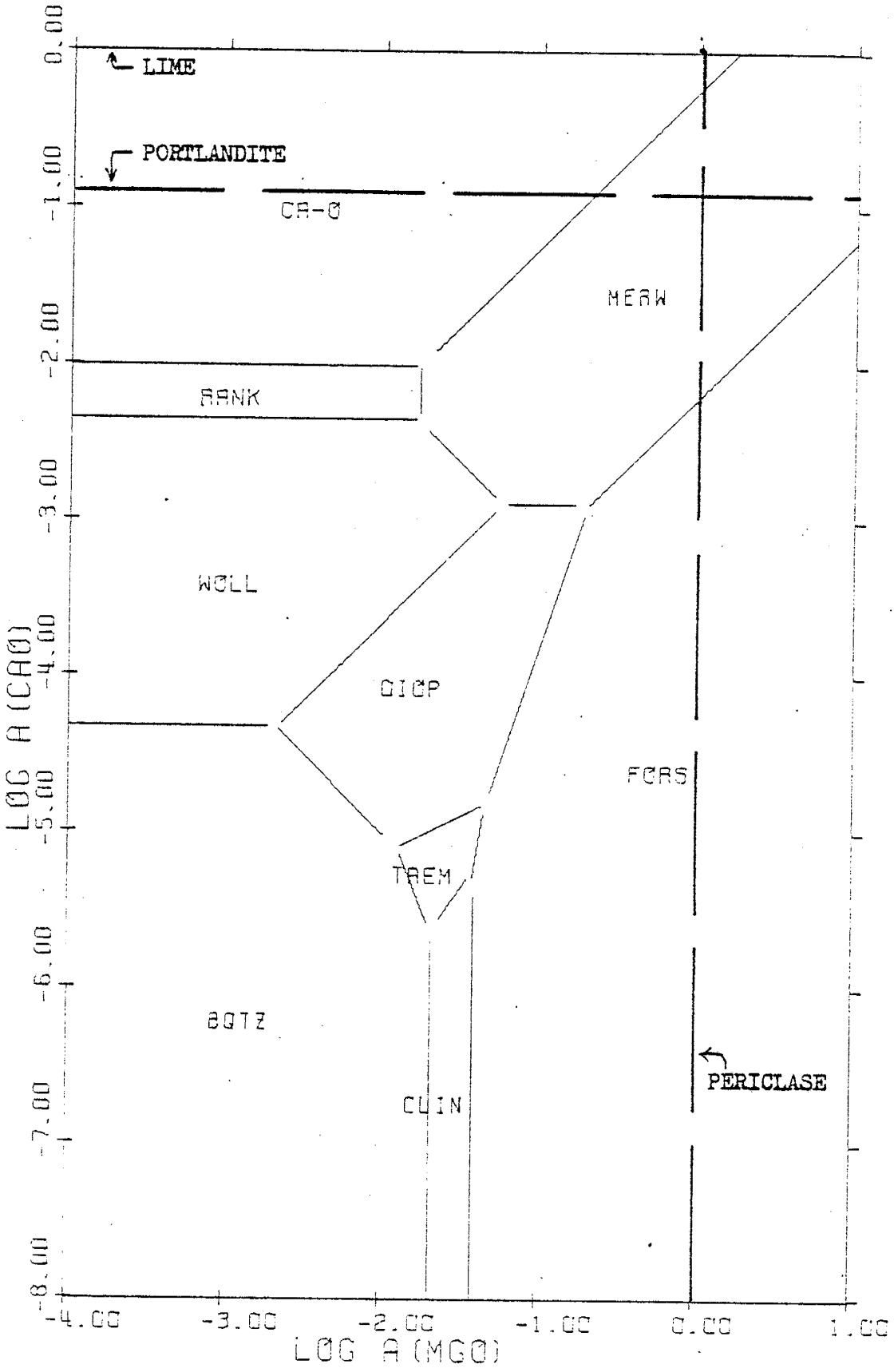
LIME
PORTLANDITE
CA-O
MERW
RANK
WOLL
DIOP
FORS
TREM
BOTZ
CLIN
PERICLASE
LOG A(CAO)
LOG A(MGO)
0.00
-1.00
-2.00
-3.00
-4.00
-5.00
-6.00
-7.00
-8.00
-4.00
-3.00
-2.00
-1.00
0.00
1.00

Figure 45a. Activity diagram for the system $CaO-MgO-SiO_2-H_2O$ at 100°C, 1000 bars and log f_{H_2O} = 0.256.

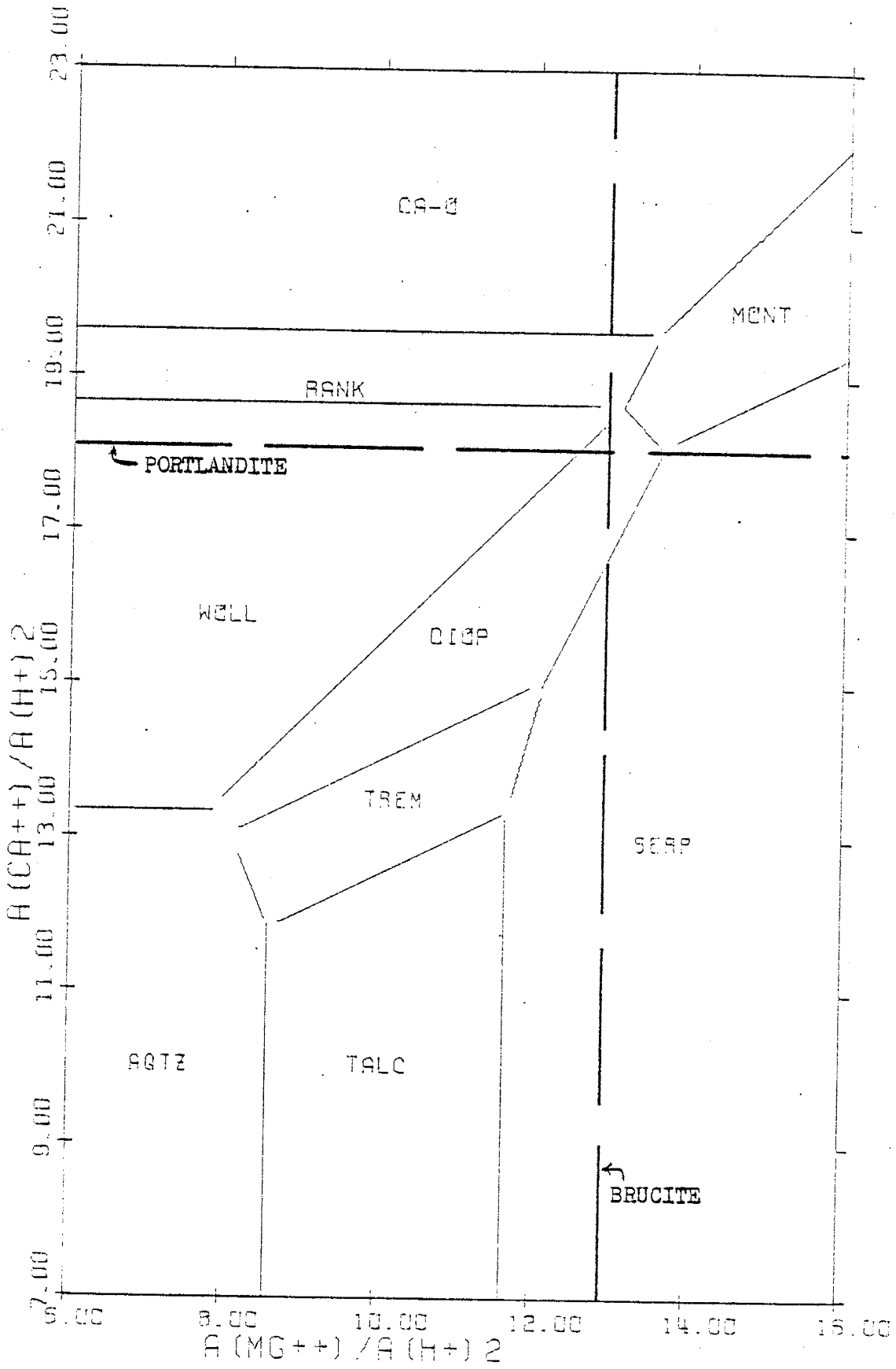
CA-O
MONT
BANK
PORTLANDITE
WOLL
DIOP
TREM
SERP
QTZ
TALC
BRUCITE
A (CA++) /A (H+) 2
A (MG++) /A (H+) 2
23.00
21.00
19.00
17.00
15.00
13.00
11.00
9.00
7.00
6.00
8.00
10.00
12.00
14.00
16.00

Figure 45b. Activity diagram for the system $CaO-MgO-SiO_2-H_2O$ at 100°C, 1000 bars and log f_{H_2O} = 0.256.

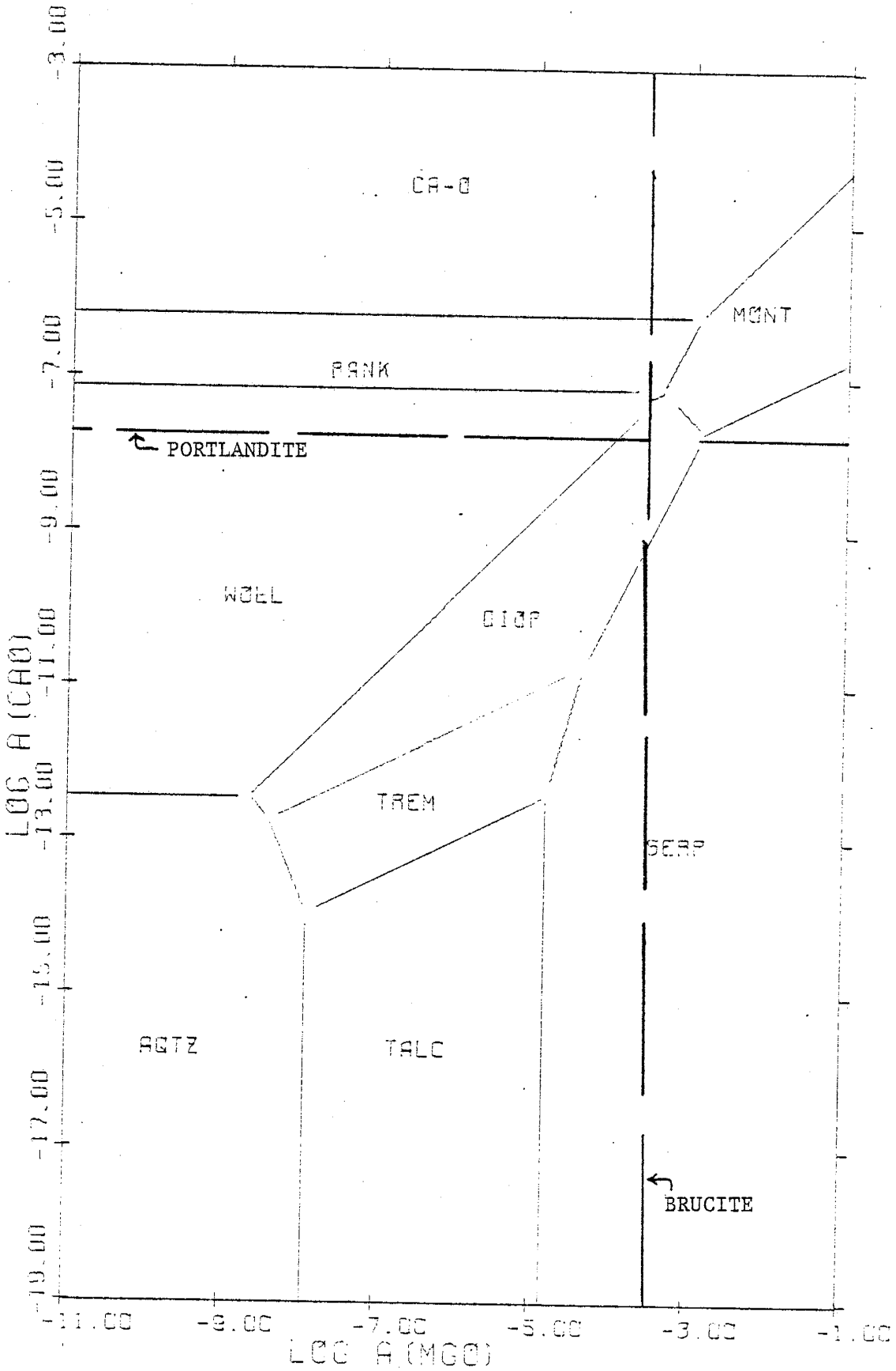
CA-O
MONT
PANK
PORTLANDITE
WOLL
DIOP
TREM
SERP
AGTZ
TALC
BRUCITE
LOG A(CAO)
LOG A(MGO)
-3.00
-5.00
-7.00
-9.00
-11.00
-13.00
-15.00
-17.00
-19.00
-11.00
-9.00
-7.00
-5.00
-3.00
-1.00

Figure 46. Activity diagram for the system $CaO-MgO-SiO_2-H_2O$ at 200°C, 1000 bars and log f_{H_2O} = 1.372.

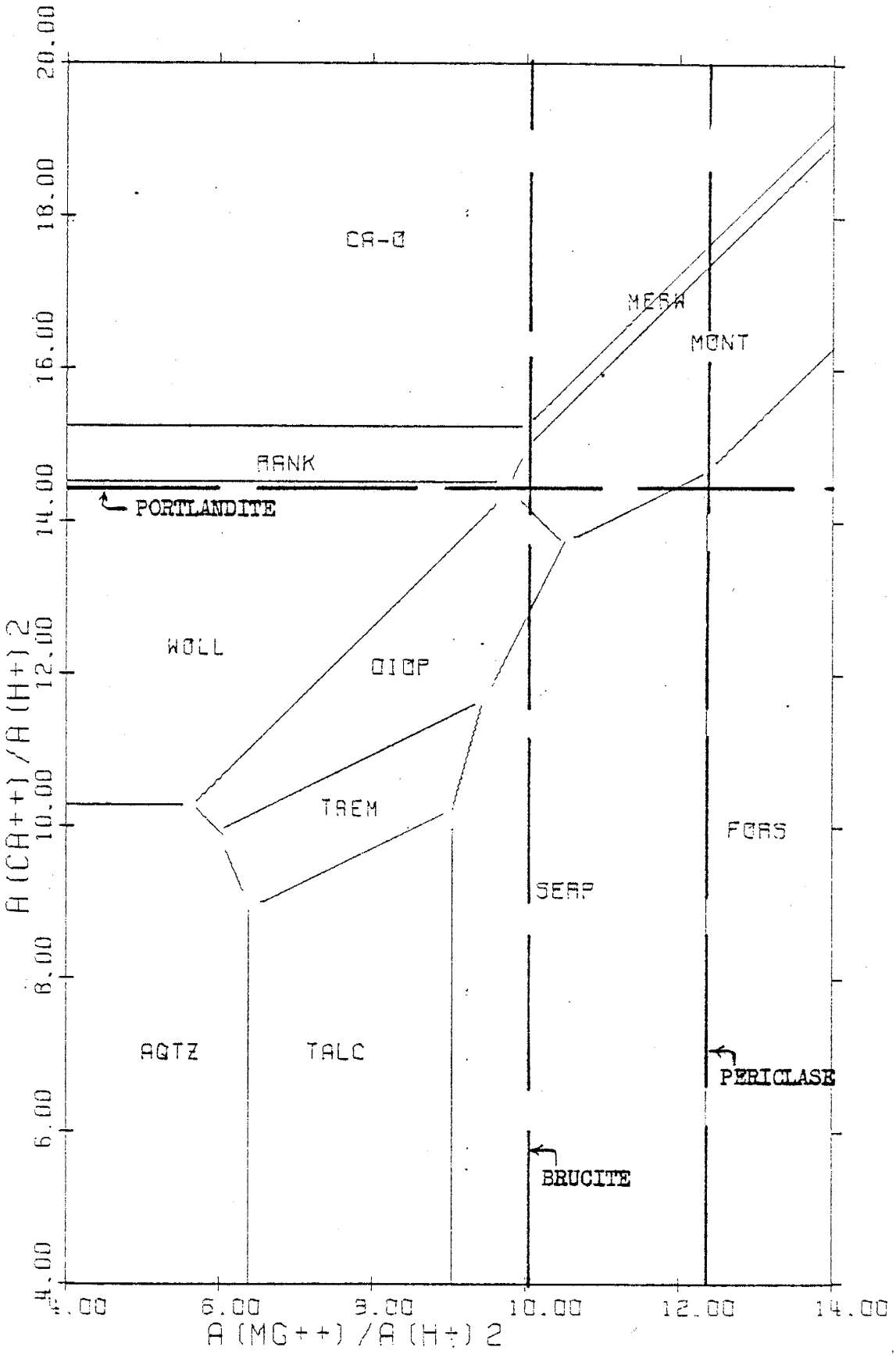
CA-O
MERW
MONT
BANK
PORTLANDITE
WOLL
DIOP
TREM
FORS
SERP
AQTZ
TALC
PERICLASE
BRUCITE
A (CA++) /A (H+) 2
A (MG++) /A (H+) 2
20.00
18.00
16.00
14.00
12.00
10.00
8.00
6.00
4.00
4.00
6.00
8.00
10.00
12.00
14.00

Figure 47. Activity diagram for the system $CaO-MgO-SiO_2-H_2O$ at 300°C, 1000 bars and log f_{H_2O} = 2.021.

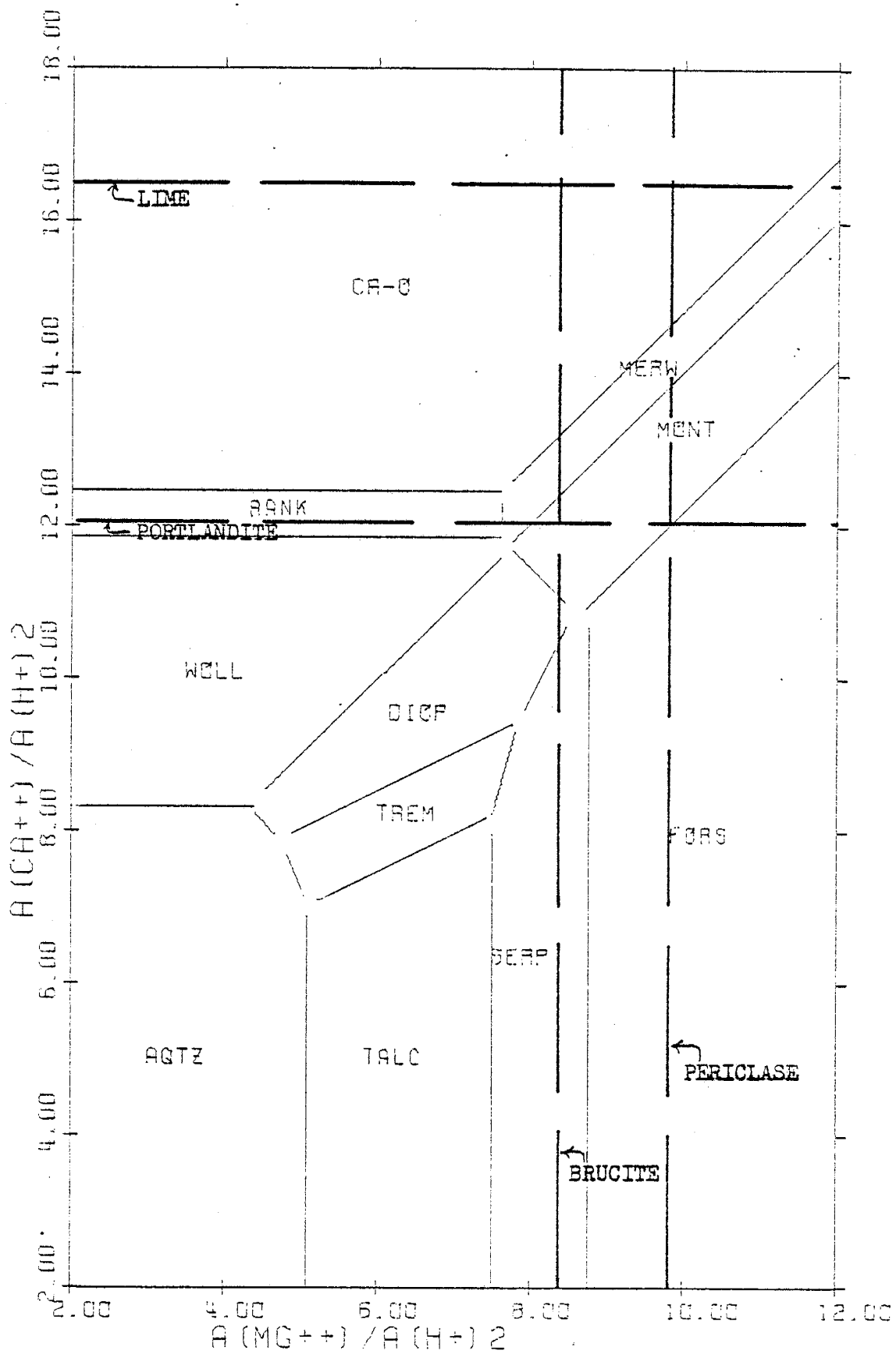
LIME
CA-O
MERW
MENT
BANK
PORTLANDITE
WOLL
DICP
TREM
FORS
SERP
AGTZ
TALC
PERICLASE
BRUCITE
16.00
14.00
12.00
10.00
8.00
6.00
4.00
2.00
2.00
4.00
6.00
8.00
10.00
12.00
A (CA++) /A (H+) 2
A (MG++) /A (H+) 2

Figure 48. Activity diagram for the system $CaO-MgO-SiO_2-H_2O$ at 400°C, 1000 bars and log f_{H_2O} = 2.419.

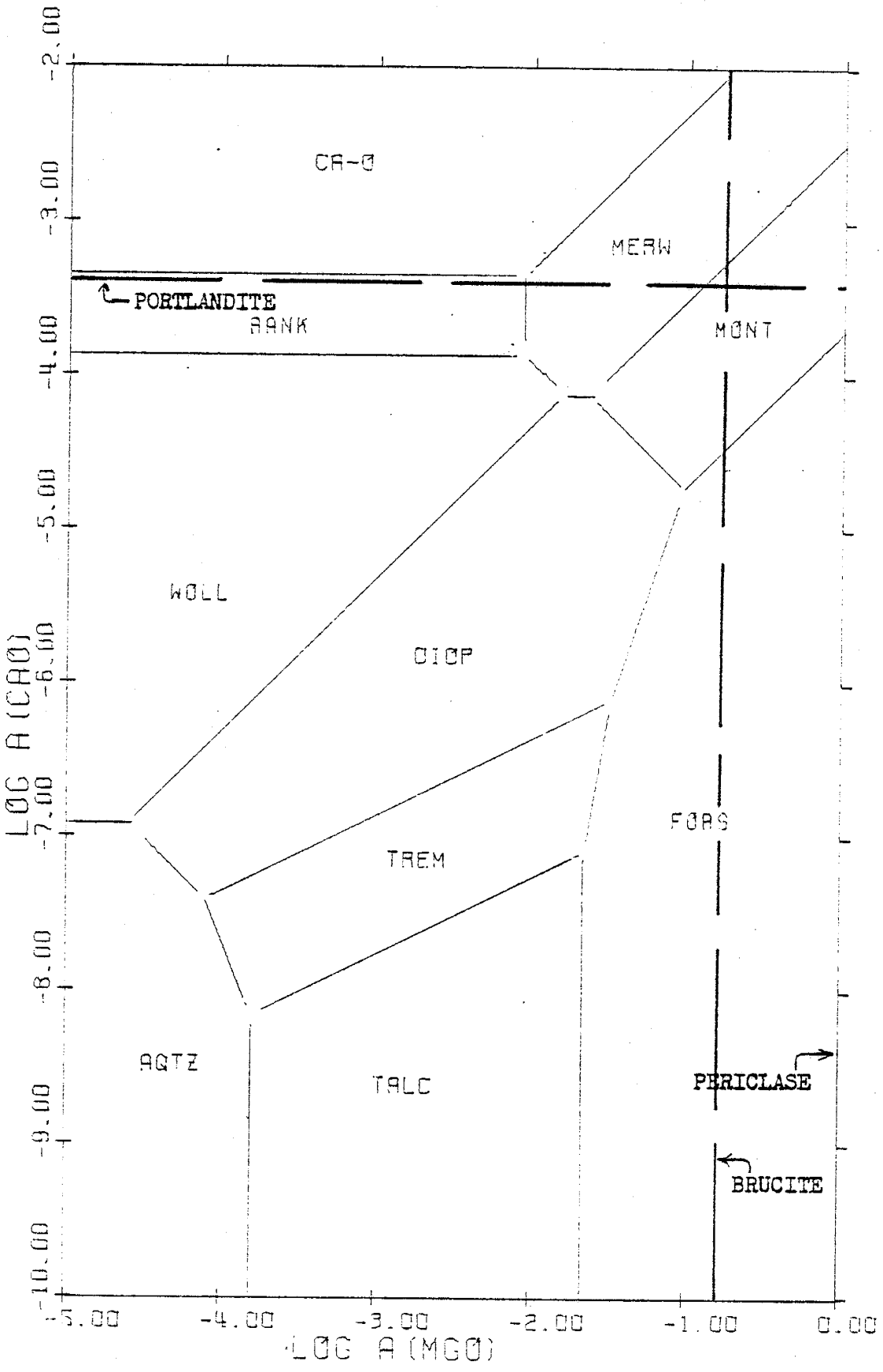
CA-O
MERW
PORTLANDITE
BANK
MONT
WOLL
DIOP
FORS
TREM
QTZ
TALC
PERICLASE
BRUCITE
LOG A(CAO)
LOG A(MGO)
-2.00
-3.00
-4.00
-5.00
-6.00
-7.00
-8.00
-9.00
-10.00
-5.00
-4.00
-3.00
-2.00
-1.00
0.00

Figure 49. Activity diagram for the system CaO-MgO-SiO_2-H_2O at 600°C, 1000 bars and log f_{H_2O} = 2.80.

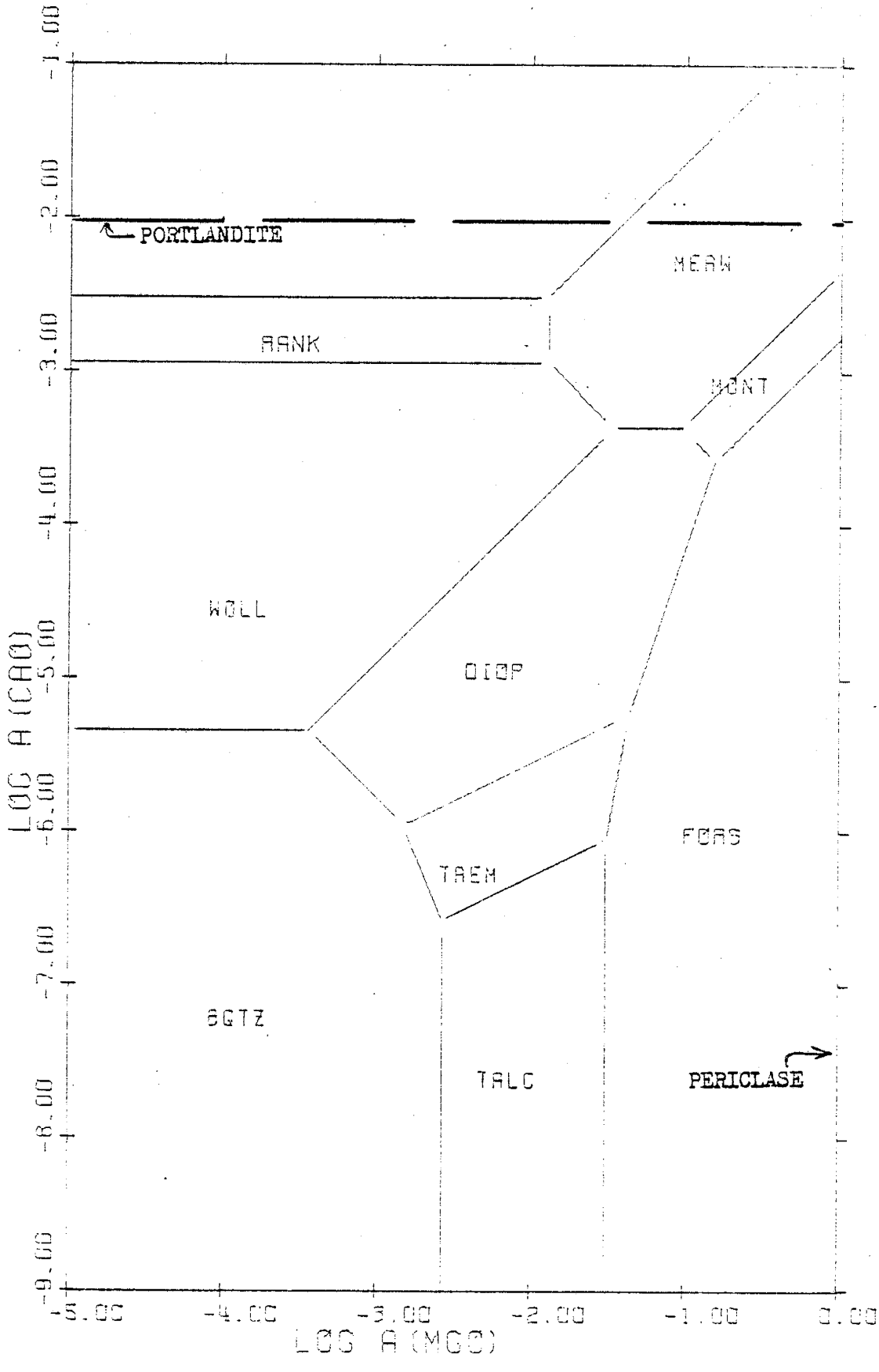
PORTLANDITE
MEAW
RANK
MONT
WOLL
DIOP
FORS
TAEM
BGTZ
TALC
PERICLASE
LOG A(CAO)
LOG A(MGO)
-1.00
-2.00
-3.00
-4.00
-5.00
-6.00
-7.00
-8.00
-9.00
-5.00
-4.00
-3.00
-2.00
-1.00
0.00

Figure 50. Activity diagram for the system $CaO-MgO-SiO_2-H_2O$ at 800°C, 1000 bars and log f_{H_2O} = 2.93.

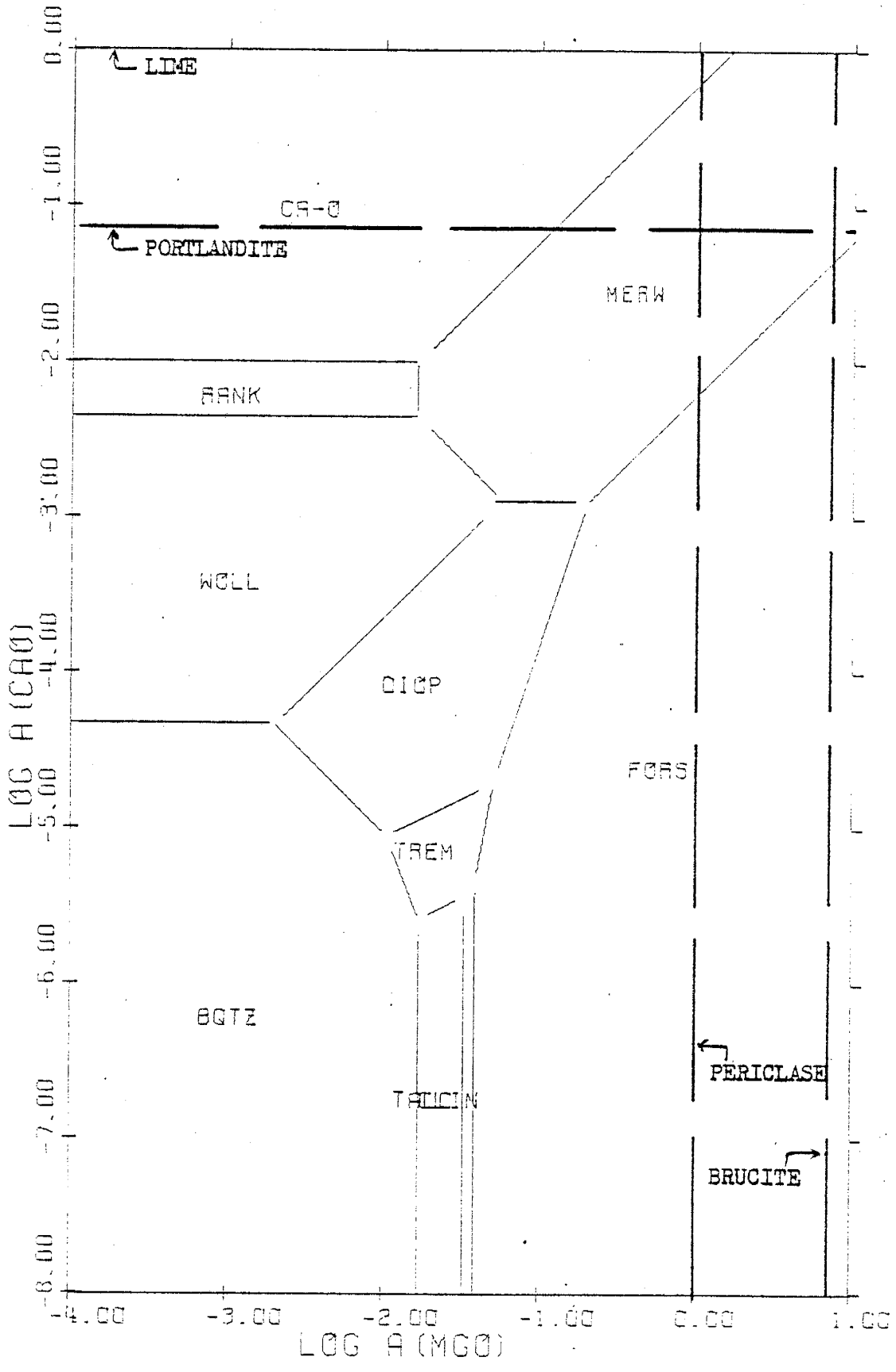
LIME
CH-C
PORTLANDITE
MEAW
RANK
WOLL
CICP
FORS
TREM
BGTZ
TAUCIN
PERICLASE
BRUCITE
0.00
-1.00
-2.00
-3.00
-4.00
-5.00
-6.00
-7.00
-8.00
-4.00
-3.00
-2.00
-1.00
0.00
1.00
LOG A(CAO)
LOG A(MGO)

brucite to periclase is shown to occur between 300° and 400°C at 1 bar. This same dehydration reaction takes place between 400° and 600°C at both 500 and 1000 bars pressure, as illustrated in Figures 42 and 43 and Figures 48 and 49. The temperature and pressure at which the brucite and periclase saturation lines actually coincide represent a point along the univariant equilibrium curve for the brucite-periclase dehydration reaction.

A close examination of these dehydration sequences at elevated pressures (500 and 1000 bars) reveals that the dehydration of the hydrous phases takes place at higher temperatures as pressure increases. Whereas serpentine becomes unstable by 200°C and talc and tremolite disappear by 600°C at 1 bar pressure (Figures 35 and 38), serpentine persists above 300°C (Figures 47 and 48) and talc and tremolite still occupy stability fields at 800°C at 1000 bars pressure (Figure 50) when clinoenstatite has just become stable, as indicated by its relatively small stability field. The brucite-periclase dehydration, as previously noted, shows a similar response to increasing pressure. This phenomenon is directly related to the commonly observed shape of dehydration curves on pressure-temperature diagrams. Figure 51 illustrates a hypothetical dehydration curve for the reaction $A \rightleftharpoons B + H_2O$ which plainly depicts the higher temperatures required to cause the dehydration of mineral A at high pressures. As previously mentioned, the slopes of curves on pressure-temperature diagrams are described by the Clapeyron equation

$$\frac{dP}{dT} = \frac{\Delta S_r}{\Delta V_r} \quad . \tag{26}$$

ΔS°_r for reactions involving a product fluid phase is often positive but its value at elevated temperatures and pressures will depend upon the heat capacity of the reaction; i.e.,

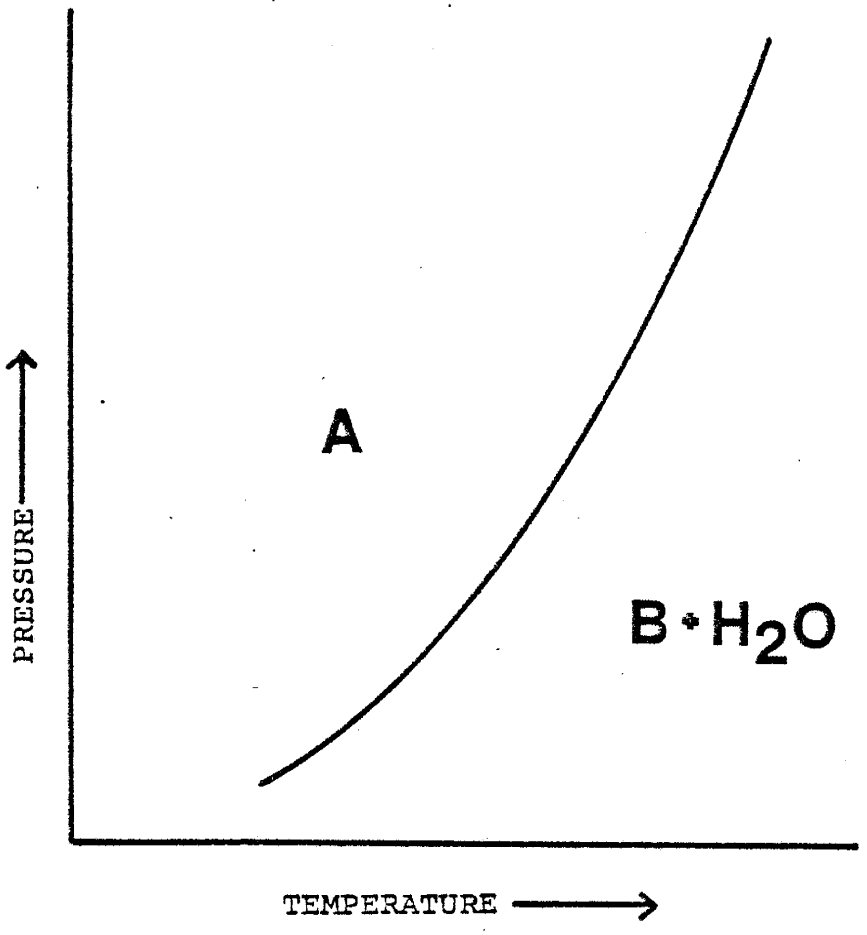

Figure 51. Hypothetical dehydration curve for the reaction A $\rightleftharpoons$ B + H_2O.

$$\Delta S_{T,r} = \Delta S^{\circ}_{298.15,r} + \int_{298.15}^{T} (\Delta Cp_r/T)dT \ . \qquad (67)$$

Heat capacities of anhydrous minerals can be roughly approximated by summing the heat capacities of their pure component oxides, and therefore the heat capacity of reaction between anhydrous phases is about zero. The heat capacity of a hydrous mineral can be estimated in a similar manner by assuming the heat capacity of H_2O in the mineral to be that of ice. In contrast, the H_2O evolved in a dehydration reaction involving hydrous minerals is considered a gas and therefore contributes the heat capacity of a gas to the total heat capacity of the reaction. However, the difference between the heat capacity of $H_2O(g)$ and $H_2O(s)$ is small enough at elevated temperatures and pressures such that, as a first approximation, the heat capacity of reaction can be roughly evaluated as zero. Consequently, the entropy change of some reaction at an elevated temperature and pressure is approximately equal to the entropy change at 25°C and 1 bar. This might be expected because the entropy of a mineral can also be estimated by the stochiometric summation of the contributions of its component oxides and the entropy of reaction would therefore depend on the difference between the entropy of H_2O as the gas evolved in the reaction and its entropy as an integral part of a mineral. Accordingly, ΔS_r will not vary greatly over pressure-temperature space and therefore the slope of the equilibrium curve is dependent on ΔV_r. Because the fluid phase appears as a product in dehydration reactions, ΔV_r will generally be positive. However, as pressure increases, the volume of H_2O will decrease and the slope of the dehydration curve will tend to become steeper, yielding the commonly observed shape of univariant dehydration curves as illustrated in Figure 51. Of course, this is an oversimplification of the problem but it does illustrate the

general relationships involved in determining the slope of pressure-temperature curves.

It should be noted that the series of diagrams in Figures 34a,b to 50 at pressures of 1, 500 and 1000 bars and temperatures from 100° to 800°C show that the mineral stability field boundaries between anhydrous minerals are relatively independent of pressure, as previously explained, and therefore diagrams at the same temperature but different pressures are generally quite similar. However, the series of diagrams at 1 bar exhibits a marked expansion of the quartz field at 200°C and 300°C relative to its size in the corresponding diagrams at 500 and 1000 bars pressure. This can be explained by the fact that at 1 bar, an increase in temperature results in the crossing of the equilibrium or boiling curve between $H_2O(l)$ and $H_2O(g)$, and H_2O undergoes a rapid volume change. At pressures exceeding that of the critical point of H_2O (220.88 bars), a temperature increase causes a gradual change in the volume of H_2O as it proceeds from a liquid to a gaseous state. Therefore, there is a distinct difference in the thermodynamic properties of the fluid phase at 1 bar compared to its properties at 500 and 1000 bars pressure at 200° and 300°C. According to the activity diagrams however, as soon as the temperature exceeds that of the critical point of H_2O (374.136°C), the fluid phase appears to have the same general properties at all pressures because the diagrams once again coincide.

It was mentioned above that activity diagrams plotting the ratios of ion activities are related to diagrams plotting the activities of the corresponding oxide components by $\log K_{r,T,P} - \log f_{H_2O}$ where the reaction referred to is the transition of the oxide components to the appropriate cations. Figures 34b and 45b were inserted after Figures 34a and 45a at

the same temperature and pressure to illustrate that this is indeed the case. For example, $\log K_{r,T,P} - \log f_{H_2O}$ for the reactions

$$CaO(c) + 2H^+ \rightleftharpoons Ca^{++} + H_2O \qquad (48)$$

and

$$MgO(c) + 2H^+ \rightleftharpoons Mg^{++} + H_2O \qquad (68)$$

are 25.82 and 16.60 at 100°C and 1 bar and 25.79 and 16.50 at 100°C and 1000 bars, respectively. A comparison of the diagrams mentioned above confirms the fact that the stability field boundaries in each are displaced by these proportionality constants.

Up to this point, the response of mineral equilibria to changes in temperature, pressure and component chemical potential has been discussed without considering whether the chemical environment necessary to stabilize these minerals could, in fact, be achieved. As was mentioned earlier, possible mineral assemblages are limited by the equilibration of minerals within the system whose stabilities are indicated by saturation lines. For example, in Figure 34a, the brucite and portlandite saturation lines limit the solution composition such that the minerals Ca-olivine, rankinite and monticellite can never exist in equilibrium with the aqueous phase at 100°C, 1 bar and $\log f_{H_2O} = -0.007$. As the temperature increases to 300°C at 1 bar (Figure 36), the brucite and portlandite saturation lines move toward the quartz field and restrict the solution composition even further. However, by 400°C (Figure 37), brucite has dehydrated to periclase and the positioning of the periclase and portlandite saturation lines (the latter exceeding the limits of the diagram) permit the stable existence of any of the minerals occupying stability fields on the diagrams under the proper chemical conditions. At pressures of 500 and 1000 bars, the

portlandite and brucite saturation lines also encompass additional mineral stability fields with increasing temperature owing to the larger fugacities of H_2O at these pressures. Although the stability fields of Ca-olivine, rankinite, merwinite and monticellite lie mostly outside of these saturation lines at less than 200° to 300°C, increasing temperature, enhanced by the dehydration of brucite, causes their stability fields to be finally encompassed by the limiting saturation lines, at which time these minerals can exist in equilibrium with the aqueous phase in the proper chemical environment at the temperature and pressure under consideration. It is therefore apparent that at low temperatures (≃200°-300°C) and pressures up to 1000 bars, the stability of portlandite and brucite prevent the equilibration within the system of minerals such as Ca-olivine, rankinite, merwinite and monticellite which occur at large values of $\log a_{Ca^{++}}/(a_{H^+})^2$. However, at higher temperatures, some of the stability fields of these minerals are enclosed by the boundary saturation lines and thus the minerals can come to equilibrium within the system given the proper conditions. The observation that the stabilities of Ca-olivine, rankinite, merwinite and monticellite depend on chemical and physical conditions more extreme than those required to stabilize wollastonite or diopside, for example, appears to be in complete agreement with the fact that Ca-olivine and other related minerals are also rarer in nature than wollastonite and diopside. It is therefore important to remember that even if a mineral's stability field appears on these diagrams, the mineral will not be thermodynamically stable unless the chemical potentials of the proper components attain the values needed to stabilize it and are not limited by any saturation lines before the crucial values are reached.

Figures 52 to 57 illustrate the addition of a pure CO_2 phase to the

Figure 52. Activity diagram for the system $CaO-MgO-SiO_2-CO_2$ at 400°C, 1000 bars and log f_{CO_2} = 3.07 (fugacities of CO_2 in this and all following diagrams were calculated from the data of Ryzhenko and Volkov, 1971 and from equation (33) in text using CO_2 P-V-T data from Kennedy, 1954).

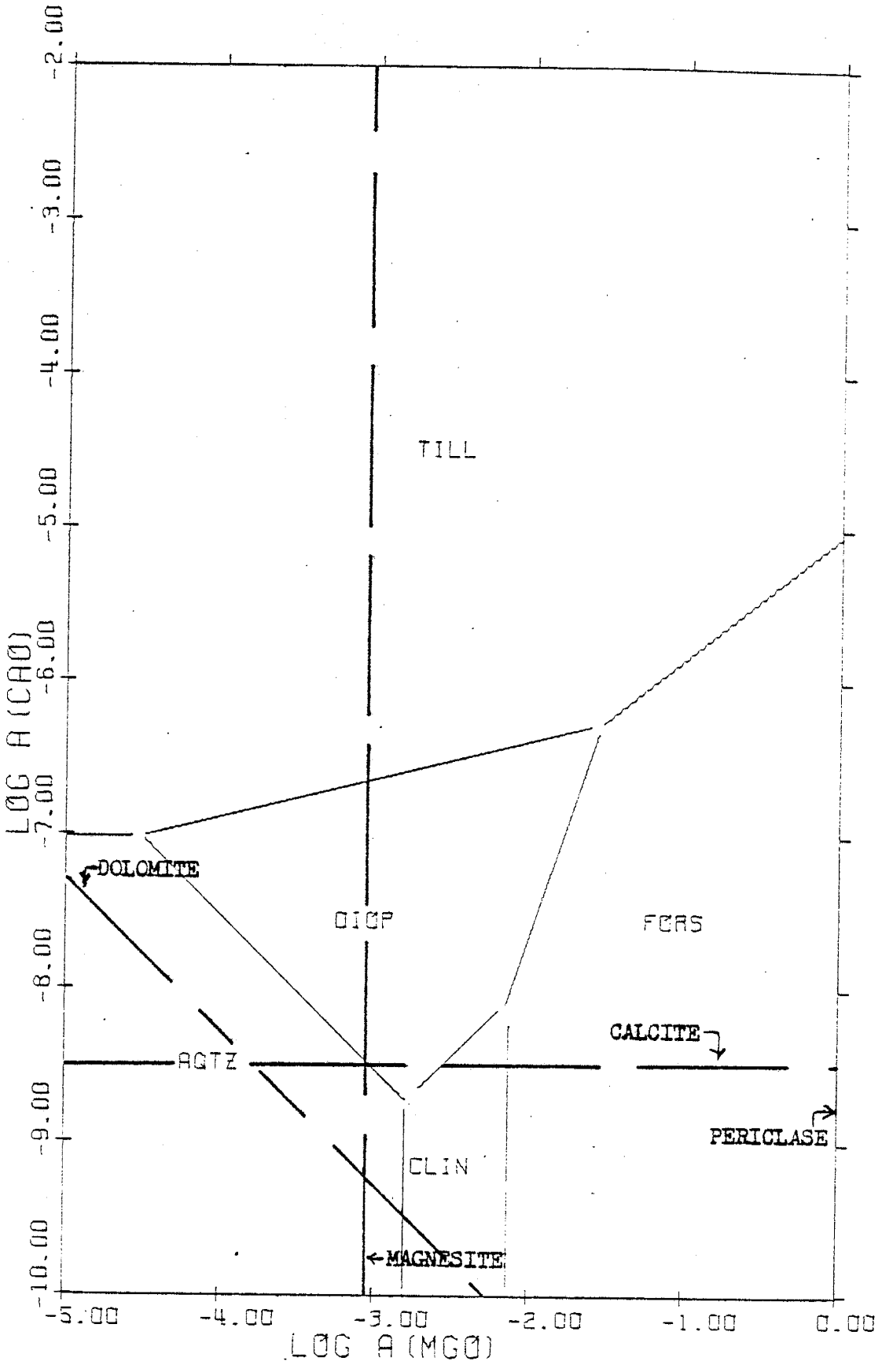
-2.00
-3.00
-4.00
-5.00
-6.00
-7.00
-8.00
-9.00
-10.00
LOG A (CAO)
TILL
DOLOMITE
DIOP
FORS
CALCITE
AQTZ
PERICLASE
CLIN
MAGNESITE
-5.00
-4.00
-3.00
-2.00
-1.00
0.00
LOG A (MGO)

Figure 53. Activity diagram for the system $CaO-MgO-SiO_2-CO_2$ at 600°C, 1000 bars and log f_{CO_2} = 3.10.

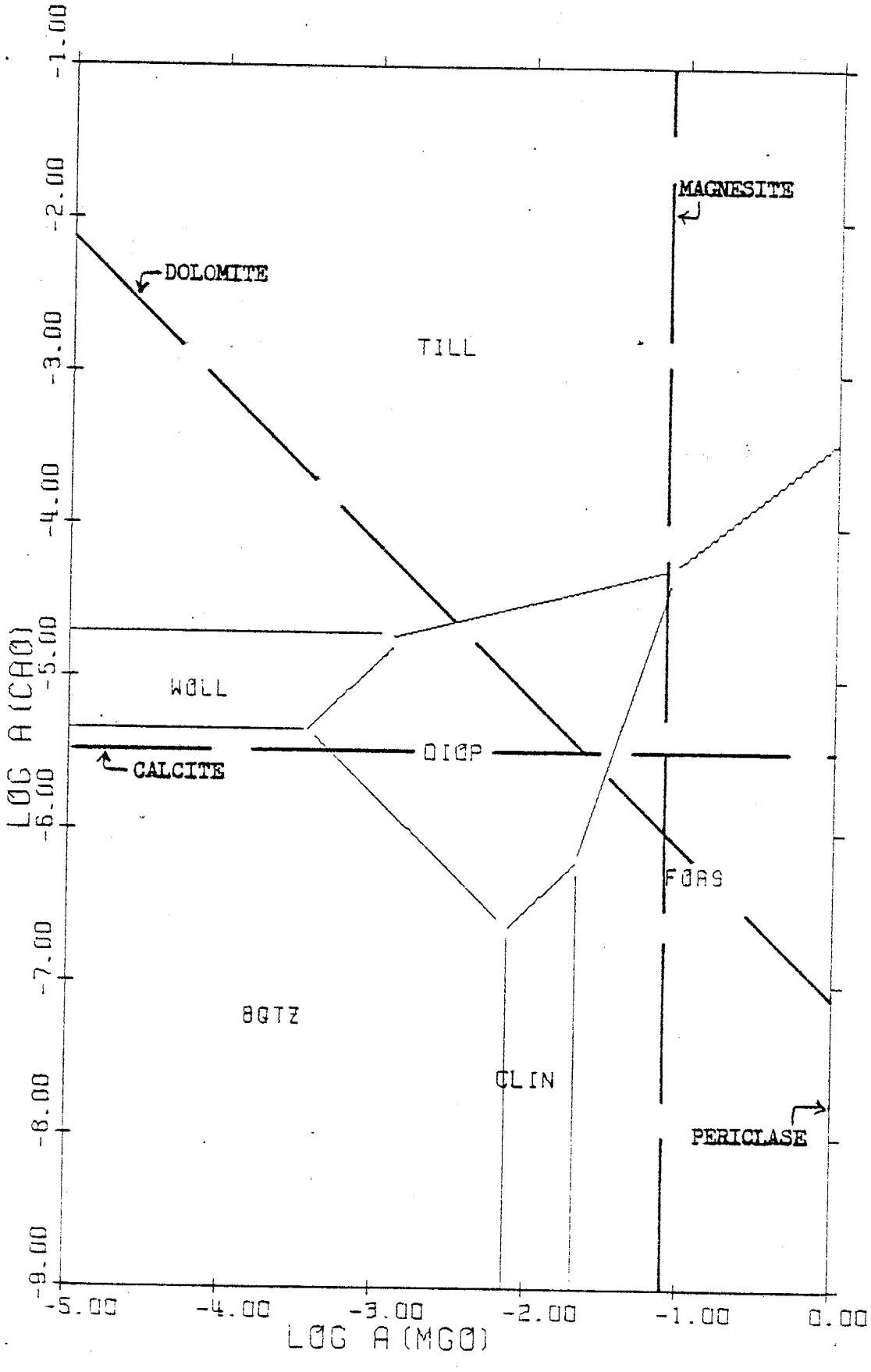
MAGNESITE
DOLOMITE
TILL
WOLL
DIOP
CALCITE
FORS
SQTZ
CLIN
PERICLASE
LOG A(CAO)
LOG A(MGO)
-1.00
-2.00
-3.00
-4.00
-5.00
-6.00
-7.00
-8.00
-9.00
-5.00
-4.00
-3.00
-2.00
-1.00
0.00

Figure 54. Activity diagram for the system $CaO-MgO-SiO_2-CO_2$ at 800°C, 1000 bars and log f_{CO_2} = 3.10.

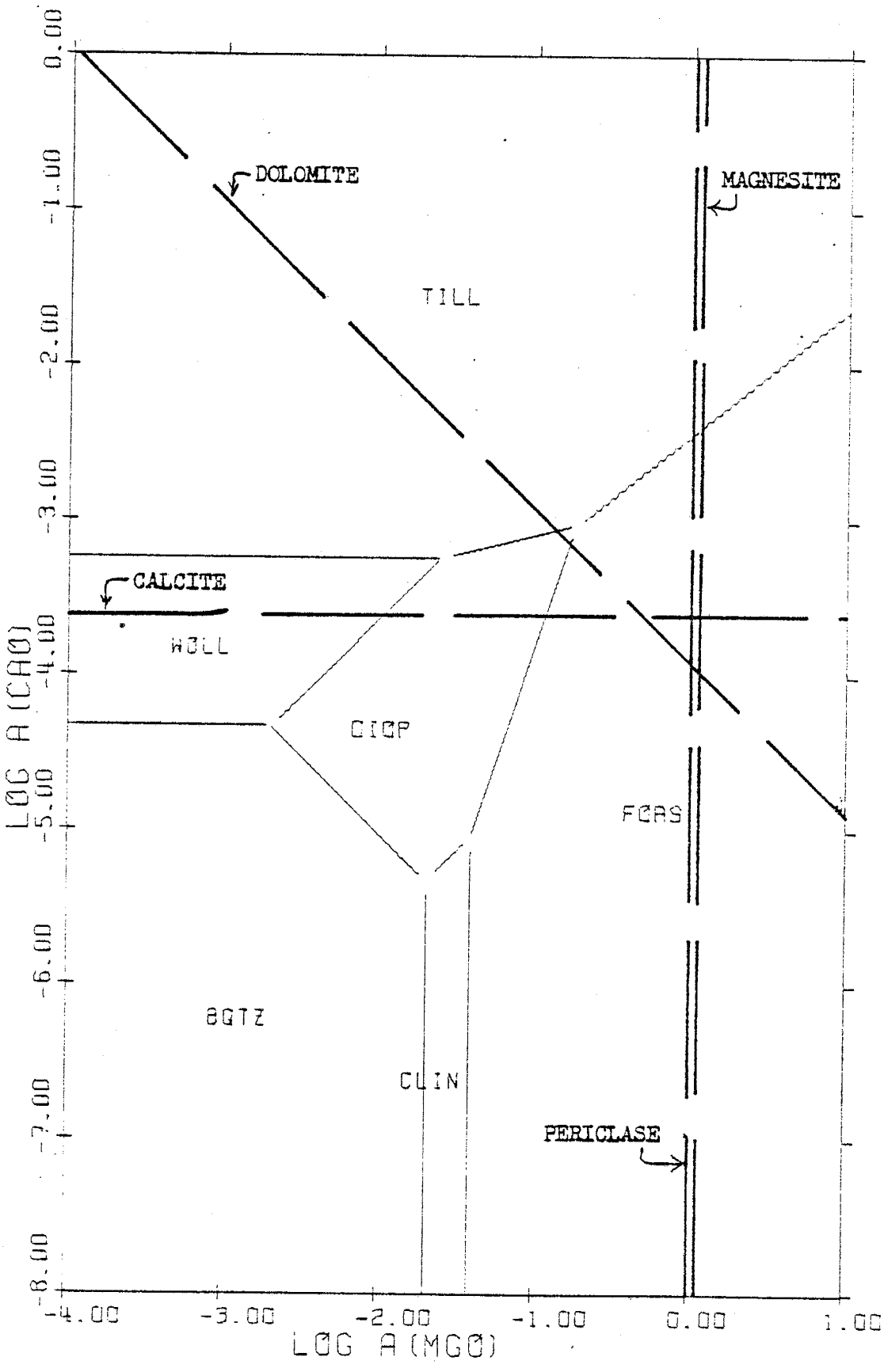
DOLOMITE
MAGNESITE
TILL
CALCITE
WOLL
DIOP
FORS
BGTZ
CLIN
PERICLASE
LOG A(CAO)
LOG A(MGO)
0.00
-1.00
-2.00
-3.00
-4.00
-5.00
-6.00
-7.00
-8.00
-4.00
-3.00
-2.00
-1.00
0.00
1.00

Figure 55. Activity diagram for the system $CaO-MgO-SiO_2-CO_2$ at 600°C, 1 bar and log f_{CO_2} = 0.0.

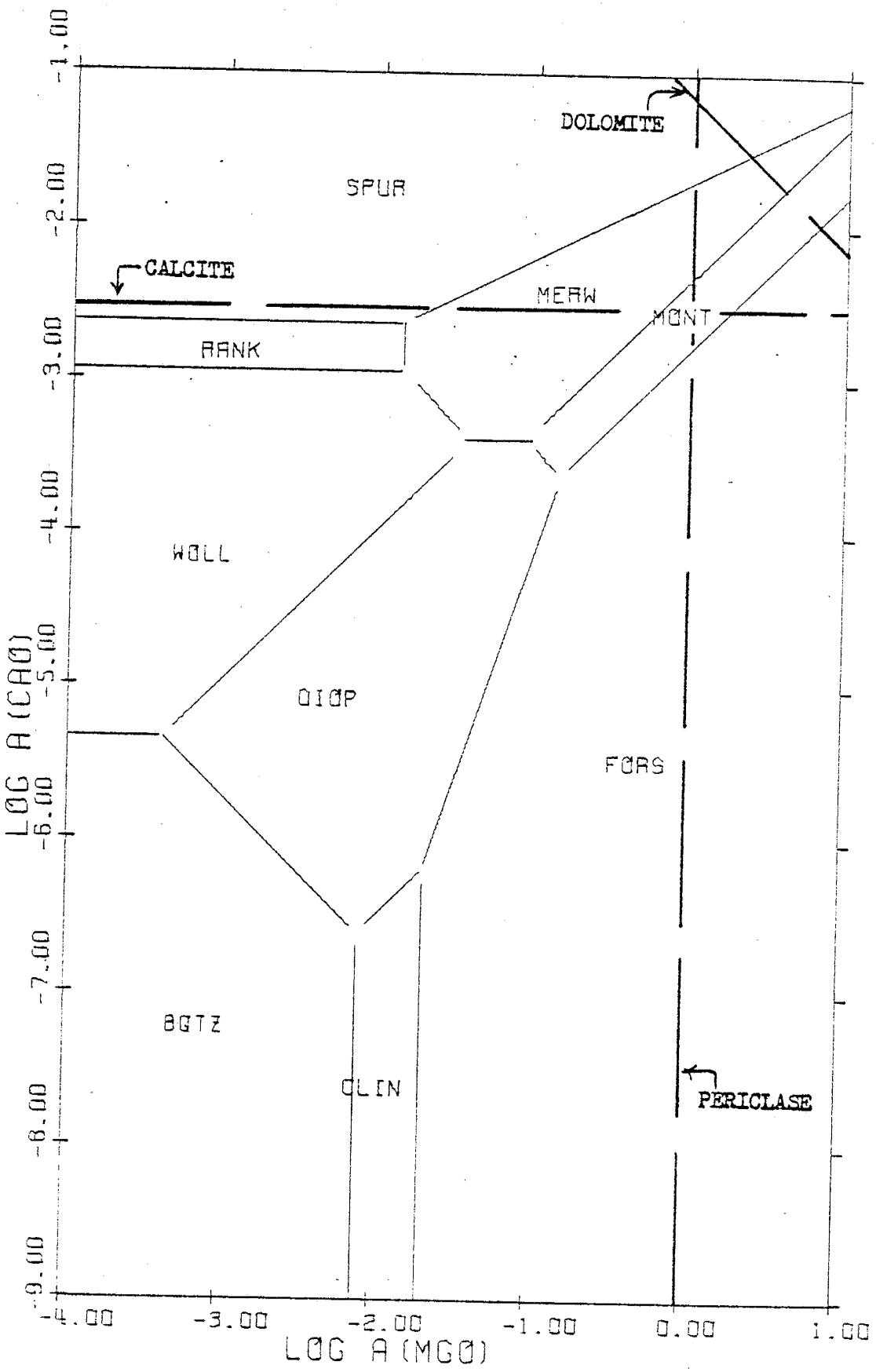
DOLOMITE
SPUR
CALCITE
MERW
MONT
RANK
WOLL
DIOP
FORS
BGTZ
CLIN
PERICLASE
LOG A(CAO)
LOG A(MGO)
-1.00
-2.00
-3.00
-4.00
-5.00
-6.00
-7.00
-8.00
-9.00
-4.00
-3.00
-2.00
-1.00
0.00
1.00

Figure 56. Activity diagram for the system $CaO-MgO-SiO_2-CO_2$ at 600°C, 500 bars and log f_{CO_2} = 2.74.

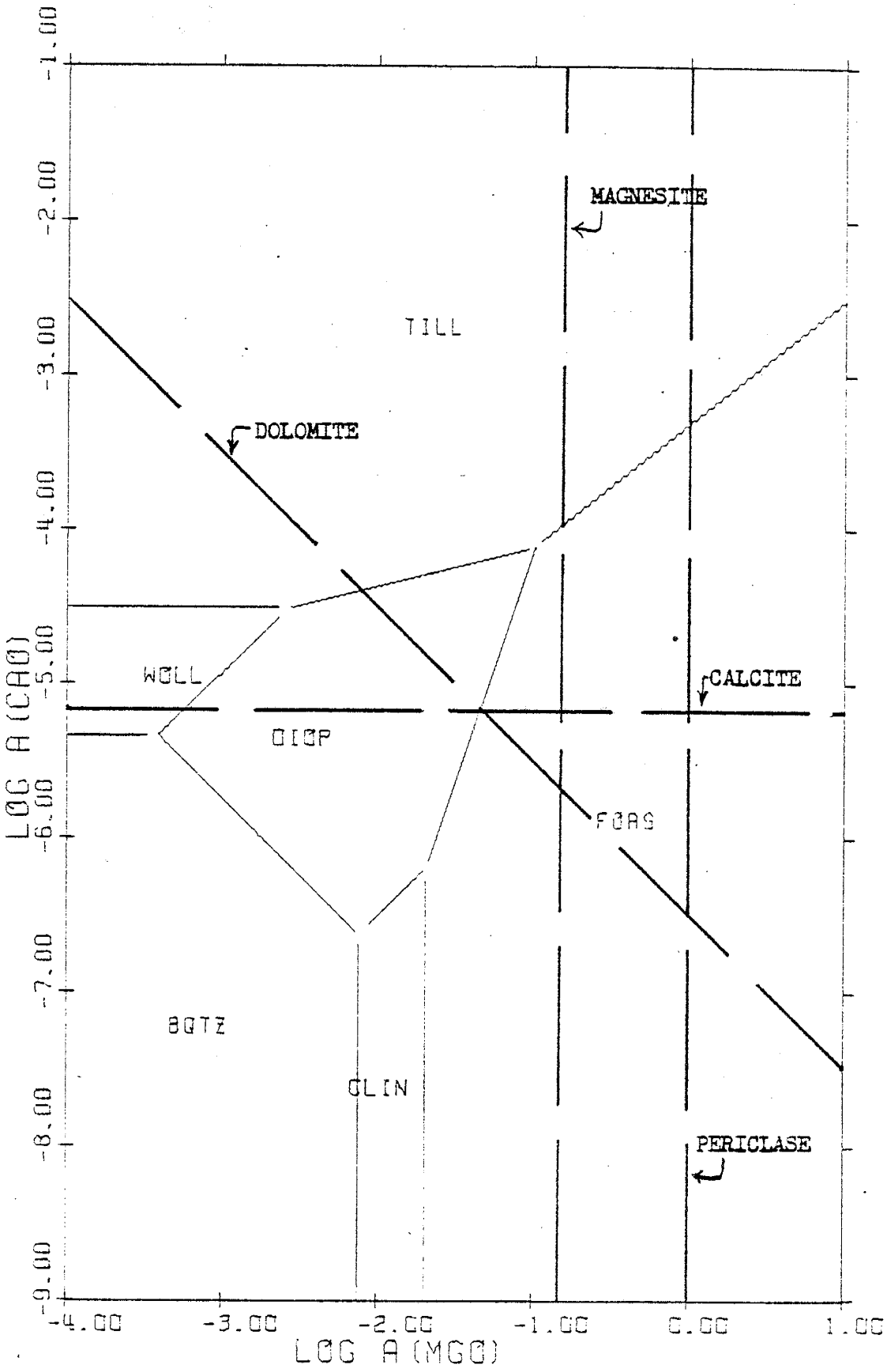
MAGNESITE
TILL
DOLOMITE
WOLL
DIOP
CALCITE
FORS
BOTZ
CLIN
PERICLASE
LOG A (CAO)
LOG A (MGO)
-1.00
-2.00
-3.00
-4.00
-5.00
-6.00
-7.00
-8.00
-9.00
-4.00
-3.00
-2.00
-1.00
0.00
1.00

Figure 57. Activity diagram for the system $CaO-MgO-SiO_2-CO_2$ at 600°C, 1000 bars and log f_{CO_2} = 3.10.

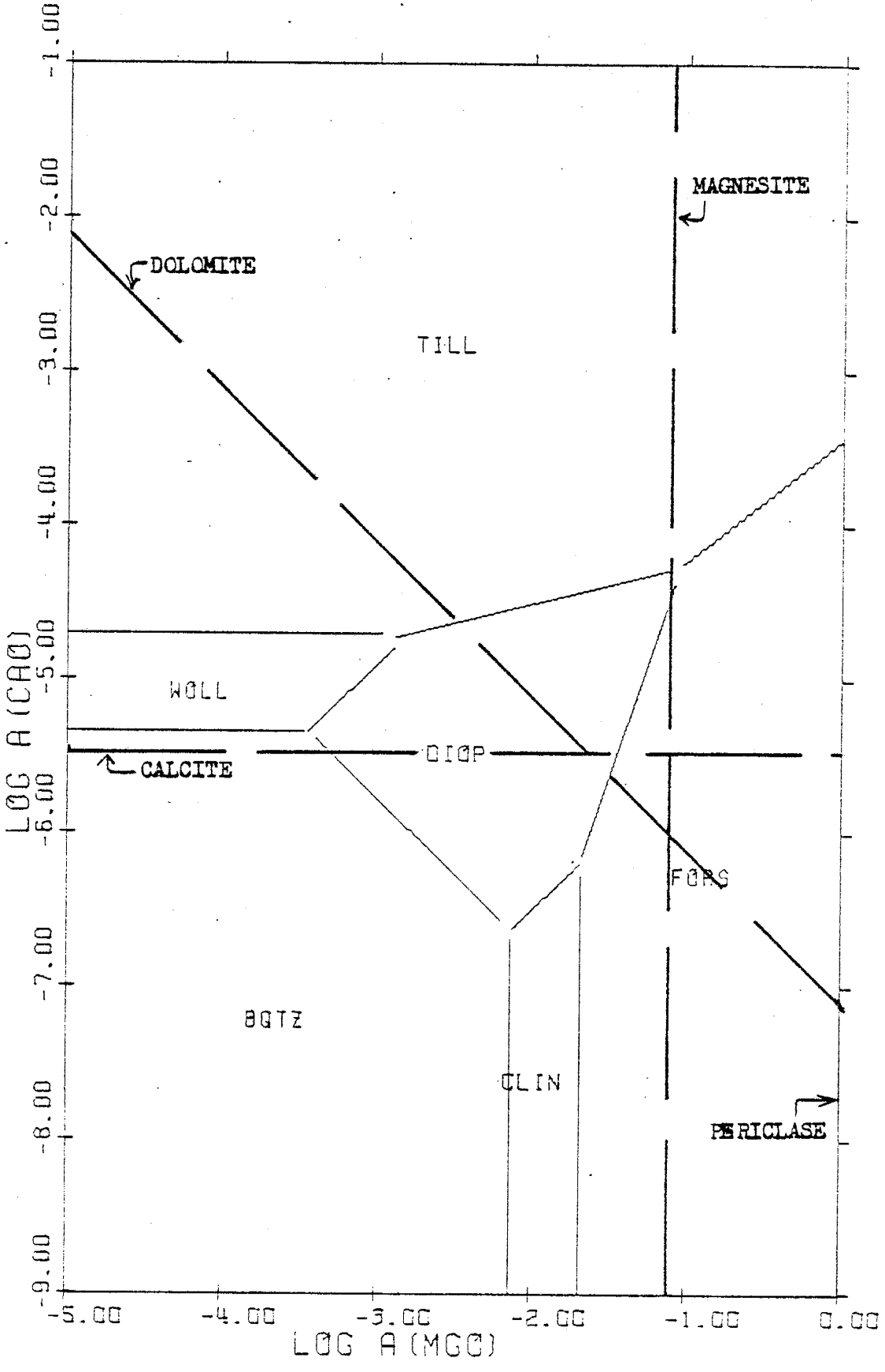
MAGNESITE
DOLOMITE
TILL
WOLL
DIOP
CALCITE
FORS
BRTZ
CLIN
PERICLASE
LOG A(CAO)
LOG A(MGO)
-1.00
-2.00
-3.00
-4.00
-5.00
-6.00
-7.00
-8.00
-9.00
-5.00
-4.00
-3.00
-2.00
-1.00
0.00

system $CaO-MgO-SiO_2$ and its effects upon mineral equilibria. The addition of CO_2 to the system necessitates the ability to represent the stability fields of spurrite and tilleyite on the activity diagrams along with the saturation lines of dolomite, calcite and magnesite. Fugacity coefficients required for these calculations were obtained from Ryzhenko and Volkov (1971) and from equation (33) using CO_2 P-V-T data from Kennedy (1954).

Figures 52 to 54 show that at a constant CO_2 pressure of 1000 bars and temperatures ranging from 400° to 800°C, the apparent consequence of adding CO_2 to the system is the stabilization of tilleyite at the expense of monticellite, merwinite, Ca-olivine, rankinite, wollastonite, diopside and forsterite. In fact, the tilleyite stability field actually imposes upon the quartz field at 400°C and 1000 bars at low chemical potentials of MgO(c). However, a closer examination of these diagrams reveals that at values of log $a_{CaO(c)}$ and log $a_{MgO(c)}$ lower than those required to stabilize any silicate on the 400°C, 1000 bars diagram (Figure 52), the carbonate minerals calcite, dolomite and magnesite come to equilibrium within the system. This condition is indicated by the positioning of the "carbonate boundary", formed by the saturation lines of calcite, dolomite and magnesite, within the quartz field. When any of these carbonate minerals come to equilibrium within the system, the system is essentially "buffered" with respect to log $a_{CaO(c)}$ and/or log $a_{MgO(c)}$, depending on which carbonate mineral has stabilized. That is, the equilibration of calcite or magnesite within the system will limit log $a_{CaO(c)}$ or log $a_{MgO(c)}$, respectively, and saturation with respect to dolomite will fix the ratio of these two activities at a constant value. Therefore, none of the indicated silicate minerals can exist in equilibrium with the aqueous phase at 400°C and 1000 bars. However, as the temperature increases to 600° and 800°C at

the same pressure, the stability fields of clinoenstatite, forsterite, diopside and wollastonite are eventually encompassed by the carbonate boundary and thus can exist in equilibrium with the aqueous phase at the temperature and pressure under consideration. The chemical conditions required for tilleyite stability can never be attained at temperatures as high as 800°C at a pressure of 1000 bars because increasing temperature, despite its tendency to expand the carbonate boundary, fails to offset the effect of 1000 bars in stabilizing calcite before the tilleyite stability field can be reached.

The consideration of pressure as a variable in these diagrams is, in essence, the consideration of the effects of variations in the fugacity of CO_2 upon the stability fields of the CO_2-bearing minerals. Figures 55 to 57, drawn at 600°C and 1, 500 and 1000 bars, show that although the stability field boundaries between anhydrous minerals do not shift to any great degree with pressure, the relative stability of spurrite and tilleyite is highly dependent on the pressure exerted on the system because of its effect on the fugacity of CO_2. For example, as pressure increases, the CO_2-bearing mineral spurrite converts to tilleyite, which in turn progressively eliminates the stability fields of the other silicates until it becomes the only phase to occur at higher values of log $a_{CaO(c)}$. (The conversion of spurrite to tilleyite between 1 and 500 bars at this temperature will be discussed below.) These diagrams also illustrate the movement of the calcite, magnesite and dolomite saturation lines toward the quartz field and lower values of $a_{CaO(c)}$ and $a_{MgO(c)}$ with increasing pressure, thereby reducing the stability range of the silicates in the aqueous phase. However, at 600°C and pressures as low as 1 bar, even spurrite, rankinite, monticellite and merwinite can exist in equilibrium with the aqueous phase

under the proper chemical conditions.

As a preliminary investigation, Figures 52 to 57 would thus seem to indicate that although increasing pressure favors carbonate rather than silicate stability in a pure CO_2 system, increasing temperature tends to favor silicate rather than carbonate stability. Whereas spurrite can exist in equilibrium with the aqueous phase only at very low CO_2 pressures ($\simeq$1 bar) and temperatures $\geq$600°C, the minerals wollastonite, diopside, clinoenstatite and forsterite appear to be stable over a much wider range of temperature and pressure. Monticellite, merwinite and rankinite can exist in equilibrium with the aqueous phase only at temperatures and pressures paralleling those of spurrite stability because higher pressures and lower temperatures would cause their stability fields to be either eliminated by tilleyite or to be inaccessible to the aqueous phase owing to the movement of the calcite saturation line toward the quartz field.

In natural environments, a mixed H_2O-CO_2 phase would be expected to exist in equilibrium with metamorphic assemblages rather than a pure H_2O or CO_2 phase. Therefore, the relative stabilities of minerals and the problem of silicate stability in relation to the equilibration of carbonates will be studied as a function of X_{CO_2} at a fixed temperature and pressure.

As was shown above, pressures $\geq$500 bars effectively prohibit the stability of silicates such as monticellite, merwinite, rankinite, spurrite and tilleyite even at temperatures as high as 800°C in a pure CO_2 system because of the tendency of increasing pressure to stabilize calcite at lower values of log $a_{CaO(c)}$ than are required for the stability of the silicates listed above. However, if the CO_2 in the fluid phase was "diluted" by H_2O, the fugacity of CO_2 at the temperature and pressure of interest would decrease, thereby causing the carbonate saturation lines to expand

away from the quartz field. Figures 58 to 63 were constructed at 100 bars, 800°C and varying X_{CO_2} to illustrate the effect that a changing mole fraction of CO_2 in the fluid phase would have upon mineral equilibria. H_2O and CO_2 were assumed to mix ideally because of the low pressure and high temperature involved. These diagrams show that the stability field of tilleyite is gradually reduced in size as X_{CO_2} decreases, allowing not only the expansion of the merwinite field (which has eliminated the stability field of monticellite at lower temperatures) but also the appearance of the rankinite stability field at $X_{CO_2} = 0.4$. At $X_{CO_2} = 1.0$, the calcite saturation line lies just below the tilleyite-wollastonite stability field boundary, but as X_{CO_2}, and therefore f_{CO_2}, decreases at a constant temperature and pressure, it moves up to lie just within the tilleyite stability field at $X_{CO_2} = 0.6$. It is apparent that although reducing the mole fraction of CO_2 in the fluid phase does not have a drastic effect either on the size of the stability fields of the CO_2-bearing minerals spurrite and tilleyite or on the positioning of the calcite saturation line, the combination of the two effects results in the possibility of equilibration of spurrite or tilleyite within the system at 800°C and 100 bars at a mole fraction of CO_2 as high as 0.6.

Figures 64 to 66, drawn at 1 bar and 400°, 600° and 800°C for a pure CO_2 system, confirm the fact that spurrite, monticellite, merwinite and rankinite can only come to equilibrium at temperatures of about 600°C or higher at pressures as low as 1 bar. As previously noted, these minerals, including tilleyite, are generally stable only under pressures $\leq$100 bars at temperatures $\geq$600°C, being highly dependent on the positioning of the calcite saturation line. In comparison, the minerals clinoenstatite, diopside, forsterite and wollastonite are generally quite stable over a range

Figure 58. Activity diagram for the system $CaO-MgO-SiO_2-CO_2$ at 800°C, 100 bars and log f_{CO_2} = 2.011 (X_{CO_2} = 1.0).

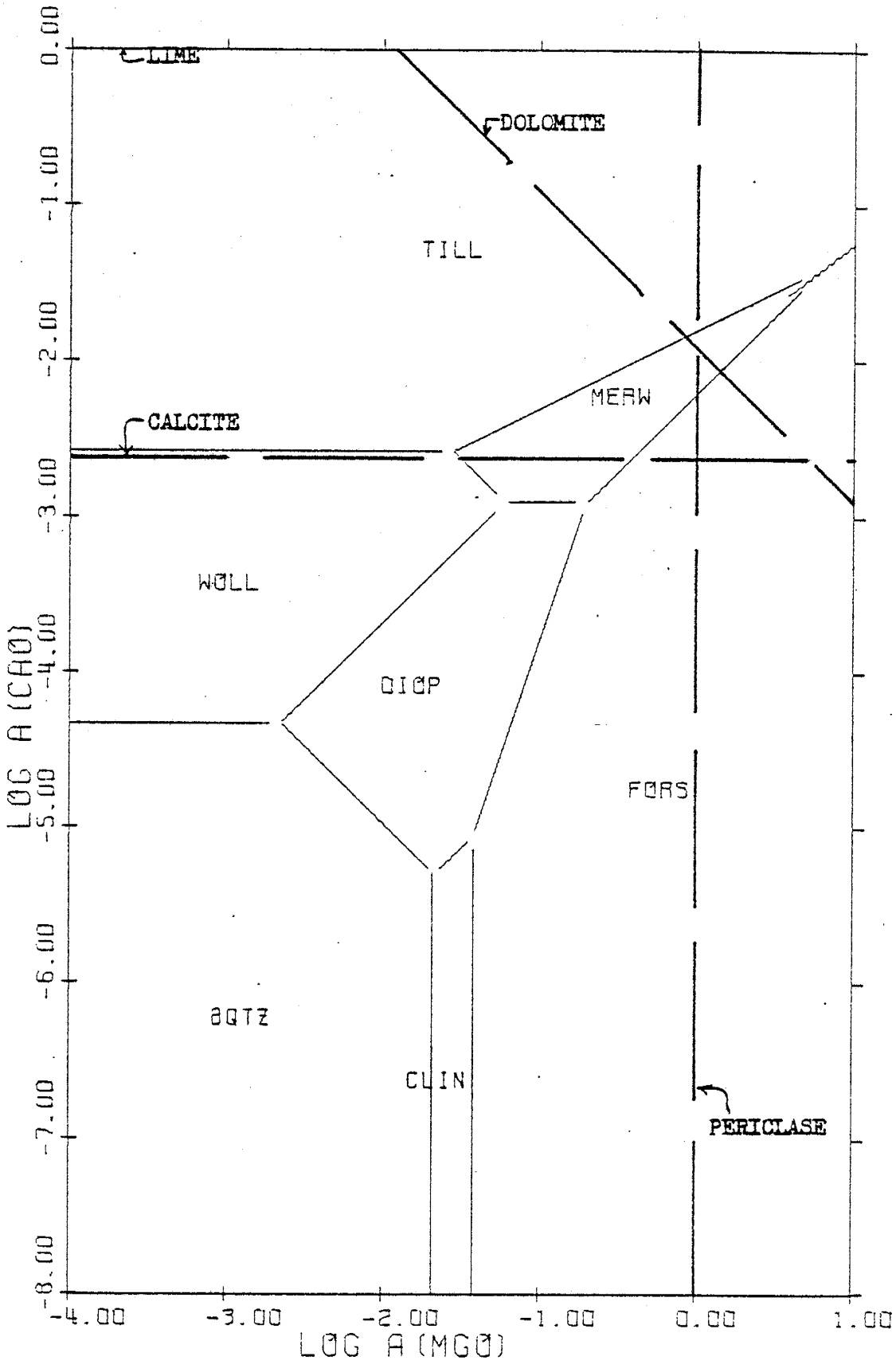
LIME
DOLOMITE
TILL
MERW
CALCITE
WOLL
DICP
FORS
QTZ
CLIN
PERICLASE
0.00
-1.00
-2.00
-3.00
-4.00
-5.00
-6.00
-7.00
-8.00
LOG A (CAO)
-4.00
-3.00
-2.00
-1.00
0.00
1.00
LOG A (MGO)

Figure 59. Activity diagram for the system $CaO-MgO-SiO_2-H_2O-CO_2$ at 800°C, 100 bars, log f_{H_2O} = 1.289 and log f_{CO_2} = 1.914 (X_{CO_2} = 0.8).

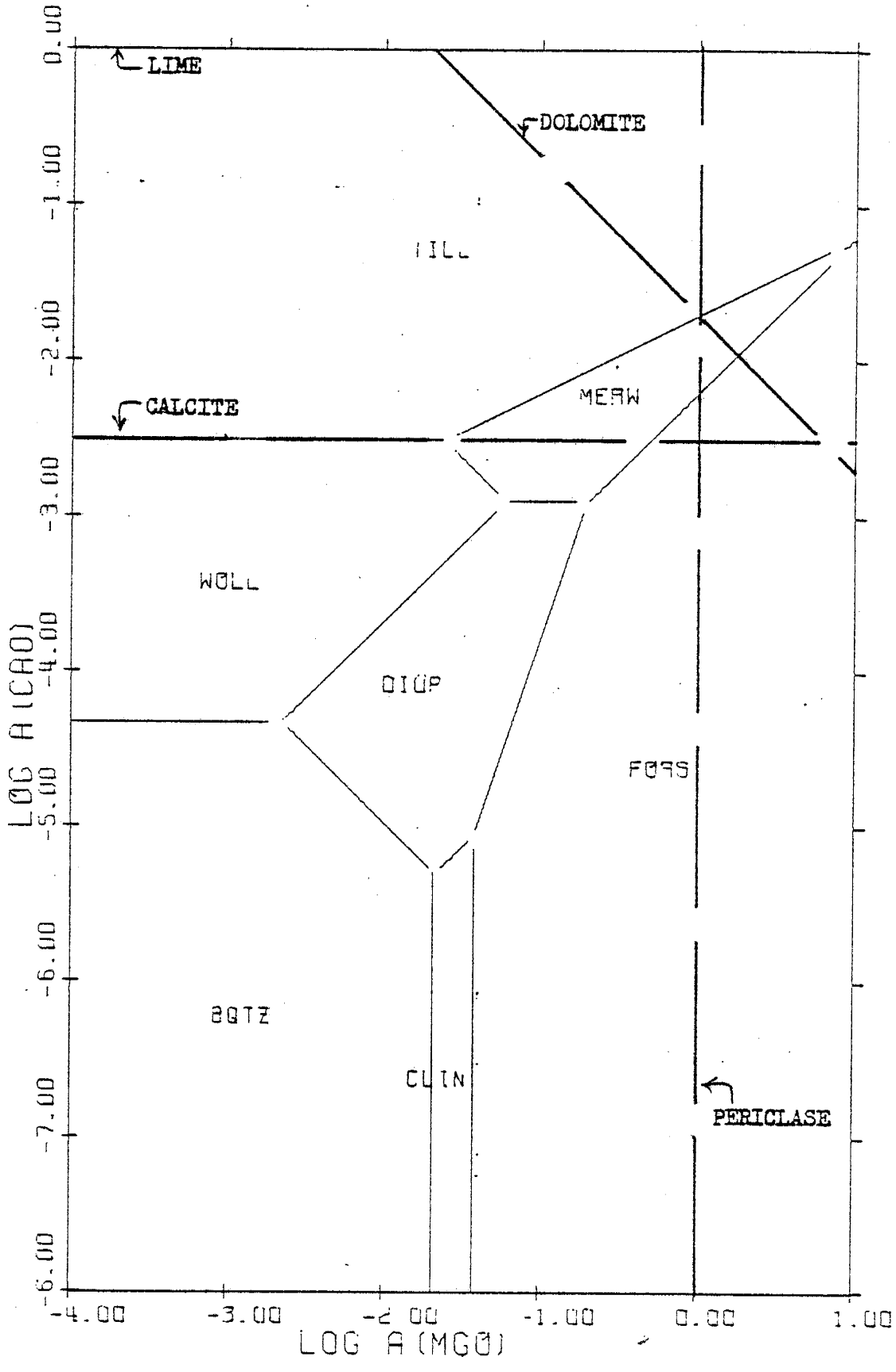
LIME
DOLOMITE
TILL
CALCITE
MERW
WOLL
DIOP
FORS
BQTZ
CLIN
PERICLASE
0.00
-1.00
-2.00
-3.00
-4.00
-5.00
-6.00
-7.00
-6.00
-4.00
-3.00
-2.00
-1.00
0.00
1.00
LOG A(CAO)
LOG A(MGO)

Figure 60. Activity diagram for the system $CaO-MgO-SiO_2-H_2O-CO_2$ at 800°C, 100 bars, log f_{H_2O} = 1.59 and log f_{CO_2} = 1.789 (X_{CO_2} = 0.6).

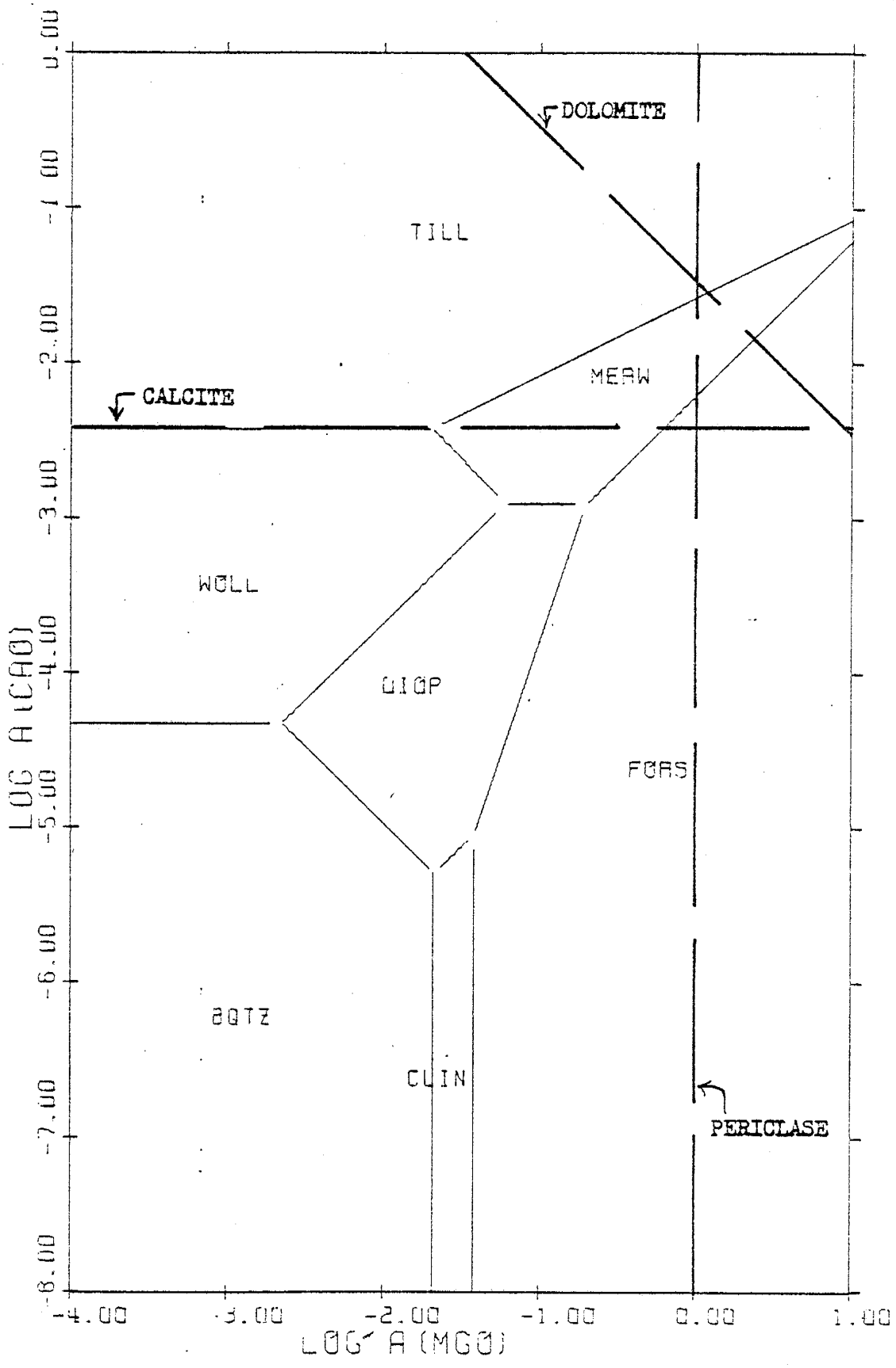
DOLOMITE
TILL
MEAW
CALCITE
WOLL
DIOP
FORS
QTZ
CLIN
PERICLASE
LOG A(CAO)
LOG A(MGO)
0.00
-1.00
-2.00
-3.00
-4.00
-5.00
-6.00
-7.00
-8.00
-4.00
-3.00
-2.00
-1.00
0.00
1.00

Figure 61. Activity diagram for the system $CaO-MgO-SiO_2-H_2O-CO_2$ at 800°C, 100 bars, log f_{H_2O} = 1.766 and log f_{CO_2} = 1.613 (X_{CO_2} = 0.4).

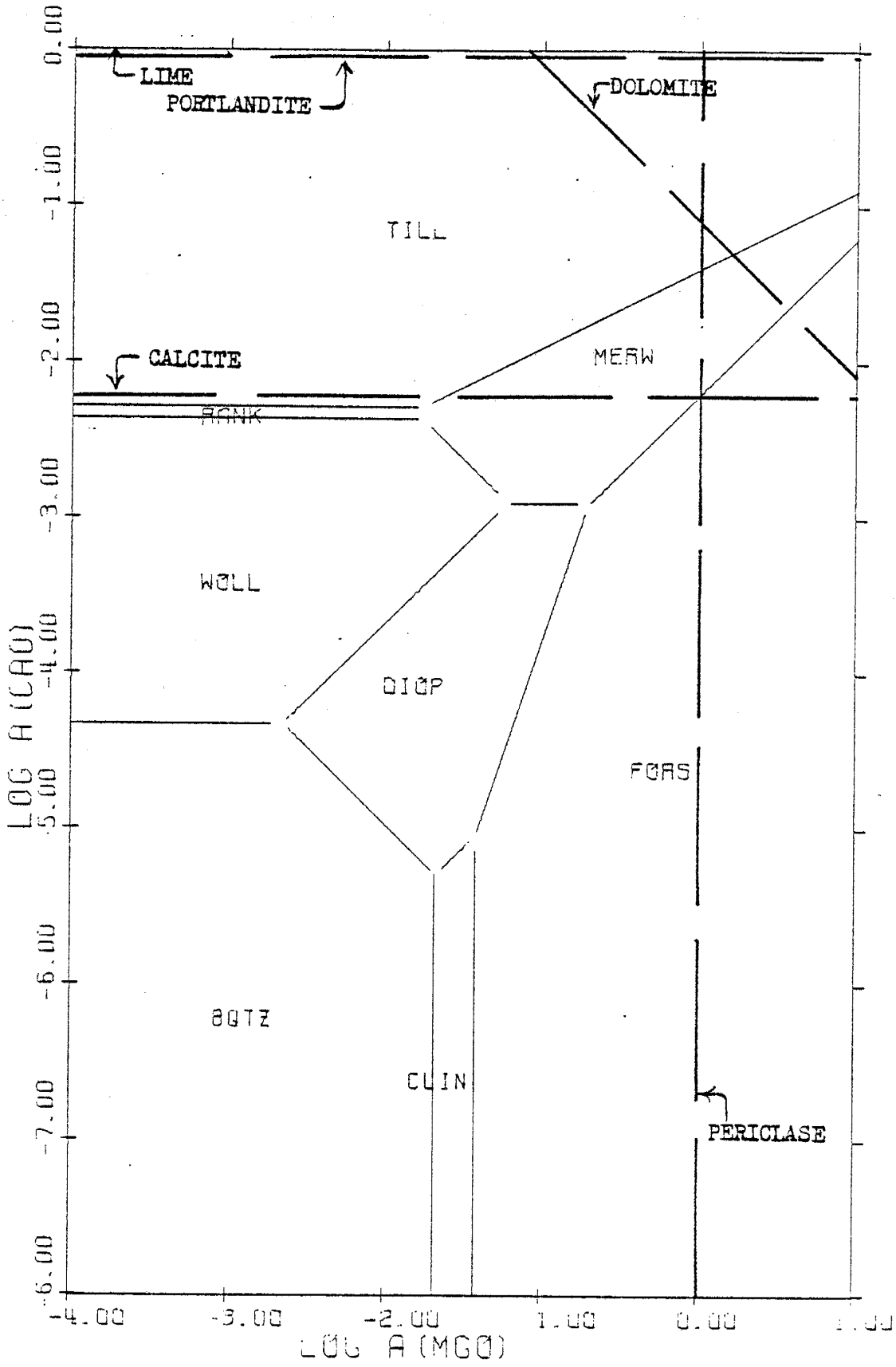
LIME
PORTLANDITE
DOLOMITE
TILL
CALCITE
MERW
RANK
WOLL
DIOP
FORS
QTZ
CLIN
PERICLASE
LOG A (CAO)
LOG A (MGO)
0.00
-1.00
-2.00
-3.00
-4.00
-5.00
-6.00
-7.00
-8.00
-4.00
-3.00
-2.00
1.00
0.00

Figure 62. Activity diagram for the system $CaO-MgO-SiO_2-H_2O-CO_2$ at 800°C, 100 bars, log f_{H_2O} = 1.891 and log f_{CO_2} = 1.312 (X_{CO_2} = 0.2).

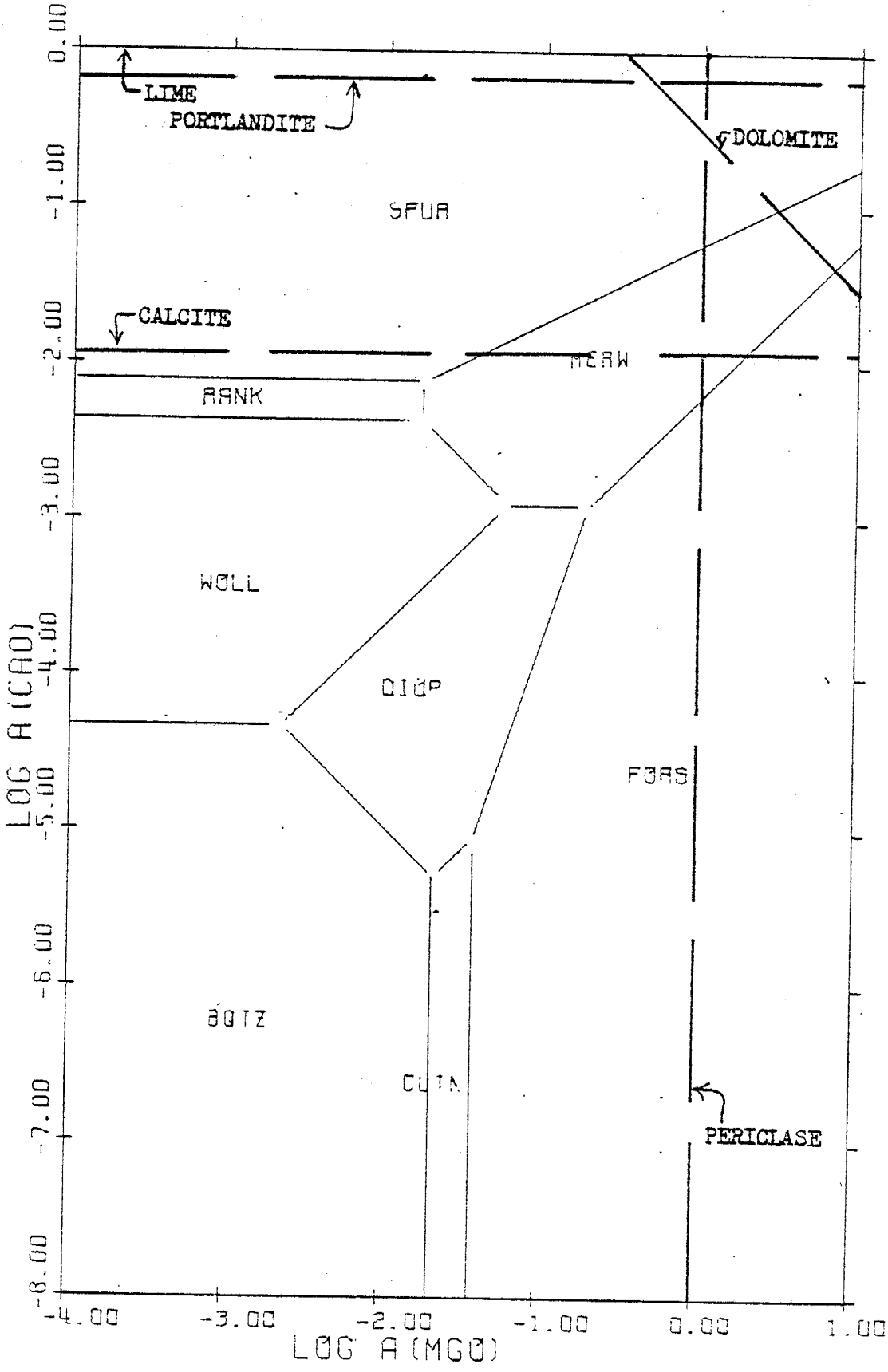
LIME
PORTLANDITE
DOLOMITE
SPUR
CALCITE
RANK
WOLL
DIOP
FORS
PERICLASE
LOG A(CAO)
LOG A(MGO)
0.00
-1.00
-2.00
-3.00
-4.00
-5.00
-6.00
-7.00
-8.00
-4.00
-3.00
-2.00
-1.00
0.00
1.00

Figure 63. Activity diagram for the system $CaO-MgO-SiO_2-H_2O-CO_2$ at 800°C, 100 bars and log f_{H_2O} = 1.99 (X_{CO_2} = 0.0).

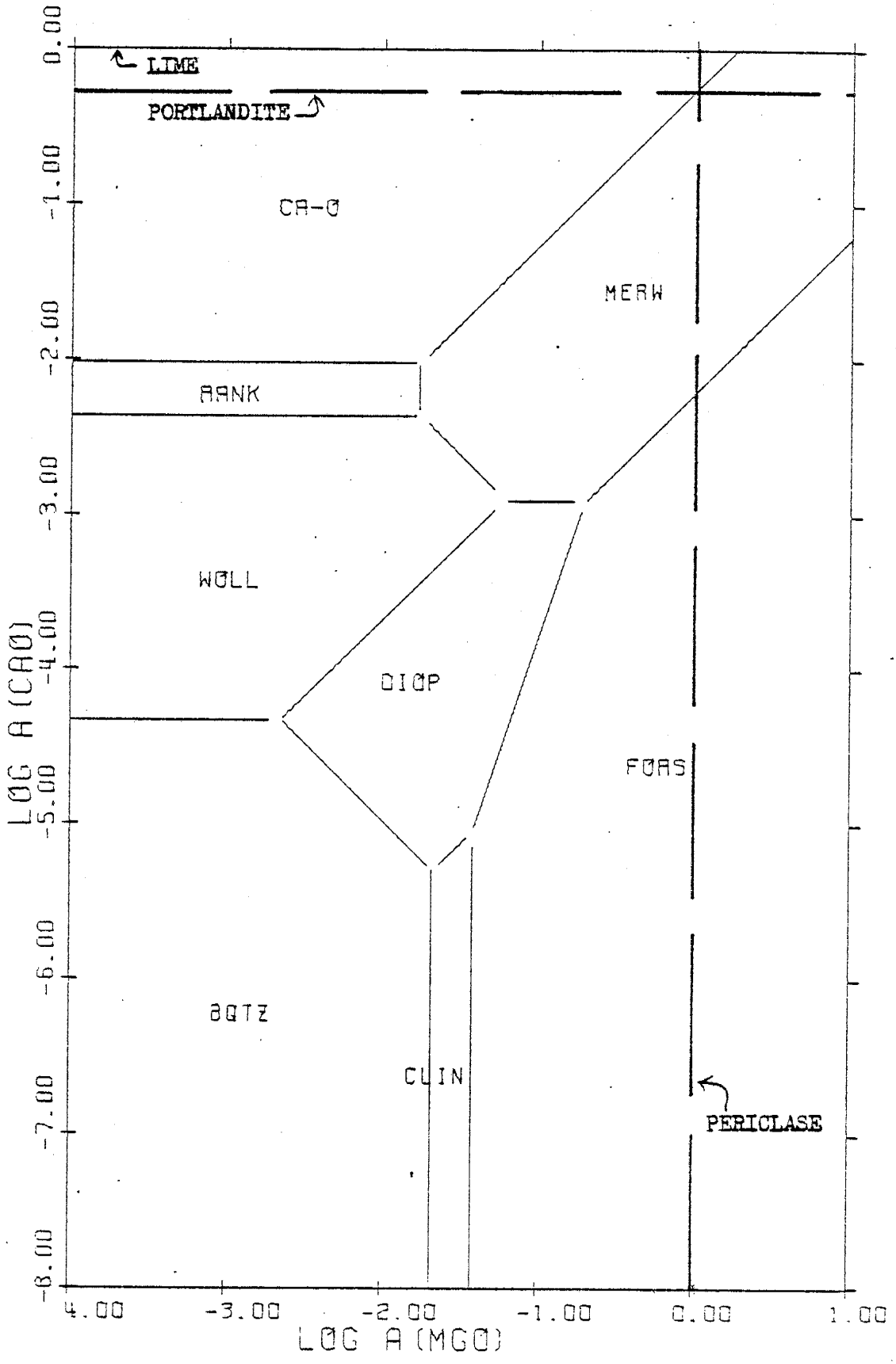
LIME
PORTLANDITE
CA-O
MERW
ANAK
WOLL
DIOP
FOR5
BQTZ
CLIN
PERICLASE
0.00
-1.00
-2.00
-3.00
-4.00
-5.00
-6.00
-7.00
-8.00
LOG A(CAO)
-4.00
-3.00
-2.00
-1.00
0.00
1.00
LOG A(MGO)

Figure 64. Activity diagram for the system $CaO-MgO-SiO_2-CO_2$ at 400°C, 1 bar and log f_{CO_2} = 0.0.

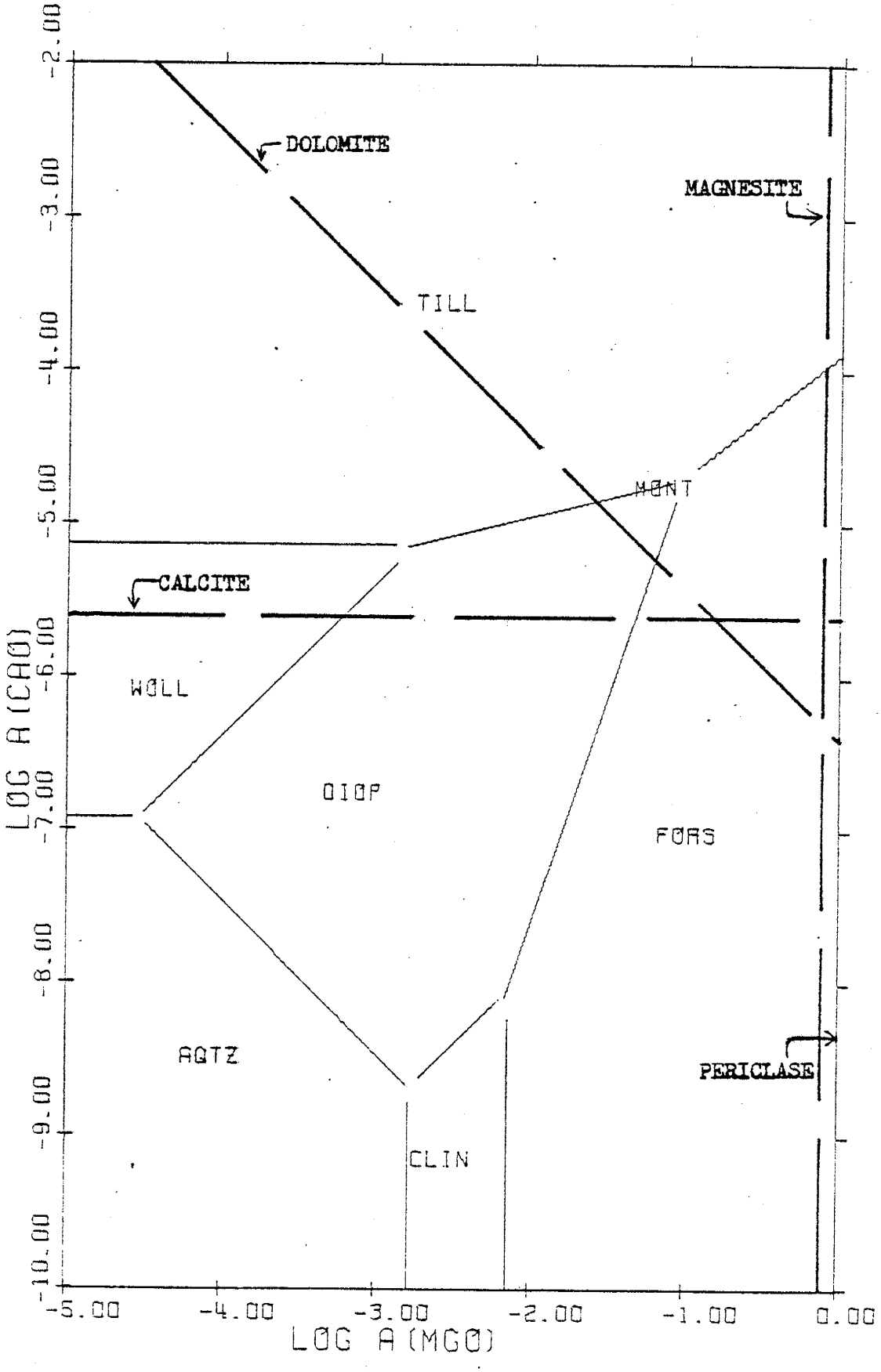
DOLOMITE
MAGNESITE
TILL
MONT
CALCITE
WOLL
DIOP
FORS
AQTZ
CLIN
PERICLASE
LOG A(CAO)
LOG A(MGO)
-2.00
-3.00
-4.00
-5.00
-6.00
-7.00
-8.00
-9.00
-10.00
-5.00
-4.00
-3.00
-2.00
-1.00
0.00

Figure 65. Activity diagram for the system $CaO-MgO-SiO_2-CO_2$ at 600°C, 1 bar and log f_{CO_2} = 0.0.

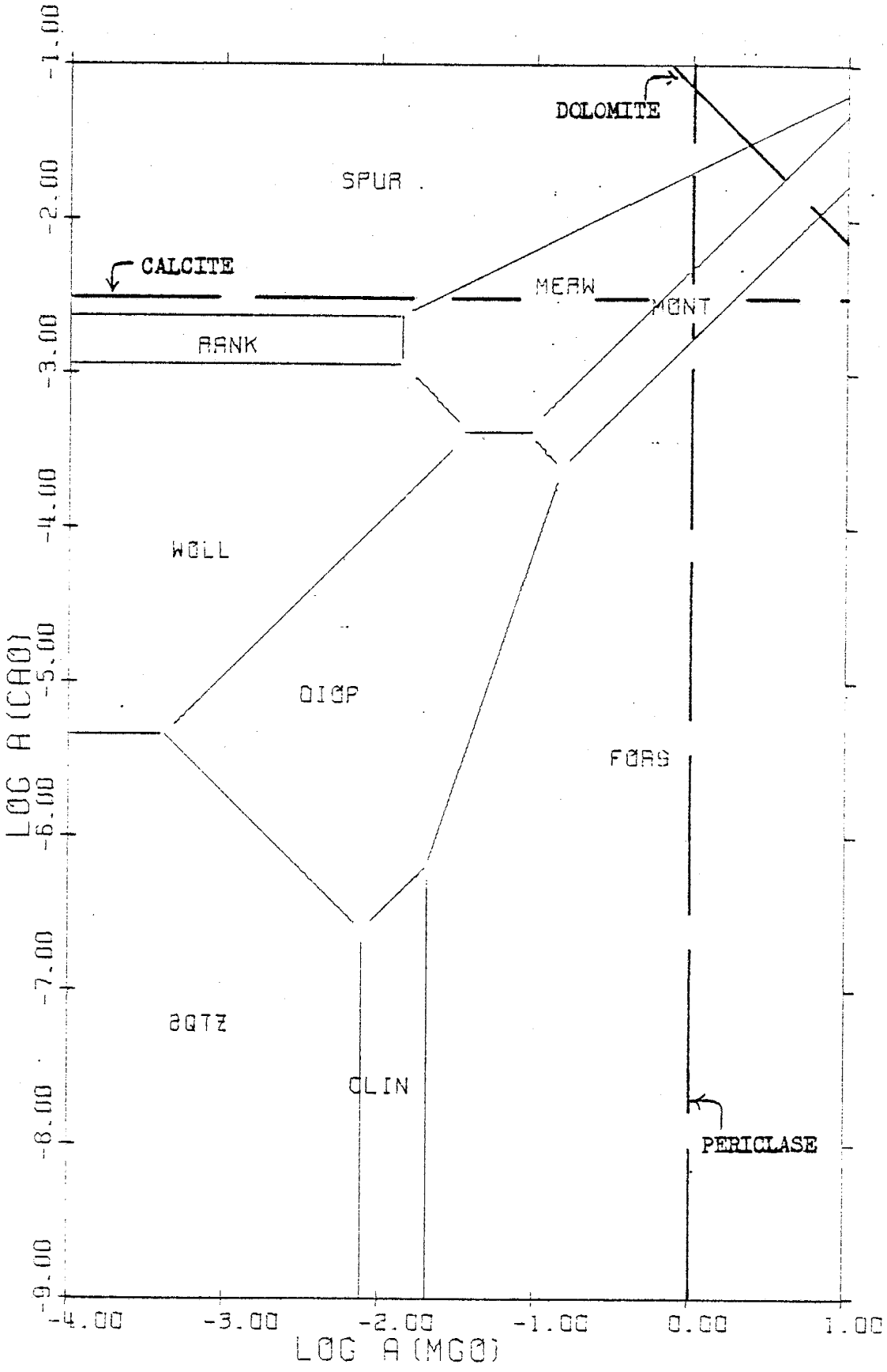
DOLOMITE
SPUR
CALCITE
MERW
MONT
RANK
WOLL
DIOP
FORS
QTZ
CLIN
PERICLASE
LOG A(CAO)
LOG A(MGO)
-1.00
-2.00
-3.00
-4.00
-5.00
-6.00
-7.00
-8.00
-9.00
-4.00
-3.00
-2.00
-1.00
0.00
1.00

Figure 66. Activity diagram for the system $CaO-MgO-SiO_2-CO_2$ at 800°C, 1 bar and log f_{CO_2} = 0.0.

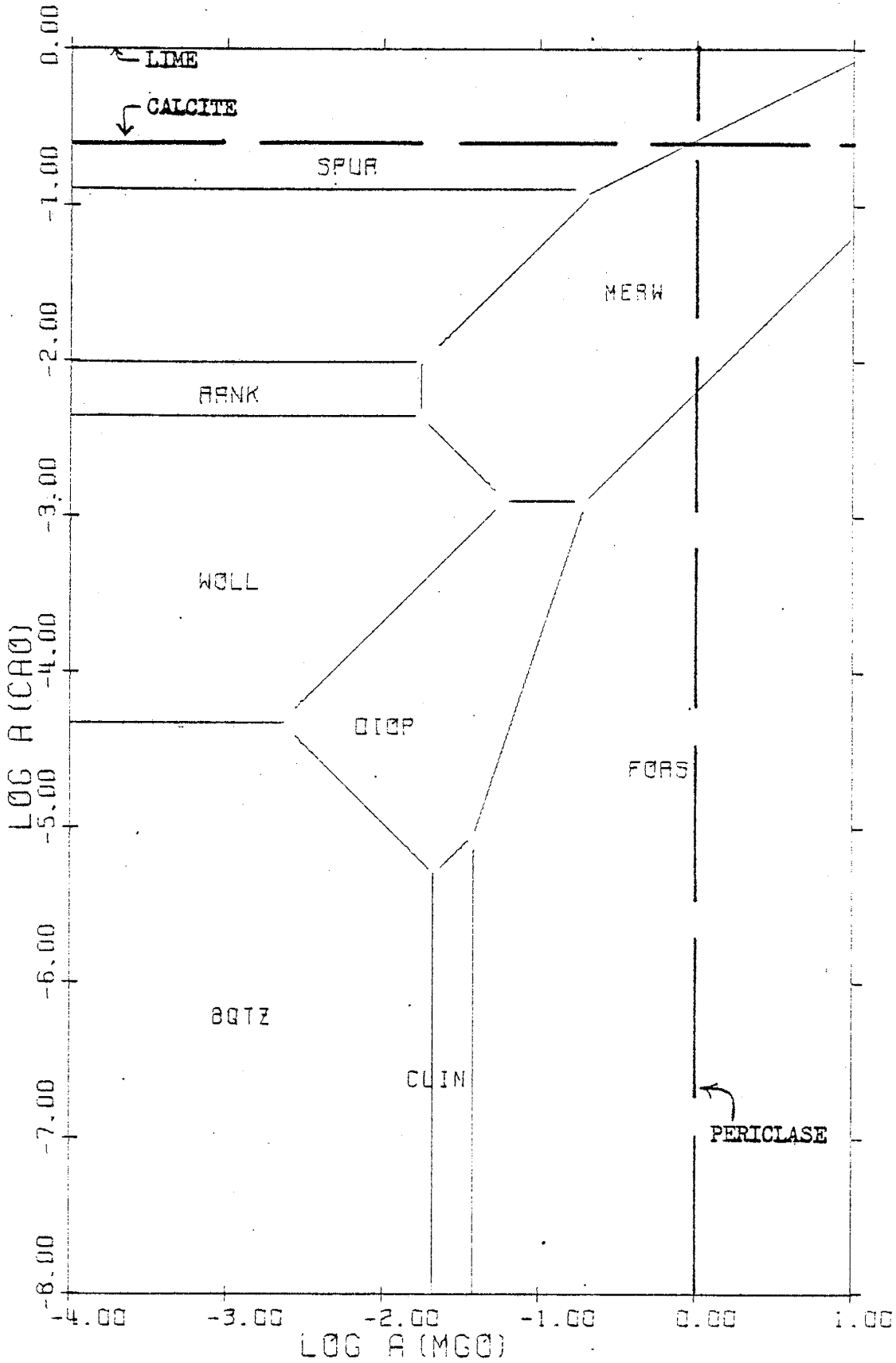
LIME
CALCITE
SPUR
MERW
RANK
WOLL
DIOP
FORS
QTZ
CLIN
PERICLASE
0.00
-1.00
-2.00
-3.00
-4.00
-5.00
-6.00
-7.00
-8.00
-4.00
-3.00
-2.00
-1.00
0.00
1.00
LOG A(CAO)
LOG A(MGO)

of temperature and pressure, although high pressures (∿1000 bars) may favor saturation with respect to calcite rather than wollastonite.

Figures 64 and 65 illustrate the tilleyite-spurrite transition between 400° and 600°C at 1 bar pressure. This transition is a function of the fugacity of CO_2 because

$$Ca_5Si_2O_7(CO_3)_2 \rightleftharpoons 2Ca_2SiO_4 \cdot CaCO_3 + CO_2 \qquad (8)$$

and

$$\log K_{r,T,P} = \log f_{CO_2} \quad . \qquad (69)$$

Log $K_{r,T,P}$ can be evaluated using equation (22), and the results at 1, 500 and 1000 bars pressure are plotted in Figure 67 as a function of temperature. Note that pressure has relatively little effect upon the stabilities of these minerals when compared to the great influence of temperature because it does not significantly alter log $K_{r,T,P}$ using the standard state employed here. The equilibrium curves in Figure 67 represent the log f_{CO_2} necessary to maintain equilibrium between spurrite and tilleyite at a specified temperature and pressure. For example, at 600°C and 1 bar, the equilibrium log fugacity of CO_2 is + 0.03 and thus when log f_{CO_2} = 0.0 at this temperature and pressure, spurrite should be stable, as is illustrated in Figure 65. At 400°C and 1 bar, the equilibrium log f_{CO_2} = -2.48 and therefore tilleyite is stable in Figure 64 at the same temperature and pressure when log f_{CO_2} = 0.0. Figures 64 and 65 are a good example of the manner in which activity diagrams constructed over a range of temperature and pressure demonstrate isochemical processes such as decarbonation. However, the tilleyite-spurrite transition is also illustrated in Figures 61 and 62 as a function of X_{CO_2} in an isothermal and isobaric system. These figures, drawn at 100 bars, 800°C and 0.4 and 0.2 X_{CO_2}, respectively, re-

Figure 67. Equilibrium curves for the reaction tilleyite ⇌ spurrite + CO_2 on a plot of log f_{CO_2} versus temperature at 1, 500 and 1000 bars pressure.

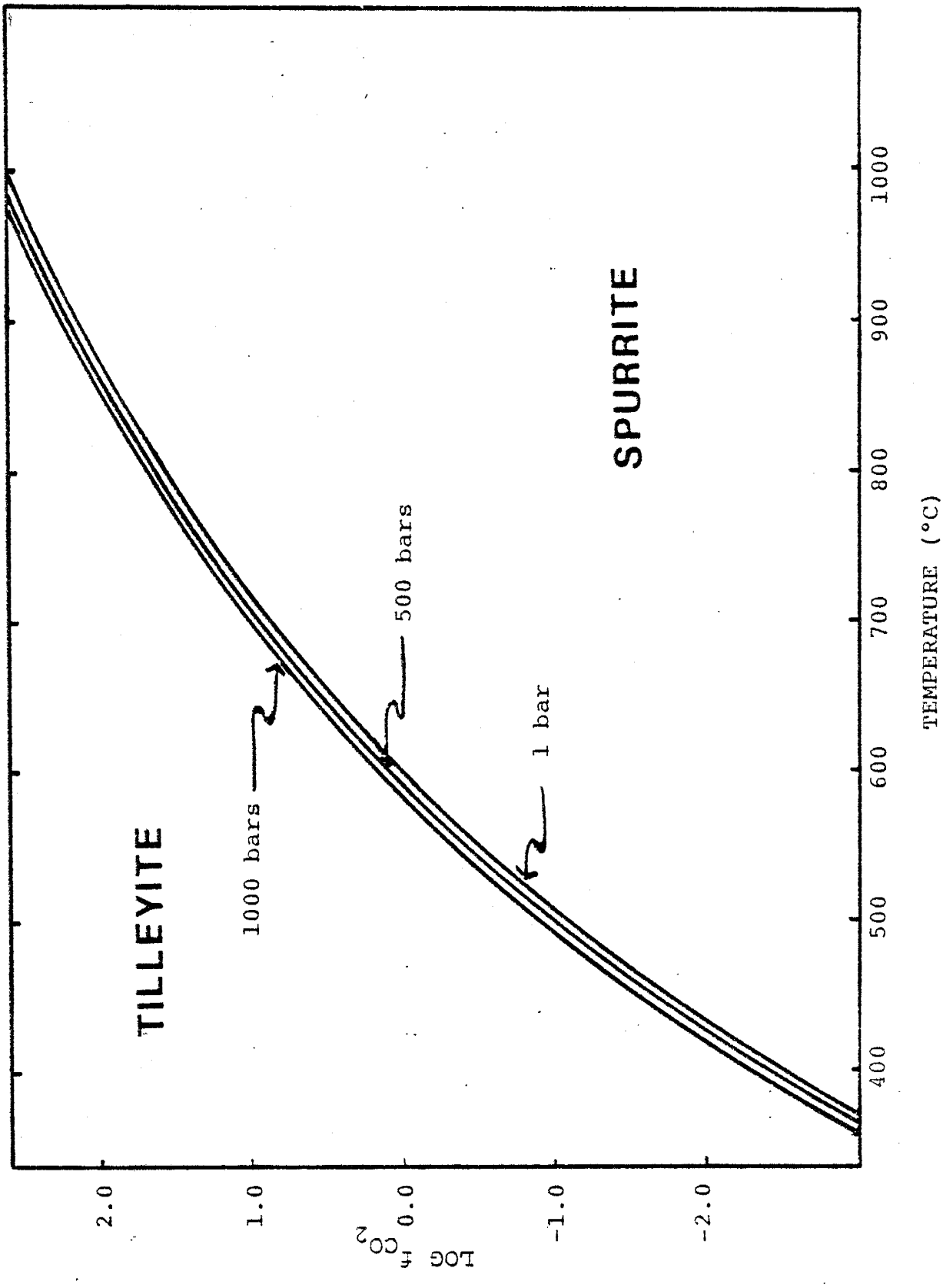
TILLEYITE
SPURRITE
1000 bars
500 bars
1 bar
2.0
1.0
0.0
-1.0
-2.0
LOG f_{CO_2}
400
500
600
700
800
900
1000
TEMPERATURE (°C)

flect the attainment of the equilibrium fugacity of CO_2 between these two mole fractions at the temperature and pressure of interest.

SUMMARY AND CONCLUSIONS

Calculation of equilibrium relations among minerals in the system $CaO-MgO-SiO_2-H_2O-CO_2$ may be carried out in terms of the thermodynamic variables of pressure, temperature and chemical composition provided the necessary thermodynamic data is available for the phases involved. Where such data is lacking, several of the fundamental thermodynamic parameters may be either estimated independently of or computed from experimentally determined phase equilibria. Determination of the thermodynamic data for spurrite and tilleyite requires the development of new estimation techniques and the modification of existing ones, as described in the literature and usually applied only to silicates, because of the need to account for the thermodynamic contributions of the CO_2 component in these minerals.

Evaluation of various methods of estimating the heat capacity of a phase indicates that the heat capacity power function of a mineral can be closely approximated by the stochiometric summation of the heat capacity power functions representing the contributions of the mineral's oxide components to the total heat capacity of the mineral. This method of estimation reproduces experimental values of heat capacity as accurately as the method suggested by Helgeson (1969) at all temperatures, and can be used with greater facility than Helgeson's method because the effects of phase changes upon heat capacity are automatically taken into account by the temperature-dependent contributions of the component oxides. Analogous treatments were used to calculate the standard third law entropy contributions of the oxide components CaO, MgO, SiO_2 and CO_2 as integral parts of a mineral to the entropies of carbonates and silicates. Entropies were also estimated with about the same degree of accuracy using a variation of an equation proposed

by Fyfe et al. (1958) describing the relation between the entropy and volume of a mineral and those of its component oxides. The methods of estimating entropies developed in this paper are equally, if not more, accurate as the estimates made using the methods of Latimer (1951), Kelley (1965), Fyfe et al. (1958) and Beane (1975) that were discussed earlier. Because of the clustering of the estimated entropies of spurrite and tilleyite about a central value, the estimations were averaged to obtain mean standard third law entropies. The values of $S^{\circ}_{298.15}$ for spurrite and tilleyite obtained in this manner are almost identical to those calculated using Kelley's method.

The estimated entropies of rankinite, spurrite and tilleyite were then used in conjunction with experimental data to calculate ΔH°_{f} for these minerals. It was found that the estimated entropies of spurrite and tilleyite together with calculated ΔH°_{f} values reproduce experimental equilibria quite well although the entropy of rankinite required adjustment from 52.23 to 48.3 cal/mole-deg to improve the fit of the curves.

Having determined the necessary thermodynamic data for the phases under consideration, pressure-temperature, temperature- X_{CO_2} and activity-activity diagrams were constructed using this data to define mineral equilibria in isochemical, isobaric and isothermal-isobaric systems, respectively. In general, the thermochemical calculations are in good agreement with experimental data as evidenced by the similarity in position and slope of the pressure-temperature and temperature- X_{CO_2} equilibrium curves, and by the illustration of the decarbonation, dehydration and solid-solid reactions commonly observed both in the laboratory and in natural systems. Activity diagrams constructed over a range of temperature and pressure show that mineral equilibria in the system $CaO-MgO-SiO_2-H_2O-CO_2$ are highly

dependent on the equilibration of carbonates. That is, high pressures and low temperatures tend to enhance the stability of the carbonates, whose stability, in turn, limits possible solution compositions and thus possible mineral associations. The stability of silicates such as clinoenstatite, forsterite, diopside and wollastonite which lie at low values of log $a_{CaO(c)}$ and log $a_{MgO(c)}$ are least affected by carbonate saturation and therefore can come to equilibrium with the aqueous phase over a wide range of temperature and pressure. However, spurrite and tilleyite can exist in equilibrium with the aqueous phase only at temperatures $\geq$600°C and pressures of approximately 100 bars or less. These same conditions are required for the equilibration of the minerals monticellite, merwinite, Ca-olivine and rankinite within the system. Reducing the mole fraction of CO_2 in the fluid phase at a specified temperature and pressure causes a decrease in carbonate stability and therefore a corresponding increase in the stability of silicates.

It therefore appears that thermochemical calculations can be employed profitably in the study of mineral equilibria as long as the thermodynamic data utilized in the calculations is believed to be of reasonable accuracy. It is emphasized that because metamorphism is not restricted to closed systems, the study of the causes of metamorphism should not only include consideration of changes in temperature, pressure and the mole fraction of CO_2 in the fluid phase, but the changing chemical potential of the components in the system as well.

APPENDIX A

Table A-1. Thermodynamic data for phases in the system $CaO-MgO-SiO_2-H_2O-CO_2$.

Name	Formula	ΔH_f° [a] cal/mole	$S^{\circ}_{298.15}$ [a] cal/mole-deg	V° [a] cm^3/mole	$Cp = a + bT + c/T^2$ a	bx10^{-3}	cx10^{5}	Source
Quartz - α	SiO_2	-217650.	9.88	22.688	11.22	8.20	-2.70	b
Quartz - β	SiO_2	-217730.	9.00	23.72	14.41	1.94	---	b
Lime	CaO	-151790.	9.5	16.764	11.67	1.08	-1.56	b
Periclase	MgO	-143800.	6.44	11.248	10.18	1.74	-1.48	b
H_2O (gas)	H_2O (gas)	-57796.	45.104	24465.	7.30	2.46	---	b
H_2O (liq)	H_2O (liq)	-68315.	16.71	18.069	18.04	--	---	b
CO_2 (gas)	CO_2 (gas)	-94051.	51.06	24465.	10.57	2.10	-2.06	b
Portlandite	$Ca(OH)_2$	-235610.	19.93	33.056	19.07	10.80	---	b
Brucite	$Mg(OH)_2$	-221200.	15.09	24.63	13.04	15.80	---	b
Calcite	$CaCO_3$	-288592.	22.15	36.934	24.98	5.24	-6.20	b
Aragonite	$CaCO_3$	-288651.	21.18	34.15	20.13	10.24	-3.34	b
Magnesite	$MgCO_3$	-266081.	15.7	28.018	18.62	13.80	-4.16	b
Dolomite	$CaMg(CO_3)_2$	-557613.	37.09	64.34	42.76	20.85	-11.53	c
Huntite	$Mg_3Ca(CO_3)_4$	-1086960.	67.0	122.58	---	--	---	-
Wollastonite	$CaSiO_3$	-390640.	19.60	39.93	26.64	3.60	-6.52	b

Table A-1, cont.

Name	Formula	ΔH_f° [a] cal/mole	$S^\circ_{298.15}$ [a] cal/mole-deg	V° [a] cm^3/mole	$Cp = a + bT + c/T^2$ a	b$\times10^{-3}$	c$\times10^{5}$	Source
Clinoenstatite	$MgSiO_3$	-370140.	16.22	31.47	24.55	4.74	-6.28	b
β - larnite	β - Ca_2SiO_4	-551420.	30.50	51.60	34.87	9.74	-6.26	b
Ca-olivine	γ - Ca_2SiO_4	-553973.	28.80	59.11	31.86	12.32	-4.64	b
Forsterite	Mg_2SiO_4	-520370.	22.75	43.79	35.81	6.54	-8.52	b
Rankinite	$Ca_3Si_2O_7$	-945435.[f]	48.3[d]	97.43	64.84	8.69	-15.93	d
Monticellite	$CaMgSiO_4$	-540800.	24.5	51.36	34.65	6.08	-8.12	d
Diopside	$CaMgSi_2O_6$	-767390.	34.20	66.09	52.87	7.84	-15.74	b
Akermanite	$Ca_2MgSi_2O_7$	-926510.	50.03	92.81	64.68	8.47	-17.36	d
Merwinite	$Ca_3MgSi_2O_8$	-1091490.	60.5	104.4	73.06	12.38	-14.81	d
Talc	$Mg_3Si_4O_{10}(OH)_2$	-1415700.[d]	62.34	136.25	84.60	41.66	-17.99	c
Serpentine (Chrysotile)	$Mg_3Si_2O_5(OH)_4$	-1043050.	53.2	108.5	75.82	31.60	-17.58	e
Tremolite	$Ca_2Mg_5Si_8O_{22}(OH)_2$	-2952935.	131.19	272.92	188.07	59.36	-45.90	c
Spurrite	$2Ca_2SiO_4 \cdot CaCO_3$	-1395200.[d]	81.63[d]	147.66	96.28	20.91	-19.06	d
Tilleyite	$Ca_5Si_2O_7(CO_3)_2$	-1524260.[d]	91.81[d]	170.42	100.96	25.31	-27.29	d

Table A-1, cont.

Sources of Thermodynamic Data

[a] Robie and Waldbaum (1968)

[b] Kelley (1960)

[c] Least squares fit of $H_T - H_{298}$ data given in Robie and Waldbaum (1968)

[d] Estimated as described in paper

[e] King et al. (1967)

[f] Weeks (1956)

REFERENCES

Beane, R. E., 1975, personal communication.

Bricker, O. P., Nesbitt, H. W., and Gunter, W. D., 1973, The stability of talc: Am. Min., v. 58, p. 64-72.

Brown, T. H., 1970, Theoretical predictions of equilibrium and mass transfer in the system CaO-MgO-SiO_2-H_2O-CO_2-NaCl-HCl: Ph.D. thesis, Northwestern University, Evanston, Illinois.

Fyfe, W. S., Turner, F. J. and Verhoogen, J., 1958, Metamorphic reactions and metamorphic facies: Geol. Soc. Am. Mem. 73, 259 p.

Greenwood, H. J., 1962, Metamorphic reactions involving two volatile components: Carn. Inst. Wash. Yrbk. 61, p. 82-85.

Greenwood, H. J., 1967, Wollastonite: Stability in H_2O-CO_2 mixtures and occurrence in a contact-metamorphic aureole near Salmo, British Columbia, Canada: Am. Min., v. 52, p. 1669-1680.

Greenwood, H. J., 1973, Thermodynamic properties of gaseous mixtures of H_2O and CO_2 between 450° and 800°C and 0 to 500 bars: Am. Jour. Sci., v. 273, p. 561-571.

Harker, R. I., 1959, The synthesis and stability of tilleyite, $Ca_5Si_2O_7(CO_3)_2$: Am. Jour. Sci., v. 257, p. 656-667.

Harker, R. I. and Tuttle, O. F., 1955, Studies in the system CaO-MgO-CO_2, Part I: The thermal dissociation of calcite, dolomite and magnesite: Am. Jour. Sci., v. 253, p. 209-224.

Harker, R. I. and Tuttle, O. F., 1956, Experimental data on the P_{CO_2}-T curve for the reaction: Calcite + quartz = wollastonite + CO_2: Am. Jour. Sci., v. 254, p. 239-256.

Helgeson, H. C., 1968, Evaluation of irreversible reactions in geochemical processes involving minerals and aqueous solutions: I. Thermodynamic relations: Geochim. et Cosmochim. Acta, v. 32, p. 853-877.

Helgeson, H. C., 1969, Thermodynamics of hydrothermal systems at elevated temperatures and pressures: Am. Jour. Sci., v. 267, p. 729-804.

Helgeson, H. C. and Kirkham, D. H., 1974, Theoretical prediction of the thermodynamic behavior of aqueous electrolytes at high pressures and temperatures: I. Summary of the thermodynamic/electrostatic properties of the solvent: Am. Jour. Sci., v. 274, p. 1089-1198.

Hemley, J. J., Shapiro, L., Shaw, D. R. and Luce, R. L., 1975, Stability relations of anthophyllite: Geol. Soc. Am. 1975 Annual Meeting, Salt Lake City, Utah, September, 1975, Abs. with programs, p. 1109.

Kelley, K. K., 1960, Contributions to the data on theoretical metallurgy. XIII. High-temperature heat content, heat capacity, and entropy data for the elements and inorganic compounds: U. S. Bur. Mines Bull. 584, 232 p.

Kelley, K. K., 1965, in Stull, D. R., Prophet, H. et al., JANAF Thermochemical Tables: Natl. Bur. Standards, Natl. Standards Reference Data Ser., Natl. Bur. Standards 37, 1141 p.

Kennedy, G. C., 1954, Pressure-volume-temperature relations in CO_2 at elevated temperatures and pressures: Am. Jour. Sci., v. 252, p. 225-241.

King, E. G., Barany, R., Weller, W. W. and Pankratz, L. B., 1967, Thermodynamic properties of forsterite and serpentine: U. S. Bur. Mines Rept. Div. 6962, 19 p.

Latimer, W. M., 1951, Methods of estimating the entropy of solid compounds: Am. Chem. Soc. Jour., v. 73, p. 1480-1482.

Metz, P. and Trommsdorf, V., 1968, On phase equilibria in metamorphosed siliceous dolomites: Contr. Mineral. and Petrol., v. 18, p. 305-309.

Robie, R. A. and Waldbaum, D. R., 1968, Thermodynamic properties of minerals and related substances at 298.15°K (25°C) and one atmosphere (1.013 bars) pressure and at higher temperatures: U. S. Geol. Survey Bull. 1259, 256 p.

Ryzhenko, B. N. and Malinin, S. D., 1971, The fugacity rule for the systems CO_2-H_2O, CO_2-CH_4, CO_2-N_2 and CO_2-H_2: Geochem. Intl., v. 1971, p. 562-574.

Ryzhenko, B. N. and Volkov, V. P., 1971, Fugacity coefficients of some gases in a broad range of temperatures and pressures: Geochem. Intl., v. 1971, p. 468-481.

Skippen, G. B., 1971, Experimental data for reactions in siliceous marbles: Jour. Geol., v. 79, p. 457-481.

Skippen, G. B., 1974, An experimental model for low pressure metamorphism of siliceous dolomitic marble: Am. Jour. Sci., v. 274, p. 487-509.

Slaughter, J. D., Kerrick, D. M. and Wall, V. J., 1975, Experimental and thermodynamic study of equilibria in the system CaO-MgO-SiO_2-H_2O-CO_2: Am. Jour. Sci., v. 275, p. 143-162.

Tuttle, O. F. and Harker, R. I.,1957, Synthesis of spurrite and the reaction wollastonite + calcite $\rightleftharpoons$ spurrite + carbon dioxide: Am. Jour. Sci., v. 255, p. 226-234.

Walter, L. S., 1963a, Experimental studies on Bowen's decarbonation series: I: P-T univariant equilibria of the "monticellite" and "akermanite" reactions: Am. Jour. Sci., v. 261, p. 488-500.

Walter, L. S., 1963b, Experimental studies on Bowen's decarbonation series: II: P-T univariant equilibria of the reaction: forsterite + calcite = monticellite + periclase + CO_2: Am. Jour. Sci., v. 261, p. 773-779.

Weeks, W. F., 1956, A thermochemical study of equilibrium relations during metamorphism of siliceous carbonate rocks: Jour. Geol., v. 64, p. 245-270.

Winkler, H. G. F., 1967, Petrogenesis of Metamorphic Rocks, rev. 2nd ed.: New York, Springer-Verlag, 237 p.

Winkler, H. G. F., 1974, Petrogenesis of Metamorphic Rocks, 3rd ed.: New York, Springer-Verlag, 320 p.

Zharikov, V. A. and Shmulovich, K. I., 1970, High temperature mineral equilibria in the system $CaO-SiO_2-CO_2$: Geochem. Intl., v. 1969, p. 849-869.

This thesis is accepted on behalf of the faculty of the Institute by the following committee:

Richard E. Beane

W. J. Budding

Merrill W. Bordner

Date 8/10/76